Performance Evaluation of Different SWGO Configurations

Master's Thesis in Physics

Presented by

Matei Ruta

October 21st 2022

Erlangen Centre for Astroparticle Physics
Friedrich-Alexander-Universität Erlangen-Nürnberg

Supervisor: Prof. Dr. Christopher van Eldik

Abstract

The Southern Wide-field Southern Wide-field Gamma-ray Observatory (SWGO) is a future water Cherenkov detection array that will investigate cosmic γ-rays between hundreds of GeV and hundreds of TeV. Numerous objectives of the detection site are set to include the identification of sources that emit Galactic cosmic rays in the PeV range, as well as dark matter investigations. At the current moment, possible tank designs and array layouts for SWGO are being assessed, in order to find the most suitable configuration. In this master's thesis, extensive air shower reconstructions have been conducted for 12 possible SWGO configurations, by assessing simulated Monte Carlo shower data. Consequently, the core, energy and angular performance of each setup could be investigated and the different configurations have been compared between each other. At this stage, the evaluation suggests that increased inner array sizes with lower fill factors could perform best at energies below 1 TeV, while full array diameters of 600 m seem to outperform both smaller (300 m) and significantly larger (1200 m) setups at energies above 10 TeV, assuming lower outer array fill factors in the latter case. Also, configurations with smaller PMT sizes but a larger number of tank units seem to perform better than setups with larger PMTs and a decreased tank numbers above 10 TeV. These preliminary findings would however need to be investigated with optimised data cuts in the future. Throughout the entire reconstruction process, it was possible to only use reconstructed shower properties instead of relying on true seed values throughout the procedure. Thus, γ-ray induced air showers could be reconstructed in a more realistic way. This master's thesis can be seen as a first performance evaluation of the presented 12 M5 configurations that could indicate which setups and features might perform best, thus suggesting which aspects could be investigated further, in order to later determine the best configuration for γ-ray searches in the TeV energy range.

Contents

1 Introduction

The vastness and unconfined mystery of the universe has always been of great interest to mankind. Be it the Neolithic and Bronze Age Europeans who first documented their observations of astronomical phenomena by means of the construction of the Goseck circle or the creation of the Nebra sky disc [Per+20]. Be it Nicolaus Copernicus who as one of the first proclaimed the existence of a heliocentric worldview instead of the previously accepted and socially imposed geocentric worldview through planetary examination [Cop+78]. Or be it astronomers and astrophysicists today who, assisted by modern-day interferometry, radio telescopy and further technology-assisted measurement techniques, are able to explain the content and functioning of our universe in more and more detail. They all continuously strive for improved understanding of the seemingly incomprehensible nature of the universe. The reason for this ambitous endeavour does not only lie in an insatiable curiosity towards the distantly placed unknown, though. It is the unknown nature of what is right in front of us which furthers our interest in the exploration of the cosmos.

The field of particle physics, inspecting the fundamental nature of radiation and matter by investigation of elementary particles and forces, is strongly intertwined with astrophysics, forming the combined branch of astroparticle physics. A good example of the intersection between the two disciplines can be found in the exploration of dark matter in the universe, which might possibly lead to the discovery of a new fundamental particle. Astrophysical examinations of the universe indicate the existence of a form of matter which does not absorb, emit or reflect electromagnetic radiation, thus being invisible. This dark matter is hypothesized to be composed of so-called Weakly Interacting Massive Particles (WIMPs) which, when entirely proven, would be classified as a new fundamental particle [RST18]. Our understanding of the fundamental nature of matter would thereby be improved and expanded by astrophysical explorations.

One way to further explorations in the realm of γ-ray astronomy is the examination of the previously less investigated high energy γ-rays. The Large High Altitude Air Shower Observatory (LHAASO) was recently able to detect ultrahigh-energy photons up to 1.4 PeV, thus confirming that the cosmic ray spectrum extends well beyond 1 PeV. It thereby substantiates the existence of so-called PeVatrons, cosmic ray factories which accelerate photons up to PeV energies. The location and identification of such and other accelerators would be necessary in order to find the origin of Galactic cosmic rays. This can be achieved by examining ultrahigh-energy γ-rays above 100 TeV which happen to be the principal signature of both proton and electron PeVatrons [Cao+21].

A future γ-ray detection array, the so-called Southern Wide-field Gamma-ray Observatory (SWGO), will operate up to γ-ray energies of several 100s of TeV and will thus be able to assist in the detection and analysis of high-energy γ-rays. At this stage in time, however, the SWGO is not yet operational and currently being developed. It is set to utilize the Water Cherenkov Detection Technique in order to detect and investigate cosmic γ-ray showers. In this setup, the electromagnetic components of the Extensive Air Shower (EAS) pass through water tanks, resulting in the emission of Cherenkov radiation which in turn can be measured by one or more PMTs within the water tanks. The exact design and distribution of the water tanks on the ground can thereby vary and impact the accuracy with which the detection site is able to reconstruct γ-ray air showers. Within this work, the accuracy with which the M5 array layouts, a set of configurations which the SWGO collaboration is currently considering as viable options for the future design of the detection site, are able to recontruct the air shower's core position, energy and direction in different energy ranges shall be investigated.

In this thesis, some of the fundamental concepts of astroparticle physics and high altitude γ-ray astronomy, which are necessary for the understanding of the remaining portion of the work, are explained first. Afterwards, an introduction to the water Cherenkov detection technique and detection sites which feature this mode of observing γ-ray induced air showers is given. Then, the template-based reconstruction method is elaborated which is used for the reconstruction of Extensive γ-ray Air Showers in each of the possible M5 configurations. In the next part of this thesis, the similarities and differences between the tank designs and array layouts of M5 are showcasted which put the later findings into perspective before then assessing the reconstructive capabilities of the mentioned configurations. The accuracy of the reconstruction of the air shower's core position is analysed by examining its respective core resolution, while the energy reconstruction is assessed by means of the energy resolution and the energy bias. Furthermore, the direction reconstruction can be investigated by means of the angular resolution and bias. As it is now possible to properly reconstruct the shower's direction in SWGO, only reconstructed values could be used throughout the entire reconstruction procedure, as outlined in chapter 4, instead of the previously taken true seed values for the zenith and azimuth angles. This is an important further step towards the real life reconstruction process in which none of the shower properties is previously known and all properties need to be reconstructed.

2 Cosmic Rays and Extensive Air Showers

In this chapter, an introduction to cosmic rays and Extensive Air Showers is given, the understanding of which is vital for the comprehension of the remaining portions of this thesis.

2.1 Cosmic Rays

Cosmic rays can be defined as high-energy particles which originate from outer space and the resulting secondary particles that are generated if and when the incoming particle, also being referred to as primary particle, passes through the earth's atmosphere. First, cosmic radiation has been discovered by Victor Hess in 1912 and the investigation and analysis of this subset of particles has been vital in the examination of elementary particles and particle interactions ever since. One example of such investigations and findings in the sphere of particle physics that can be associated with the study of cosmic rays is the discovery of the positron and thus of antimatter, in 1932 [Chi09]. In this instance, the investigation of cosmic ray particles with the help of a cloud chamber made it possible to spot the track of a positively charged particle with a mass smaller than the proton mass, which was subsequently called positron [And33]. The detection and analysis of cosmic rays can thus lead to an improved understanding of particle physics, which is one of the main reasons for its furthering.

In this work, the focus lies on cosmic γ-rays, but it is important to mention that this is not the only form of cosmic radiation. Examples of cosmic ray particles include charged particles like protons, muons or tauons and non-charged particles like neutrinos. As mentioned beforehand, cosmic rays can be divided into primary cosmic rays that originate in outer space and secondary radiation that emerges as a consequence of the interaction of the primary cosmic ray particles with the atmosphere.

The energy spectrum of primary cosmic rays behaves almost like a steeply decaying power law, as can be seen in Figure 2.1. The slope of the spectrum changes at approximately $10^{15.5}$ eV (at the so-called "knee"), at $10^{17.8}$ eV ("2nd knee") and at 10^{19} eV ("ankle") [NW00].

Depending upon the energy of the primary particle, its origin can vary and is discussed in the following. Cosmic ray particles that are found on the lower end of the energy

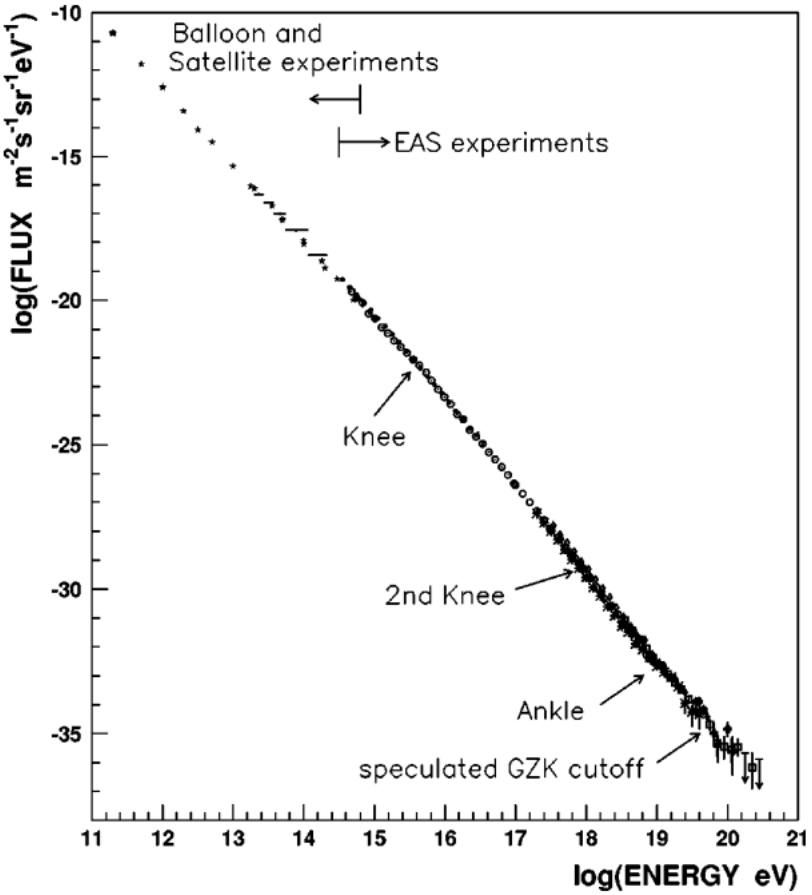

Figure 2.1: Measured energy spectrum of primary high-energy cosmic rays in an energy range of 10^{10} eV to 10^{21} eV. The flux is plotted logarithmically over $\log(E)$ and the characteristic changes in the power law-like slope are labelled according to their respective colloquially designated terms of the "knee" (at $10^{15.5}$ eV), the "2nd knee" (at $10^{17.8}$ eV) and the "ankle" (at 10^{19} eV) (figure taken from [NW00]).

spectrum (E < 1 GeV) are expected to be produced by solar flares, as the magnetic field of the sun is thought to block out most particles outside the solar system in that energy range. For higher energies up until 5 PeV ($= 5 \cdot 10^{15}$ eV), primary particles predominately originate outside our solar system, but still within the confinements of our galaxy, while between 5 PeV and 0.1 EeV ($= 0.1 \cdot 10^{18}$ eV) a transition from galactic to extragalactic particle origins takes place. At and above approximately 5 EeV, the particles on the high end of the energy spectrum are predominantly produced outside our galaxy. The previously mentioned "knee", "2nd knee" and "ankle" are important transition points within the energy spectrum. The "knee" signifies the energy at which cosmic ray particles are no longer bound to their respective galactic objects and have enough energy to overcome the strength of the object's magnetic field and exude. The "2nd knee" marks the transition to heavier primary cosmic ray particles, as outlined in [Tan+18], while the ankle can be seen as the transition point to principally extragalactic cosmic rays [Jos19].

2.2 Extensive Air Showers

An Extensive Air Shower (EAS) can be described as a cascade of secondary particles that emerges in response to the interaction between primary particles and the atmosphere. These EAS can be divided into electromagnetic and hadronic showers, depending upon the particle interactions that contribute to the emergence of such cascades. In the following, the workings of electromagnetic showers will be outlined, as γ-ray induced particle cascades fall into this category of EAS, which will be investigated throughout this thesis.

The main processes by which electromagnetic EAS result are bremsstrahlung and pair production. Both of them are explained in the following, before elaborating on the interplay between those two processes throughout the generation of an electromagnetic particle shower.

2.2.1 Bremsstrahlung

When an electron or positron passes through an electric field, it is deflected in the Coulomb field under loss of kinetic energy. Consequently, this energy is emitted in form of electromagnetic radiation, in this instance also referred to as bremsstrahlung. The energy loss of the electron can thereby be quantified in the following way:

$$-\frac{\partial E}{\partial X} = \frac{E_0}{X_0} \tag{2.1}$$

Here, E_0 describes the initial electron energy, while X_0 indicates the radiation length, which is defined as the average distance that the particle has to pass until losing a fraction

of $1/e$ of its initial energy. One can write

$$E(x) = E_0 \cdot \exp\left(-\frac{x}{X_0}\right) \tag{2.2}$$

in order to describe the energy E of the electron after a distance x. Oftentimes, the development of different EAS can be compared to one another in relation to their respective radiation lengths, instead of the overall proceeded distance, as the amount of matter that the particle shower passes is then also taken into consideration. One can characterise the radiation length as

$$X_0 = [4\alpha r_e^2 \frac{N_A}{A} \cdot (Z \cdot (Z+1) \ln(\frac{183}{Z^{1/3}})]^{-1} \tag{2.3}$$

with $\alpha = 1/137$ being the fine structure constant, r_e the classical electron radius, Z the proton number of the proceeded medium, A its molar mass and N_A Avogadro's constant [Edw17].

2.2.2 Pair Production

Pair production is defined as the process in which a highly energetic photon is converted into an electron-positron pair. Thereby, on average half of the energy of the photon is being transferred onto the electron, while the other half passed on to the positron. Consequently, the energy of the incoming photon needs to exceed the rest energy of both the electron and positron, in order for this process to be possible. The radiation length of a photon that interacts through pair production can be described as

$$X_0 = \frac{7}{9} \cdot \lambda \tag{2.4}$$

in relation to its mean free path $\lambda = 47.8$ g cm^{-2} [Edw17].

2.2.3 Shower Emergence

Simplistically, the emergence of an electromagnetic shower can be seen as the alternation of electron-positron pair production and the generation of bremsstrahlung. A sketch of both the generation of an electromagnetic and hadronic shower is shown in Figure 2.2, while the emergence of electromagnetic showers is explained in the following.

First, the incoming γ-ray undergoes pair production and a highly energetic electron and positron are generated. These charged particles can in turn produce bremsstrahlung when passing through the internal electric fields of the nuclei in the atmosphere. As a result, photons emerge that again can go through the process of pair production with

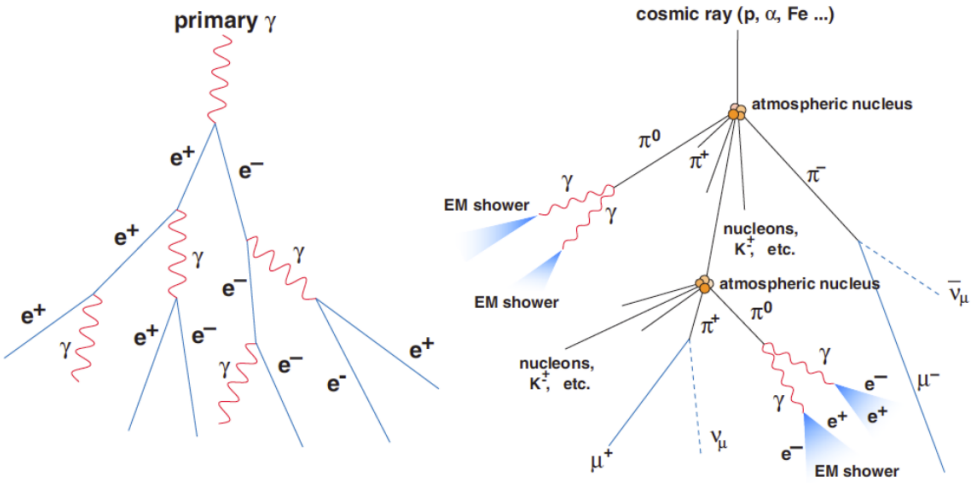

Figure 2.2: Sketch showcasting the emergence of an electromagnetic (left) and hadronic (right) EAS (figure taken from [Jos19]).

subsequent bremsstrahlung being generated by the resulting electrons and positrons. Consequently, a cascade of photons and charged electrons and positrons develops in which the number of particles N doubles at each of those interaction steps n. The number of shower particles at a certain distance x can then be calculated as

$$N = 2^n = \exp(\frac{x}{X_0}) \tag{2.5}$$

This shower expansion continues until the average energy of the particles falls below the critical energy E_c. At this point, energy losses through ionisation exceed those that happen due to bremsstrahlung and pair production and the number of shower particles decreases until the EAS eventually dies off. The maximum number of particles that is reached throughout the emergence of the shower can be quantified by

$$N_{\text{max}} = \frac{E_0}{E_c} = 2^{n_c} \tag{2.6}$$

with n_c being the number of interaction lengths after which the energy of shower particles reaches E_c. Using Equation 2.5 and Equation 2.6, one can also define the maximum radiation length as

$$X_{\text{max}} = X_0 \cdot \ln(\frac{E_0}{E_c}) \tag{2.7}$$

The property of X_{max} can be interpreted as the radiation length after which the shower reaches its maximum and varies, depending on the primary shower particle. It is important to point out that this is an idealistic description of EAS development and properties

such as $X_{\max}$ and N are bound to fluctuate. Also, a few simplifying assumptions have been made. For instance, the interaction lengths of electrons and photons were assumed to be identical and it was presupposed that bremsstrahlung and pair production were the only interactions contributing to the emergence of the EAS [Edw17].

Apart from the energy and $X_{\max}$, the incoming γ-ray particle can further be characterised by its zenith and azimuth angle of origin. In contrast to charged cosmic rays, γ radiation is not deflected by magnetic field along its way, as it carries no charge. Thus, one is able to reconstruct its location of origin and study high energy accelerators directly through the examination of γ-ray particles [Jos19].

3 Water Cherenkov Detection Sites

The Southern Wide-field Gamma Ray Observatory (SWGO) is a future high altitude γ-ray detection site, which operates as a water Cherenkov detection array. Thus, an introduction into the workings of such detection sites will be given. Furthermore, the High-Altitude Water Cherenkov Observatory (HAWC) is prefaced for purposes of reference, before presenting SWGO itself.

3.1 Cherenkov Radiation

In order to understand how water Cherenkov detection sites operate, it is important to introduce the concept of Cherenkov radiation first.

Cherenkov radiation is defined as a form of electromagnetic radiation which emerges when a charged particle passes through a medium of refractive index n with a velocity $v = \beta \cdot c$ that surpasses the phase velocity of light c/n in the given medium. For velocities below c/n, the polarisations that are generated by the charged particle near its pathway vanish straight away, as shown in Figure 3.1, and the dipol radiation from the polarised particles interferes destructively. For velocities above c/n, the radiation becomes coherent in accordance to Huygen's law and a wavefront is formed [Ish20].

The wavefront is of conical shape and the angle θ_c between the trajectory of the particle and the emerging wavefront, also referred to as Cherenkov angle, can be described in the following way:

$$\cos(\theta_c) = \frac{1}{\beta n} \tag{3.1}$$

Consequently, possible values of $\cos(\theta_c)$ range from a minimum of $1/n$ for the highest possible particle velocity of $v = c$ to 1. In the latter case, the Cherenkov condition

$$\beta = \frac{1}{n} \tag{3.2}$$

can be formulated, which marks the β value for the treshold velocity for which Cherenkov radiation is emitted [Ish20].

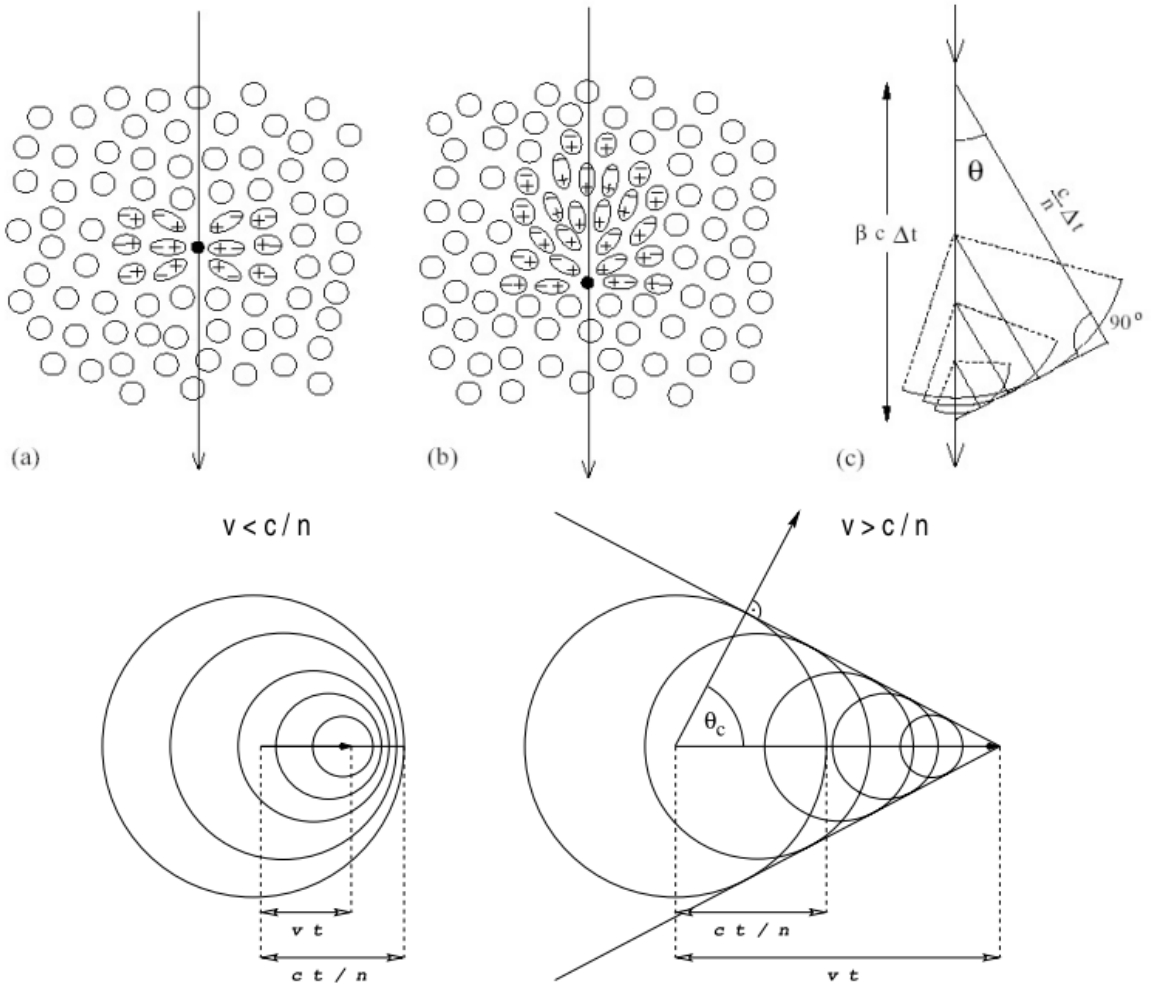

Figure 3.1: Upper row: Sketch of the appearing polarisation for a charged particle that passes the dielectric medium with a velocity below (a) and above (b) the phase velocity of light in the given medium. In the latter case, a wave front of Cherenkov light emerges (c); Lower row: According to the Huygen's law, a wavefront only develops for particle velocities above (right) and not below c/n (left) (figure taken from [Hen07]).

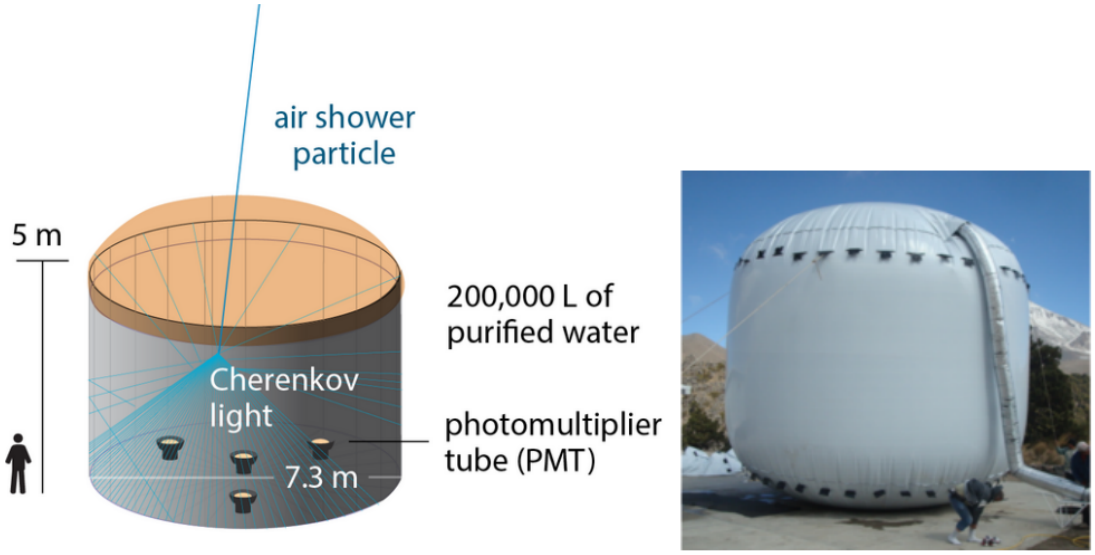

Figure 3.2: Sketch of the interaction between shower particles and the water inside of the detection tanks (left) and an outside image of a HAWC tank unit (figure taken from [Jos19]).

3.2 Detection Mechanism

When a primary γ-ray particle hits the earth's atmosphere and an EAS develops, its charged components can be detected at high altitudes via water Cherenkov detectors. It presupposes the use of water-filled tanks, the content of which can then interact with the incoming radiation and consequently produce a measurable signal. More precisely, the charged components of the EAS pass through the water within the tanks and thus generate Cherenkov radiation, in accordance with section 3.1. This Cherenkov radiation can then be detected by photomultiplier tubes (PMTs) and generate a measurable signal in form of photoelectrons.

The PMT consists of a photocathode (through which the Cherenkov photons enter the PMT), multiple dynodes and an anode. When the photons hit the photocathode, electrons are ejected due to the photoelectric effect. Through a focusing electrode those electrons then enter the electron multiplier, which consists of several electrodes, so called dynodes. At each dynode, the incoming electrons produce a set of secondary electrons which then in turn are accelerated towards the following dynode. Consequently, the number of electrons increases exponentially from dynode to dynode. The acceleration happens as a result of the differences in potential between the individual dynodes, because each dynode is kept at a higher potential than its predecessor [Pho].

An example of a water tank and its interaction with an incoming EAS can be seen in Figure 3.2, in the case of HAWC. Water Cherenkov detection sites are placed at high altitudes, in order for the shower components to carry more energy than at lower heights,

which in turn makes it possible for Cherenkov condition shown in Equation 3.2 to be fulfilled and consequently for Cherenkov radiation to be generated within the water tanks. For instance, the HAWC detection array has been constructed at an altitude of 4100 m above sea level. Usually, detection sites that investigate air showers via the water Cherenkov detection technique are furthermore composed of several tank units, instead of a single larger tank. One of the reasons for this can be found in the fact that it makes it possible to build and and maintain them separately, which implies that the site remains operational even if individual tank units are damaged. Furthermore, one can assess local variations of the EAS, which aids in γ-hadron separation and direction reconstructions. The information presented in this section has been drawn from [Jos19], where more details with regard to the detection mechanism are outlined.

3.3 High-Altitude Water Cherenkov Observatory (HAWC)

In the following, the already operational High-Altitude Water Cherenkov Observatory (HAWC), which investigates γ-ray data by means of water Cherenkov detection, shall be assessed in more detail with regards to its setup and applications. This makes it possible to compare the future SWGO observatory to a similar setup and showcast possible applications, once SWGO too becomes operational.

The HAWC observatory is a wide field-of-view water Cherenkov detection setup, located in the national park Pico de Orizaba in Mexico. As mentioned beforehand, the array is placed at 4100 m above sea level. The utilised water tanks measure 7.3 m in diameter and 5 m in height and the water level is kept at a value of 4.5 m, thus warranting that the incoming electrons and positrons are entirely absorbed until they reach the tank floor, while passing through the water tanks [RV21].

The layout of the detection site can be seen in Figure 3.3, consisting of 300 tank units which each contain 200,000 l of purified water that is filtered and softened and afterwards sterilized with UV light. As can be seen in Figure 3.2, each water-filled tank contains four PMTs that are mounted on the floor of the tank and are pointing upwards [Smi15].

As outlined in [Jos19], the HAWC observatory operates within an energy range of several 100s of GeV up to approximately 100 TeV, making it highly suited for high-energy γ-ray investigations. This, for instance, enabled the detection site to study the ultra-high energy spectrum of the source MGRO J1908+06, which is one of the highest-energy known γ-ray sources with energies exceeding 200 TeV [Alb+22]. Further applications of HAWC also include dark matter searches, as reported in [Abe+19], by the detection and analysis of γ-ray signal from low-luminosity regions with predicted dark matter content. In fact, HAWC observations set new limits in terms of dark matter decay and annihilation [Abr+19] and thus inspired the furthering of the similar Large High Altitude Air Shower Observatory (LHAASO) in China, which managed to investigate

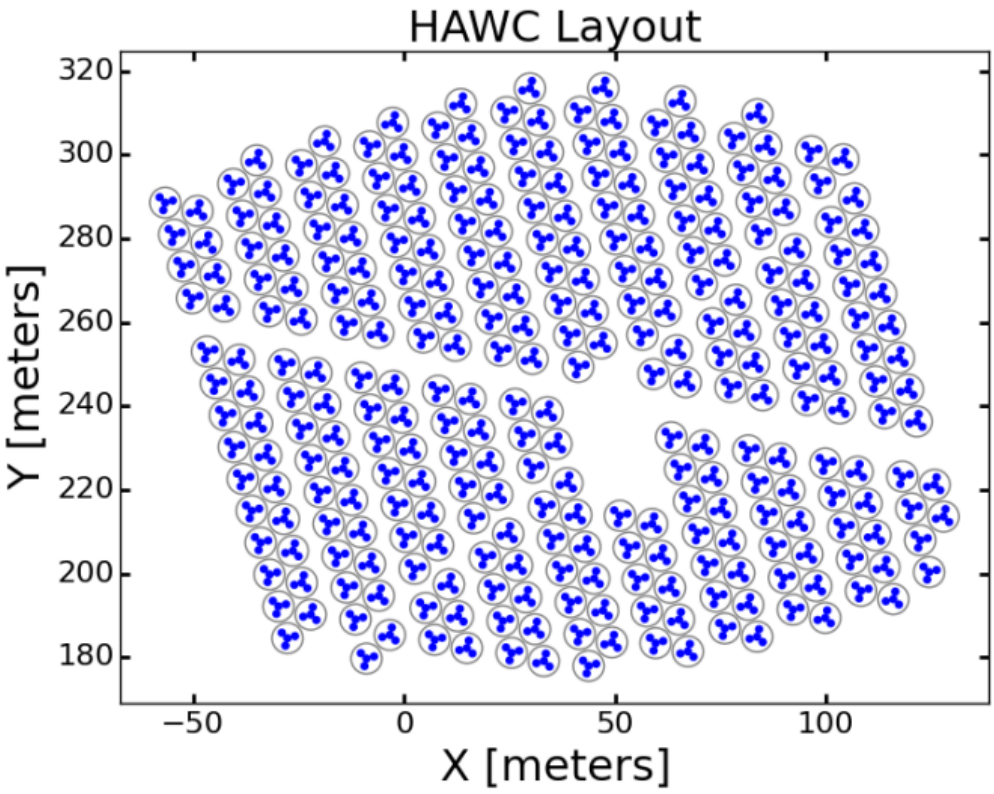

Figure 3.3: Array layout of the HAWC detection site. The circles represent the individual tank units, while the blue dots indicate the positions of the PMTs (figure taken from [Smi15]).

Objective	Major Requirements
Measure TeV halos around nearby PWNs	wide field of view
Identify sources of PeV Galactic cosmic rays	sensitivity to highest energies
Measure the Galactic Center morphology	wide field of view, sensitivity to highest energies
Study the nature of the Fermi bubbles	wide field of view
Measure the Galactic diffuse emission	wide field of view
Measure the local cosmic-ray anisotropy	wide field of view
Measure solar cosmic-ray interactions	large unbiased duty cycle
Search for new Galactic VHE emitters	wide field of view, large unbiased duty cycle
Detect AGN flares and issue alerts	large unbiased duty cycle, sensitivity $\lesssim$1 TeV
Search for periodicity in AGNs	large unbiased duty cycle
Measure long-term emission from AGNs	large unbiased duty cycle
Search for neutrino VHE counterparts	large unbiased duty cycle
Search for counterparts to GW events	wide field of view, large unbiased duty cycle
Measure nearby bright GRBs	wide field of view, sensitivity $\lesssim$1 TeV
Search for dark matter annihilation/decay	wide field of view, sensitivity to highest energies
Probe Lorentz invariance violation	sensitivity to highest energies
Search for PBHs and ALPs	wide field of view

Figure 3.4: Objectives and requirements for the future SWGO detection site (table taken from [Abr+19]).

ultrahigh-energy photons up to 1.4 PeV and thus substantiate the existence of PeVatrons [Cao+21], as mentioned in chapter 1. The successes of HAWC and LHAASO can be seen as one of the main driving forces behind the creation of the future the SWGO detection site, which plans to investigate similar phenomena at high energies, as will be elaborated on in the following.

3.4 Southern Wide-Field Gamma Ray Observatory (SWGO)

The Southern Wide-Field Gamma Ray Observatory (SWGO) is a future ground-based γ-ray observatory, which is set to operate within an energy range from 10s of GeV up to several PeV. It will deploy the water Cherenkov detectors and is planned to be build in South America, while the exact location is yet to be determined. Similarly to HAWC and LHAASO, scientific objectives of the SWGO detection site include the investigation of dark matter sources, the search for primordial black holes (PBHs) and axion-like particles (ALPs), as well as the exploration for new very high-energy (VHE) cosmic ray sources. As can ben seen in a more comprehensive list of objectives and requirements for SWGO in Figure 3.4, further objects of interest encompass active galactic nuclei (AGNs) and pulsar wind nebula (PWNs) [Abr+19].

Due to its geographical positioning on the Southern hemisphere, the SWGO sky coverage varies from HAWC, as illustrated in Figure 3.5. Thus, future observations from SWGO can be used as a complement to the data which is taken from HAWC, once the SWGO detection site starts operating. It is important to point out that some objects of interest, such as the Galactic centre and Fermi bubbles are only partially covered by HAWC. Consequently, the observations that can be done with SWGO will be vital for the further study of these sources at high energies and make it possible to investigate parts of the sky that are inaccessible to HAWC in more detail.

While the exact array layout of SWGO is still undetermined and a subset of such possible configurations will be discussed in chapter 5, the overall area of the setup is expected to be significantly larger than HAWC. In case of the latter, the surface of the array measures up to $20,000\ \mathrm{m}^2$, whereas the first, preliminary setup of SWGO, the reference configuration, covers an overall area of $221,000\ \mathrm{m}^2$. Also, the number of tank units is increased from 3,000 in HAWC up to 5,000 in the reference design of SWGO. As a consequence, given portions of the SWGO reference setup are higher in both total detection area and tank density than the entire HAWC observatory. Thus, sub-1TeV γ-ray events with consequently low particle densities can be studied more accurately, while the increased size of the SWGO detection site implies improved measurements of high-energy events with a larger shower spread [Abr+19]. Here, the reference setup of SWGO has been used for comparison purposes. While the performance related benefits of SWGO in comparison to HAWC should remain true for all possible SWGO configurations, it is important to point out that the exact number of tanks and overall covered area varies in between the individual configurations. A thourough analysis of these configurations and the benefits of various array layouts and sizes is outlined in chapter 5 and troughout of the performace analysis in chapter 6.

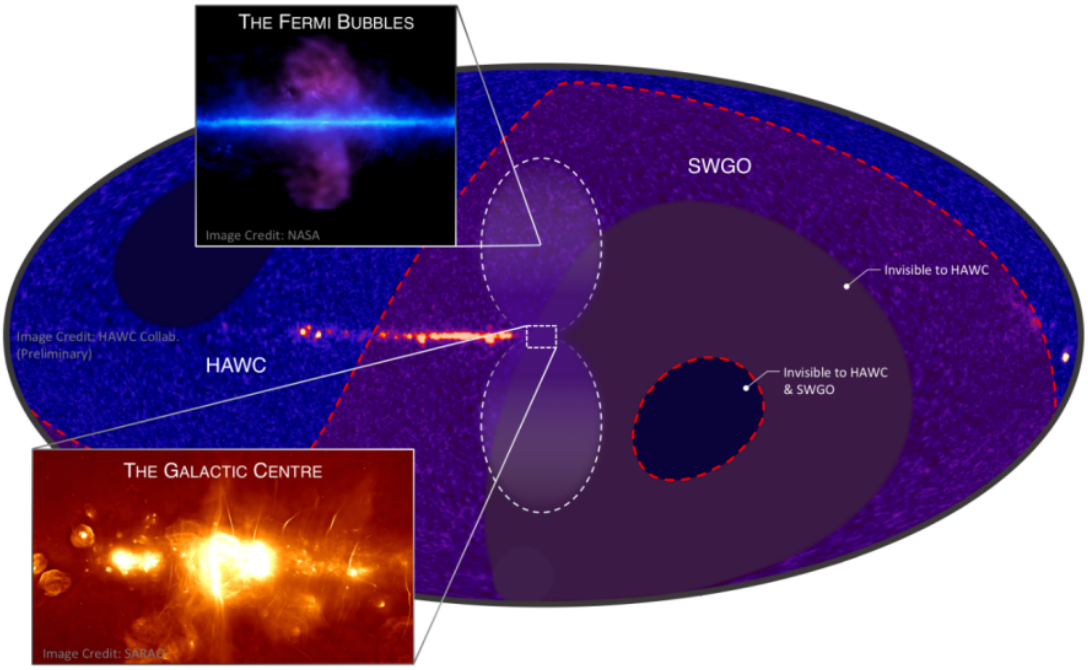

Figure 3.5: Sky coverage of SWGO in Galactic coordinates, projected on top of a significance map of the HAWC observatory (image taken from [Abr+19]).

4 Template-Based Reconstruction Method

The objective of this thesis is the analysis of the reconstruction performance of the M5 configurations. However, at this stage none of these configurations have been physically built and therefore none of the setups can be assessed in real life. Therefore, simulations of such γ-ray EAS have been used throughout this thesis which are elaborated on in section 4.1, before explaining the template-based reconstruction procedure itself.

4.1 Simulations

A total number of 250,000,000 γ-ray induced EAS have been simulated via the Monte Carlo-based program CORSIKA, which models the development of an EAS by simulating both primary particle properties and the particle interactions by which these air showers emerge [Hec01], at each stage of the shower development. Followingly, the number and distribution of secondary shower particles at given detector heights can be modelled [Jos19].

In a next step, the interaction between those CORSIKA showers and the tanks of the configuration is simulated via the *Geant*4 toolkit, which models the interaction of such EAS with matter [Ago+03], and saved in so-called HAWCSim files. These simulation files consequently do not only contain the information encoded into the CORSIKA files, but furthermore hold data that characterises the response in the tanks of the configuration to the respective EAS. For instance, each time that a given PMT converts the Cherenkov flashes into a photoelectron in response to the shower, the ID of that PMT is being saved within a variable and the reoccurance of the same PMTID in that variable signifies a further instance in which a photoelectron is generated within that PMT. As the location of each PMT is known, that makes it possible to assess which portion of tanks in the detection array respond to the incoming shower with which number of triggered photoelectrons.

These HAWCSim files are the starting point of the reconstruction chain, the workings of which are expanded upon in this chapter up to the point of the final reconstruction file. The goal of a given reconstruction is to predict primary particle properties, such as energy and direction, by the assessment of the array's response to the given shower, while the HAWCSim file serves as input. The predicted and known, simulated primary

Parameter	Bin size	Value range
E	$\Delta log(E) = 0.05$	31.6 GeV - 1 PeV
X_{max}	$\Delta X_{\mathrm{max}} = 50 \frac{\mathrm{g}}{\mathrm{cm}^2}$	$150 \frac{\mathrm{g}}{\mathrm{cm}^2}$ - $750 \frac{\mathrm{g}}{\mathrm{cm}^2}$
θ	$\Delta cos(\theta) = 0.06$	0° - 68.9°
r	$\Delta r = 2\mathrm{m}$	0 m - 2600 m

Table 4.1: Binning for the template creation of all of the investigated configurations

particle properties can then be saved together in the final reconstruction file, which is in turn used throughout the performance assessment of each configuration.

4.2 Templates

Before shower properties can be reconstructed, it is necessary to formulate an expectation with regard to the detector's response to said shower, which can be used for reference when assessing newly incoming, unknown events. Meaning: one needs to know how many photoelectrons are triggered at which distance from the core of a given shower for an EAS with certain energy, zenith angle and X_{max} values. When a shower with similar properties then falls onto the array, the interplay between the number of generated photoelectrons and the distance between triggered tanks and shower core can be recognised and similar energy, zenith angle and X_{max} values to the previously investigated shower can be predicted.

This expectation manifests itself as templates, which can be defined as three dimensional histograms, that visualise the probability $\log(P)$ (z-axis) that a certain number of photoelectrons $\log(n_{\mathrm{PE}})$ are triggered at distance r to the shower core in response to an EAS that falls within a set of a given energy, zenith angle and X_{max} binning. For each combination of bins, one template is generated and filled with Monte Carlo shower data. At $\log(n_{\mathrm{PE}}) = -3$, the probability that 0 photoelectrons are generated is being stored. One such template can be seen in Figure 4.1.

The binning that has been used throughout the template creation process of the M5 configurations can be seen in Table 4.1. Overall, the interplay between $\log(n_{\mathrm{PE}})$, r(m) and $\log(P)$, also referred to as the Lateral Distribution Function (LDF), can be fed into the templates for a total number of 250,000,000 EAS. Followingly, each template for each combination of bins is filled with data and subsequently functions as reference when assessing newly incoming γ-ray showers. The LDF of the unknown shower can then be fitted to the templates and predicitions with regard to the shower's energy, zenith angle and X_{max} can be made.

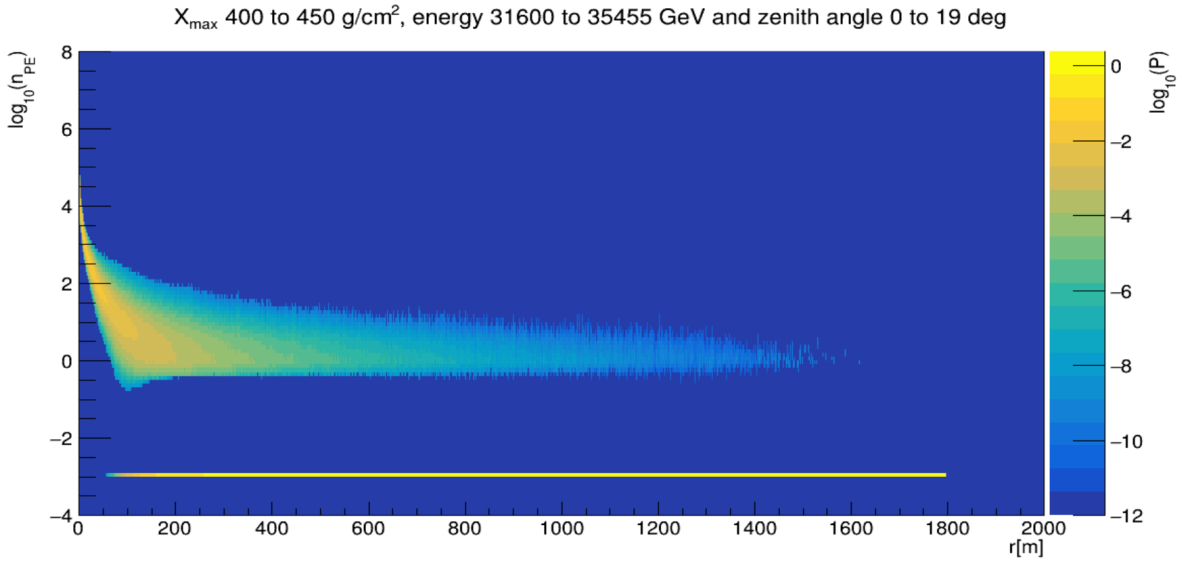

Figure 4.1: A1 template for the following binning: $400\frac{\mathrm{g}}{\mathrm{cm}^2} < X_{\max} < 450\frac{\mathrm{g}}{\mathrm{cm}^2}$, 31600 GeV $< E <$ 35455 GeV, $0° <$ zenith angle $\theta < 19°$. It visualises probability $\log(P)$ of triggering a certain number n_{PE} of photoelectrons at a given distance r from the shower core. In order for all features to be clearly visible, the template has been plotted up to a radius of 2000 m, while the complete template reaches up to 2600 m.

4.3 Shower Reconstruction Mechanism

As the expectations with regard to the detector array's response to showers with varying primary particle properties are set, one can move on to the actual reconstruction of said properties. At this stage, the incoming showers are simulated and thus the true shower properties are known. The reconstruction follows the steps outlined in [Jos+19] and is summarised in the following:

The fitting procedure of the primary properties of the EAS is conducted via a likelihood approach, which entails the minimisation of the following negative, log-likelihood expression:

$$log(L) = -2\sum_i \log(F(S_i(r_i, X_{\max}, E|\theta, \phi))) \tag{4.1}$$

F describes the probability that one measures a given signal S_i at a distance r_i from the shower core for a shower with set $X_{\max}$, E, θ and ϕ values. Here, ϕ describes the azimuth angle of the incoming γ-ray induced air shower and L describes the likelihood.

First, initial values of the positioning of the shower core, the energy, $X_{\max}$, θ and ϕ have to be established, which then can be introduced into the likelihood function as starting values and minimised. In order to obtain these initial fitting values for the x and y

position of the shower core, the centre of mass (COM) is determined by measuring all charges which are generated in the tanks in response to the EAS. This core guess can then be utilized in order to obtain an estimation with regard to the θ and ϕ angles of the incoming EAS. This is done by applying a curved shower front fit to the data that makes use of the differences in arrival times of the various measured signals, assuming that the shower core is placed in the previously calculated COM. As a result of this fit, which is also being reffered to as plane fit, a plane perpendicular to the shower front is calculated with which the θ and ϕ properties of the shower can be estimated.

Next, energy and $X_{\max}$ guesses are obtained with the help of Figure 4.2. First, the energy can be estimated by analysing the relationship between the number of triggered tanks, the distance between the shower core and the array centre, as well as the shower's energy. This relation can be derived for each configuration by investigating simulated shower data. Then, the $X_{\max}$ guess is obtained by relating $X_{\max}$ to the guessed shower energy, as also shown in Figure 4.2.

After all necessary starting values are now determined, the minimisation of Equation 4.1 can be conducted via the MINUIT minimisation algorithm [JR75] where a set number of 500 iterations was chosen. Thereafter, one obtains the $X_{\max}$, energy, and shower core position values in the minimum of the likelihood function as final fit values, while the direction is reconstructed by means of a second shower front fit after the likelihood minimisation. This time, the improved, fitted core position can be utilised in place of the previously used COM, which should allow for a more precise direction reconstruction. The reason for this predicted improvement in accuracy is that the shower front is fitted in relation to the estimated core position. An imprecise core estimation thereby changes the angle of the plane that is fitted perpendicularly to the shower front and thus changes the value of the fitted zenith and azimuth angles.

The fact that only reconstructed values have been used throughout the entire reconstruction process can be seen as an important step towards an even more realistic reconstruction procedure. Previously, true zenith and azimuth angles have been inserted into the likelihood expression as starting values, which only allowed for an idealized reconstruction procedure that would not be applicable in a real-world scenario.

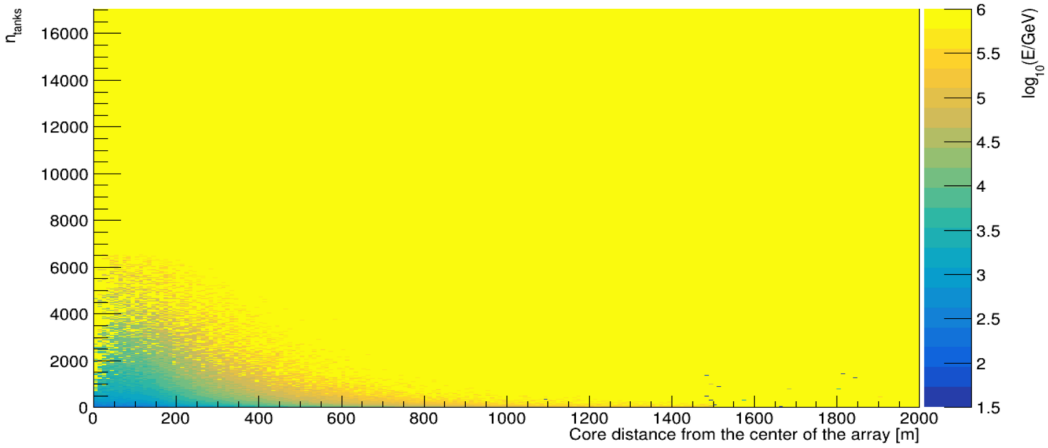

(a) energy guess

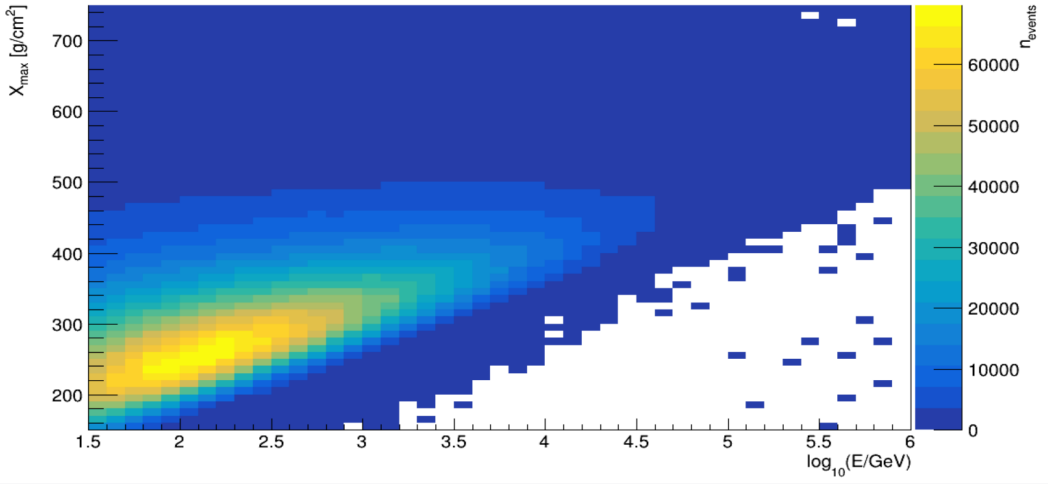

(b) $X_{\max}$ guess

Figure 4.2: Energy and $X_{\max}$ guesses, generated for the A1 configuration. For the energy guess, the number of triggered tanks n_{tanks} is plotted over the core distance from the array centre, while the z-axis indicates the energy. In case of the $X_{\max}$ guess, the $X_{\max}$ value has been plotted over the energy and the z-axis visualises the number of events n_{events}

5 SWGO Configurations

In this chapter, a subset of possible configurations for the SWGO detection site are expanded on. First, the reference configuration will be discussed which, as the name suggests, is a configuration that has already been simulated and analysed beforehand and can thus function as reference when assessing new possible array layouts. Then, the newly simulated M5 configurations are introduced and their respective properties compared with each other and the reference configuration. This chapter is meant to put the later analysis of the M5 reconstruction performance into perspective by showcasting the differences between the configurations and thereby elaborating why certain setups might be more advantageous or disadvantageous in certain energy or radius ranges.

All of the following configurations can be categorised based on two distinct components: The design of the Water Cherenkov tanks which detect the incoming particle shower and the distribution of these tanks on the surface of the detection site. The differences in tank design are described in Table 5.1 and shown in Figure 5.1. As can be seen, four of the six tank designs have two distinct cells. In each of those water-filled cells one PMT can be found. When the charged particle shower passes through the respective cell, Cherenkov light is generated in the tanks and can be collected by those PMTs. The photomultiplier that is placed in the upper cell (UC) of the tank is pointed upwards, while the PMT in the lower cell (LC) of the tank points down to the ground. The UC is significantly larger in volume than the LC and exclusively the UC is used in the creation of templates and reconstructive process for the array layouts which have double layered tanks, throughout this thesis.

Label	Number of layers	PMT type (UC, LC)	Diameter [m]	Depth (UC)	Depth (LC)
A	2	8”HQE, 8”	3.82	2.50	0.50
B	2	10”HQE, 8”	3.82	2.50	0.50
C	2	8”, 8”*	3.00	2.50	0.50
D	2	10”HQE, 8”	5.20	3.42	0.68
E	1	3×8”	4.00	1.70	-
F	1	10”HQE	5.20	4.20	-

Table 5.1: Enumeration of the tank design properties of the array layouts that are about to be discussed in this thesis. The following PMTs are used in the simulations: 8”: R5912, 8”HQE: R5912-100, 10”HQE: R7081-100. 8”*: 3”PMT and a wavelength shifter plate for costing. This PMT cannot be simulated at this stage and a 8” PMT is used instead (data taken from [Con+22])

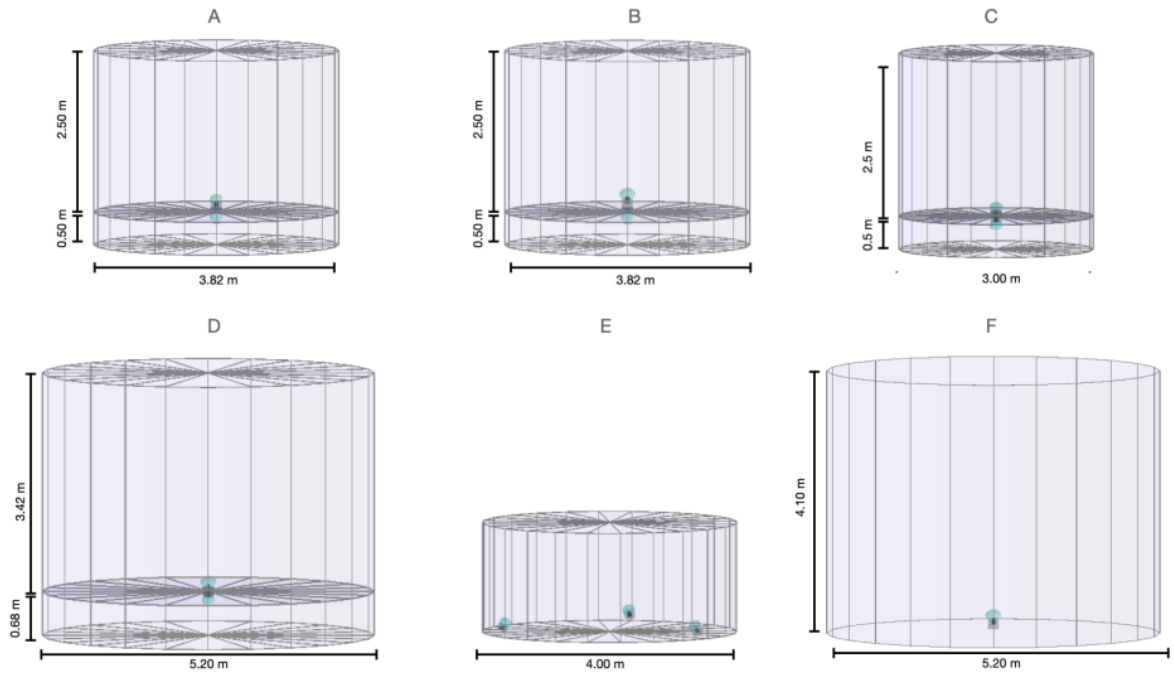

Figure 5.1: Sketch of the varying tank designs that are utilized in the M5 array layouts and the reference configuration. The diameter of the water tank and the depth of the upper and lower cells are indicated, while the placement of the PMTs is marked blue.

The tanks with the label E and F only have a single cell and can be used for comparison. In the case of the E tank design, three PMTs are placed near the outer walls of the tank and all point towards center of the ceiling, while the F tanks only contain one PMT which, similiarly to the UC of the double layered tanks, is placed in the centre of the tank floor and points directly upwards.

Another important feature of the tank designs is the type of their respective PMTs. The common denominator of all following configurations is that the cost of the setup is almost identical. As the photomultiplier is one of the more costly elements in the setup, it is therefore necessary to vary the PMT type in order to find the best possible compromise between PMT costs and reconstructive performance of the array. The types of the simulated PMTs are also listed in Table 5.1.

Apart from the design of the Water Cherenkov tanks, the placement of those tanks on the surface of the detection site is a determining factor behind the reconstruction performance of an array. As the possible cost is fixed at approximately 54 million USD [Abr+19], the number of water tanks is consequently limited. The question that then arises is: How can one place those tanks on the ground of the site as efficiently as possible, in order to both reconstruct cosmic ray air showers as precisely as possible, but also cover as much area as feasible? By covering a larger portion of the overall ground and thus measuring up to larger radii, one could also detect γ-ray air showers that otherwise would not pass through the active medium of the array. On the other hand, larger instrumented areas imply that the space in between those tanks is higher, which makes the reconstruction less efficient, as less overall data is gathered by the tanks within a given portion of the array. The layouts of the following M5 configurations thus differ in terms of their size (meaning the radius of the overall array) and the density of tanks in the inner and outer portion of the setup. This way, it is possible to assess the reconstructive performance of different types of layouts and compare them with one another.

5.1 Reference Configuration

As previously mentioned, the reference configuration has been simulated and analysed beforehand and operates as a reference in this thesis. In this setup, the array consists of an inner array in which the density of tanks, the so-called fill factor, is 80 % and an outer portion of the array with a fill factor of only 5 %, as shown in Figure 5.2. One generally expects the area with a higher density of tanks to reach a higher level of accuracy in both core and energy reconstruction, as more of the shower particles can be absorbed by the active medium of the array (the tanks) and can thus produce a measurable signal.

The reason for adding in an outer, less reconstructively efficient part of the array is that this makes it possible to also detect showers that fall down at larger radii from the array centre. Furthermore, highly energetic showers cover a larger overall area. By being also able to measure the extremities of such showers, it is therefore possible to better

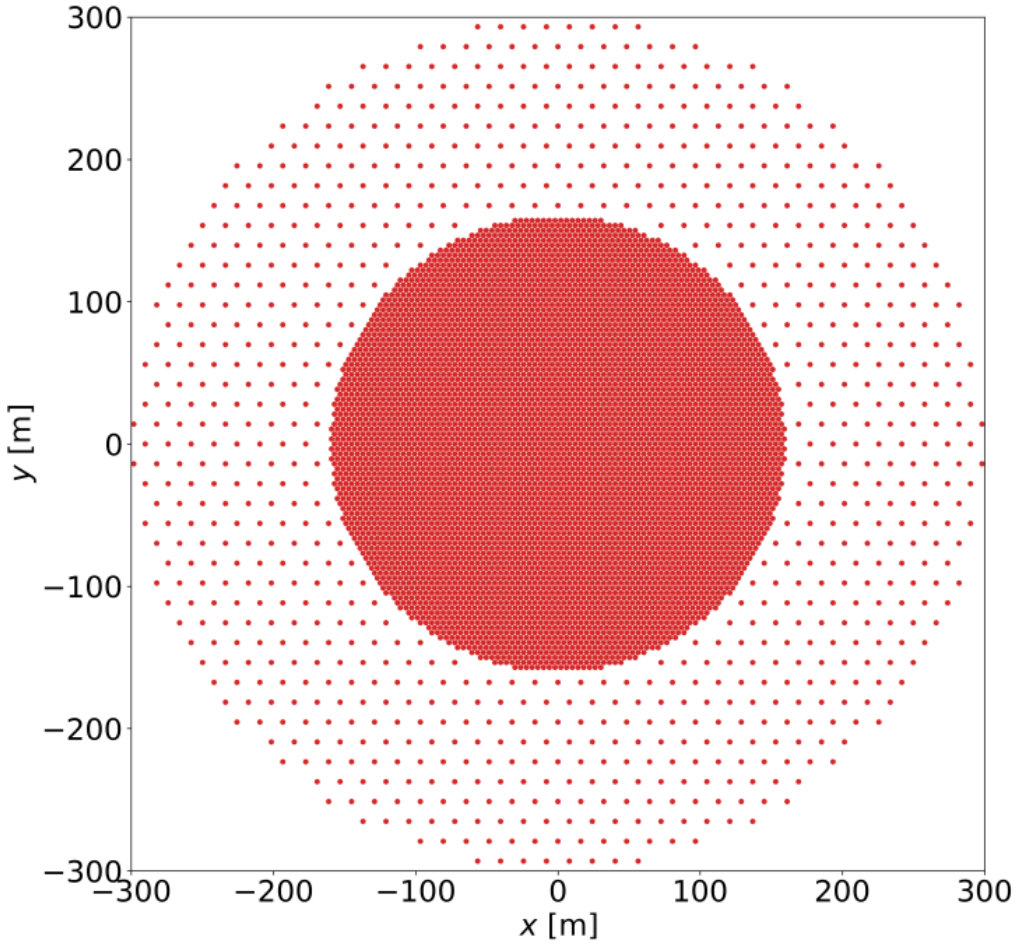

Figure 5.2: Sketch of the array layout of the reference configuration, consisting of an inner array with increased tank density and an outer array with decreased fill factor. Tank positions are indicated by red dots. (figure taken from [Lei21])

Config.	Zone 1			Zone 2			Zone 3		
	Fill factor [%]	Radius [m]	Units	Fill factor [%]	Radius [m]	Units	Fill factor [%]	Radius [m]	Units
A1	80	160	5731	5	300	858	-	-	-
A2	80	138	4303	2.5	600	2328	-	-	-
A3	80	138	4303	2.5	600	2520	-	-	-
A4	80	140	4429	4	400	1518	1.25	600	678
A5	40	234	6109	5	300	432	-	-	-
A6	88	162	6469	1	300	168	-	-	-
A7	80	101	2335	2.5	600	2394	0.63	1200	1842

Table 5.2: Radii, fill factors and tank unit numbers, enumerated for each zone of each A configuration. Zone 1 is always defined as the area around the centre of the array, while increasing zone numbers indicate more and more distant portions of the array (data taken from [Con+22])

assess the shower energy and core, as the entire distribution and width of secondary shower particles can be estimated more accurately. Furthermore, the tank density is less important at higher energies than for low-energy EAS, as more seondary shower particles interact with the array and can thus produce a signal.

5.2 M5 Configurations

In this thesis, seven configurations that utilize the A tank design and five array setups with different tank properties will be assessed. This way, the impact of the tank arrangement on the ground and the influence of the tank design itself can be evaluated separately. The label of each configuration is composed of a letter which indicates the given tank design in accordance with the labelling in Table 5.1 and a number that categorizes the configurations according to their layout approach, meaning the tank arrangement.

5.2.1 A Configurations

The A configurations A1, A2, A3, A4, A5, A6 and A7 all follow the previously mentioned A tank design from Table 5.1. Thus, they only differ in in terms of their respective array layout. Similarly to the already discussed reference configuration, the layouts consists of an inner, more densely filled, portion of the array and an outer portion with a significantly lower fill factor. The configurations A4 and A7 also possess a third zone with an even lower fill factor. For the sake of simplicity, the second and third zone of these two configurations are both referred to as the outer array in this thesis and are analysed together, while only the first zone is defined as the inner array of a given configuration. The exact fill factors, radii and tank unit numbers of all A configurations are listed in Table 5.2.

In Figure 5.3, the full layout of the A1 configuration can be seen, as well as a zoomed in image around the transition between inner and outer array. A1 is almost identical to the

reference configuration and can be used, in order to assess whether simulations dataset that is utilized for the analysis of the M5 configurations contains any major flaws. The only differences arise in terms of the PMT type and exact number of tank units in each zone. The reference configuration makes use of 8" photomultipliers, while 8"HQE PMTs are utilised in A1, in accordance with the PMT labelling from Table 5.1. Furthermore, the inner array of the reference configuration is composed of 4000 tanks, while 1000 further tanks are mounted onto the outer array, whereas 5731 tank units are part of the inner array of A1 and only 858 tanks would form the outer array. In case of properly set up simulation files, one expects the A1 configuration to perform similarly well to the reference configuration in each energy range, due to the similarities in array layout. On the other hand, major discrepancies between the reconstructive performance of these two configurations would indicate that the simulation dataset is inadequate and needs to be revisited. It is however important to note that the exact number and position of simulated showers for A1 and the reference configuration vary, which inevitably leads to some differences in performance.

The A2 configuration, visualised next to A4 in Figure 5.4, possesses a smaller inner array with a radius of only 138 m, while the full array has a significantly larger radius of 600 m than in the case of A1. Furthermore, the increase in overall array radius entails a decreased fill factor of 2.5 % in the outer array of A2, while 5 % of the area of outer array of A1 is covered with tanks.

The A3 configuration, which is shown in Figure 5.5, is almost identical to A2 in terms of the radii of the inner and outer array, the fill factors of each zone and the number of tanks in each part of the array. The only significant difference is that the outer tanks of A3 are set up in clusters of seven units each. The direct comparison between the reconstructive performance of A2 and A3 will therefore possible to assess whether the clustering of outer array tanks increases or decreases the reconstruction accuracy of the configuration, while maintaining the same overall covered area.

Similarities can also be oberserved between the radii of the inner and outer array of A2 and A4 and the number of tanks placed in both parts of the array of both configurations. The main difference between A4 and A2 is the fact that the outer array of the A4 configurations is split up in a second and third zone. That is a compromise between the advantage of having the same increased covered area in comparison to A1, while the fill factor of 4 % in the second zone permits for a higher level of reconstruction performance in that given part of the array, as more signal can be evualuated throughout the reconstructive process. The tradeoff for the increased performance in the second zone is a smaller fill factor and thus an expected decrease in performance in the third zone. Throughout the later analysis, the reconstruction accuracy of the second and third zone of the array is analysed in conjunction. Consequently, this makes it possible to assess whether a separation of the outer array into two array zones leads to an increase or decrease in overall outer array performance.

Figure 5.6 visualises the layouts of the configurations A5 and A6. In comparison to A1, A5 possesses a lower filler factor of only 40 % within the inner array of the configuration,

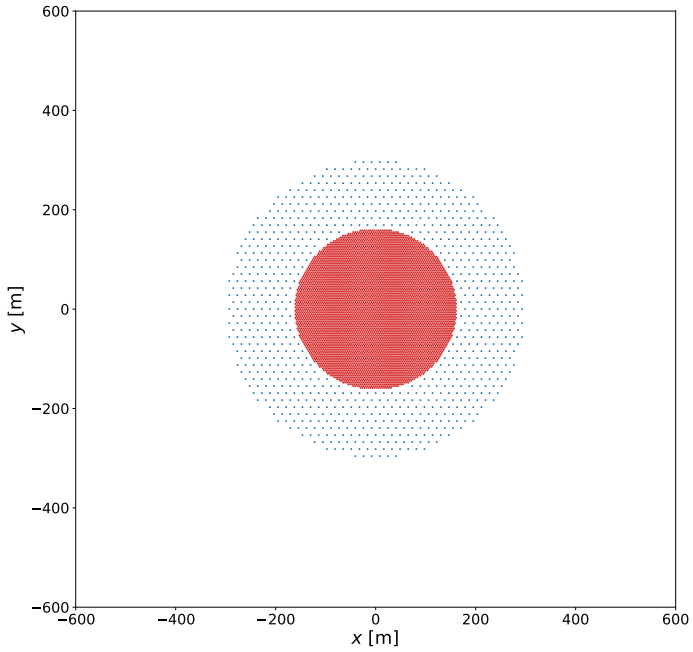

(a) A1, full array

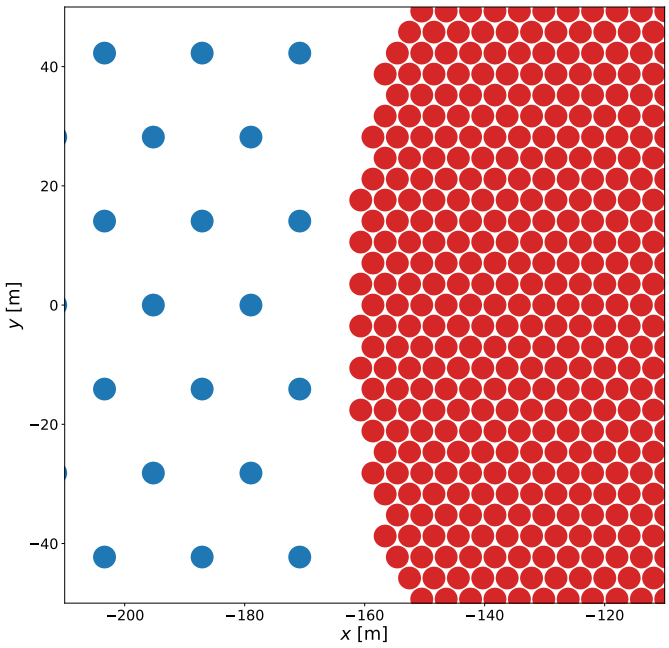

(b) A1, zoomed-in

Figure 5.3: Full and zoomed-in array of A1. Red dots represent inner array tanks, while blue dots indicate the placement of tanks in the outer array

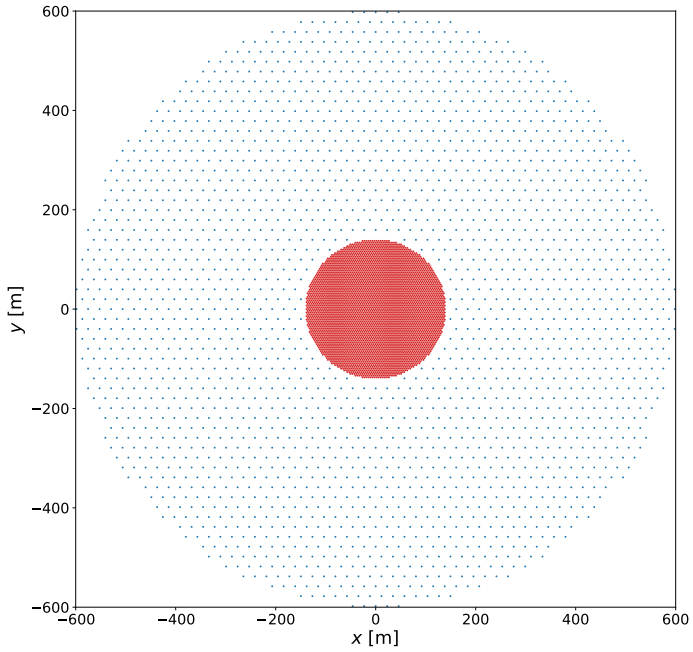

(a) A2, full array

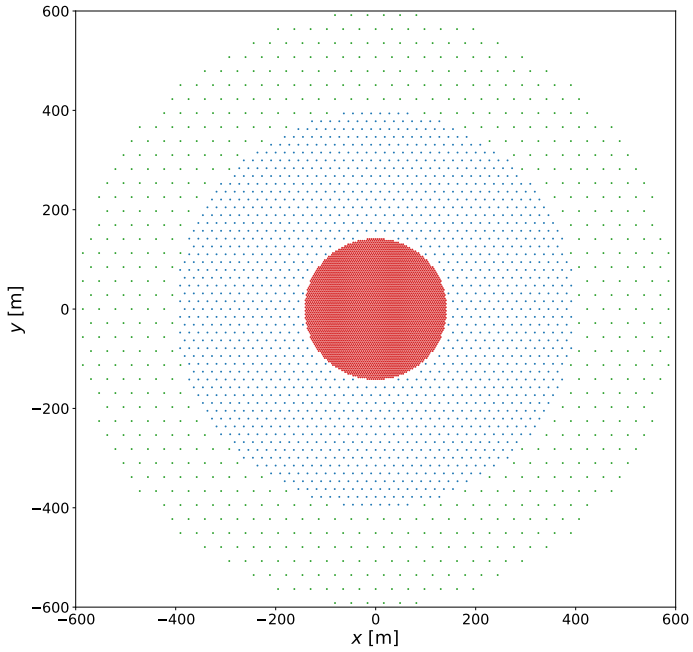

(b) A4, full array

Figure 5.4: A2 and A4 array layouts: The tanks are indicated by red dots in first zone, blue dots in the second zone and green dots in the third zone (A4 only).

while the radius of the first zone is significantly larger and measures up to 234 m, in contrast to an inner radius of 160 m for A1. The fill factor of the outer array of A5 is kept the same, but is now smaller in radius, as the overall radius of the array still measures 300 m. One would expect a decreased reconstruction performance of A5 within the inner array for small energies, due to the decreased tank density in zone one.

This expectation is based on the fact that small energy events have decreased density and width with respect to their distribution of secondary shower particles. If a given low energy event falls onto the inner array, the lower density of tanks in this zone of the A5 configuration would imply that a lesser proportion of the shower is absorbed by the array and consequently less information is gathered that can be used when reconstructing the shower. Due to the fact that less overall secondary shower particles can be evaluated in the first place, tank density is more important at low energies. However, this expectation changes for high energy events. In this case, the larger overall area in which the shower components hit the ground implies that a higher proportion of the event can still be absorbed by the inner array of A5, while the same might not be the case for A1, due to the decreased radius of the inner array. Here, the advantage of having a higher inner array radius might compensate for the decrease in tanks density and lead to an overall increase in reconstruction performance.

Also, a higher portion of the incoming showers fall on the inner array that would have fallen on the outer array of A1. Thus, these showers are expected to be reconstructed much more accurately than in the case for A1. The interplay of these mentioned advantages and disadvantages of the higher inner array radius and decreased fill factor is of special interest throughout the analysis of the reconstruction performance of A5 in comparison to A1.

On the other hand, A6 has an increased inner array fill factor of 88 % which should imply a high level of reconstructive performance in the inner array. However, the fill factor of the outer array is only 1 %, which is significantly lower than for the previously mentioned array layouts. Consequently, one expects a decreased level of accuracy for the A6 configuration in that portion of the setup. Thereby, it is interesting to assess whether the increase in reconstructive accuracy in the inner array in combination with the decreased accuracy of the outer array results in a better or worse performance of the array overall.

Finally, Figure 5.7 visualises the tank arrangement of the A7 configuration. Similarly to A4, it consists of three zones with decreasing fill factors. However, in the case of A7, the radius of the full array ranges up to 1200 m, resulting in relatively low fill factors of 2.5 % and 0.63 % respectively for zone two and three. One therefore expects the reconstructions in the outer array to be relatively inefficient and the reconstructive accuracy thus to be low in comparison A1.

On the other hand, the array is supposed to detect a significantly larger number of overall events, due to its increased effective area. Within the inner array, the author expects the performance to be similarly good to A1 for lower energ events. The inner array radius

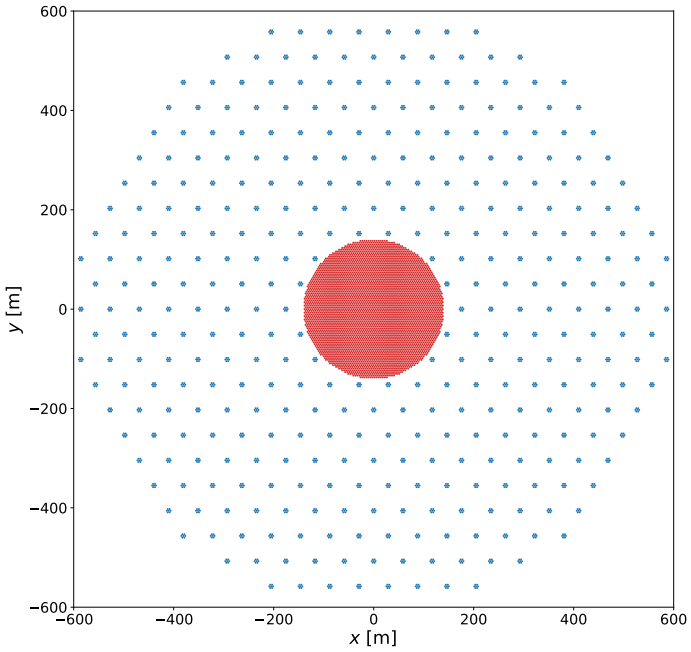

(a) A3, full array

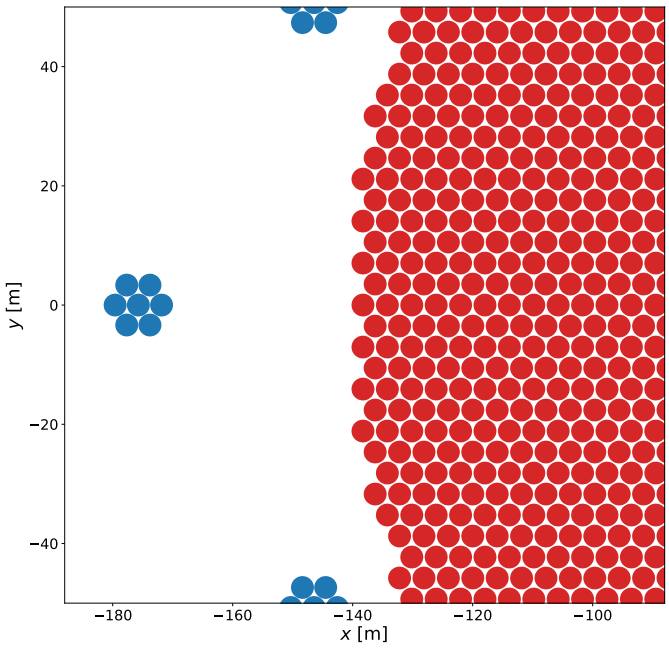

(b) A3, zoomed-in

Figure 5.5: Full and zoomed-in array of A3. Red dots represent inner array tanks, while blue dots indicate the placement of tanks in the outer array, which are set up in seven unit clusters

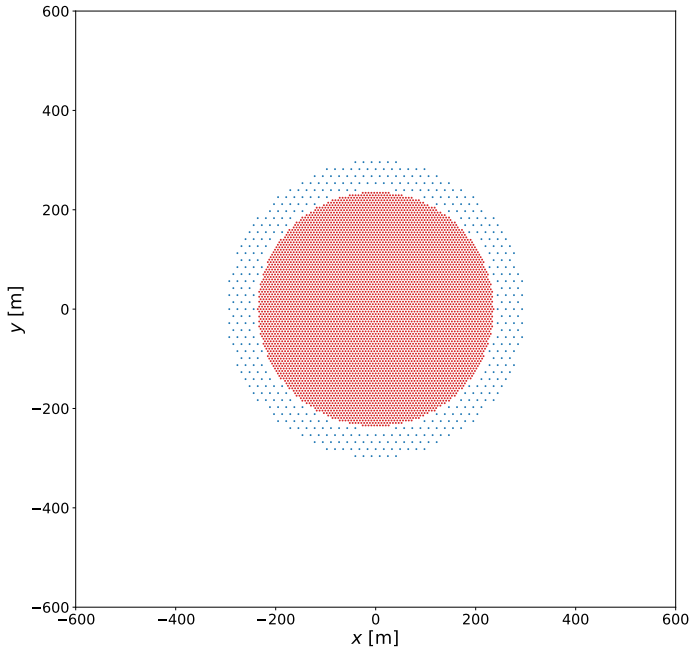

(a) A5, full array

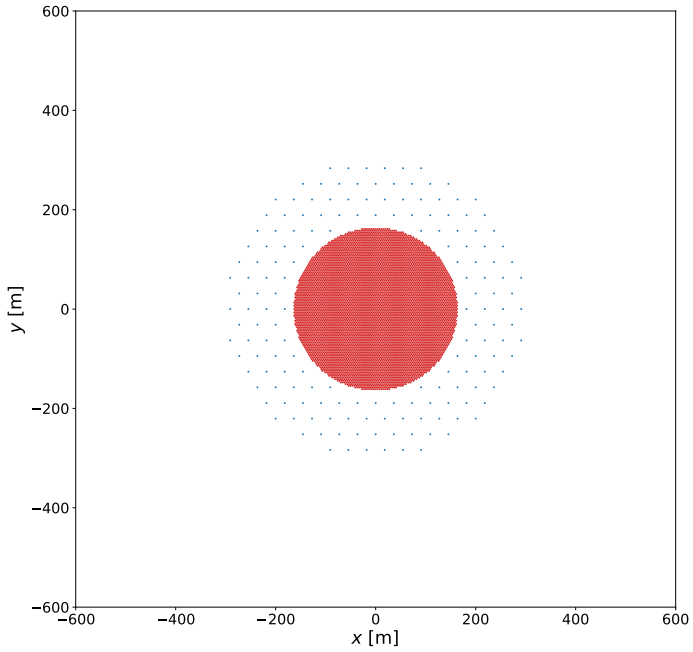

(b) A6, full array

Figure 5.6: Sketch of the A5 and A6 array layouts. The Water Cherenkov tanks are indicated by red dots in the inner array and blue dots in the outer array.

Config.	Zone 1			Zone 2		
	Fill factor [%]	Radius [m]	Units	Fill factor [%]	Radius [m]	Units
A1	80	160	5731	5	300	858
B1	80	150	4303	5	300	888
C1	80	158	9043	5	300	1398
D1	80	189	4429	5	300	372
E1	80	171	6109	5	300	738
F1	80	213	6469	5	300	306

Table 5.3: Radii, fill factors and tank unit numbers, enumerated for each zone of the array layouts A1, B1, C1, D1, E1 and F1. All of the mentioned array layouts have only two separate zones (data taken from [Con+22])

of 101 m should, however, imply a decreased reconstruction efficiency for higher energy events. In that case, the area onto which the components of such high energy showers fall is expected to oftentimes exceed the boundaries of the inner array. Thus, parts of the shower would land on the significantly more inefficient outer array and decrease the overall performance of the configuration in the higher energy range.

5.2.2 1 Configurations

Instead of keeping the tank design identical and varying the tank arrangement on the surface of the detection site, it is also possible to investigate configurations with different tank designs and similar array layouts. In the case of the M5 configurations, the setups A1, B1, C1, D1, E1 and F1 all are similar in tank arrangement, while the tank changes in accordance with the labelling seen in Table 5.1. In this thesis, the mentioned setups will be referred to as 1 configurations. As a consequence of the ressemblance in terms of their respective array layouts, the mentioned configurations only possess two zones, as seen in Table 5.3.

In Figure 5.8 the array layout of the B1 and C1 configurations are shown, as A1 has already been discussed beforehand. Similarly to A1 and all following configuration, the fill factor of the inner array is 80 %, while 5 % of the outer area of the array is filled with Water Cherenkov tanks. The main difference between the B1 and A1 configurations is that the latter features a larger 10” HQE PMT in the upper cell, while the PMT in the lower cell and the dimensions of the tank are kept the same. As the costs of all configurations are similar, the number of overall tank units in the B1 configurations is decreased. Here, it shall be investigated if the advantages of having a larger PMT, which consequently can be more sensitive to low energy events, outperforms the setup with the smaller 8” HQE PMT, but more tank units.

On the other hand, the C1 configuration features a less expensive 8” PMT in the upper cell and a decreased tank diameter of 3.00 m, opposed to the 3.82 m of diameter for A1

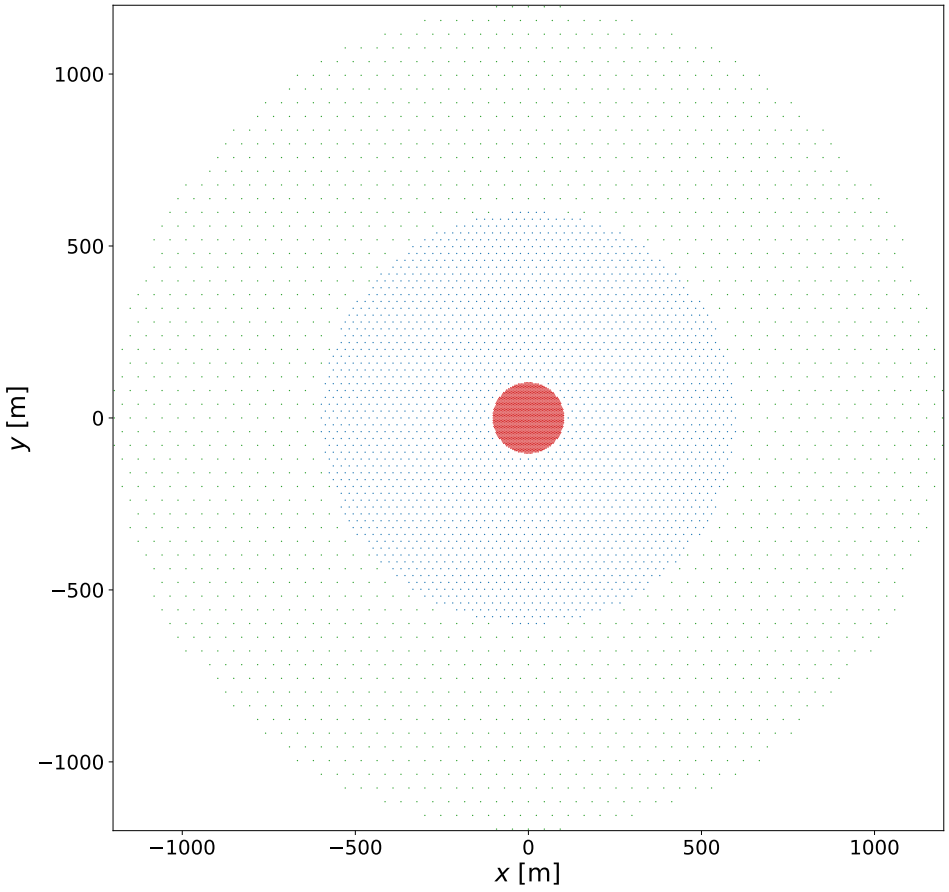

Figure 5.7: Sketch of the A7 array layout. The Water Cherenkov tanks are indicated by red dots in the first zone, blue dots in the second zone and green dots in most outer third zone, which reaches up to a radius of 1200 m.

and B1. Consequently, the number of tanks is higher. Investigating the reconstructive performance of C1 and comparing it to A1 and the D1 configuration, which is shown in Figure 5.9, will make it possible to assess the impact of the tank dimension and analyse whether a setup with less bigger tanks or more smaller tanks is advantageous.

The mentioned D1 configuration possesses a larger tank than A1 with a tank diameter of 5.20 m and an increased depth of its respective upper and lower cells. Due to the increased tank diameter, the number of D1 tank units is smaller compared to the previously mentioned configurations and thus the number of utilized PMTs is decreased. Consequently, because the PMTs are one of the more costly components of each setup, the D1 configuration can make use of the superior 10"HQE PMTs in its upper cell. The interplay between varying tank sizes, numbers of tank units and PMT sizes can therefore be investigated when comparing the reconstruction performance of A1, B1, C1 and D1 in chapter 6.

One generally expects larger PMTs to be more sensitive to low energy events, as less Cherenkov light is needed, in order to produce a signal in the PMT. That advantage of the larger, superior PMTs is expected to decrease at higher energies, as the overall incoming signal is higher. On the other hand, it can pe expected that configurations with a larger number of tanks are able to reconstruct the core position of the incoming showers more accurately, as the signal in a higher number of tank positions can be read out and used throughot the reconstruction process. Therefore, it would be possible to weigh the signal of more detectors and predict more accurately where the core of the shower landed.

Finally, the layout of the E1 and F1 configurations is visualised in Figure 5.9 and Figure 5.10, the tank designs of which are only composed of a single cell. In the case of E1, three PMTs are positioned inside each tank, while one PMT finds itself in every F1 tank. The F1 configuration features relatively large tanks with a diameter of 5.20 m and a depth of 4.20 m, while the diameter of the E1 tanks measures up to 4.00 m. The depth of E1 is the lowest out of all investigated configurations with a value of 1.70 m. The simulation and analysis of E1 and F1 will make it possible to compare the performance of single-layered configurations with the previously mentioned double-layered setups. Due to their similar tank dimensions, a direct comparison between the double-layered D1 configuration and the single-layered F1 setup can be made, while the E1 tanks are similar to the Water Cherenkov tanks that were utilized for HAWC, as previously shown in Figure 3.2, and can thus function as a reference.

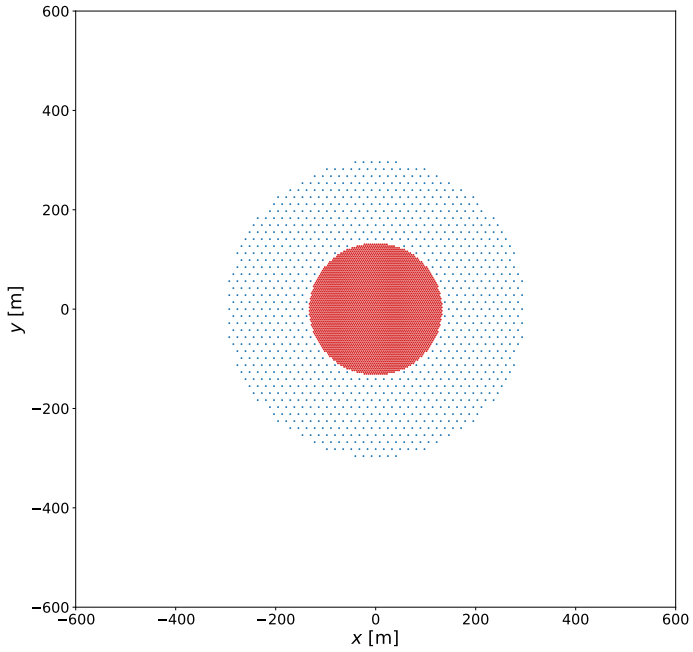

(a) B1

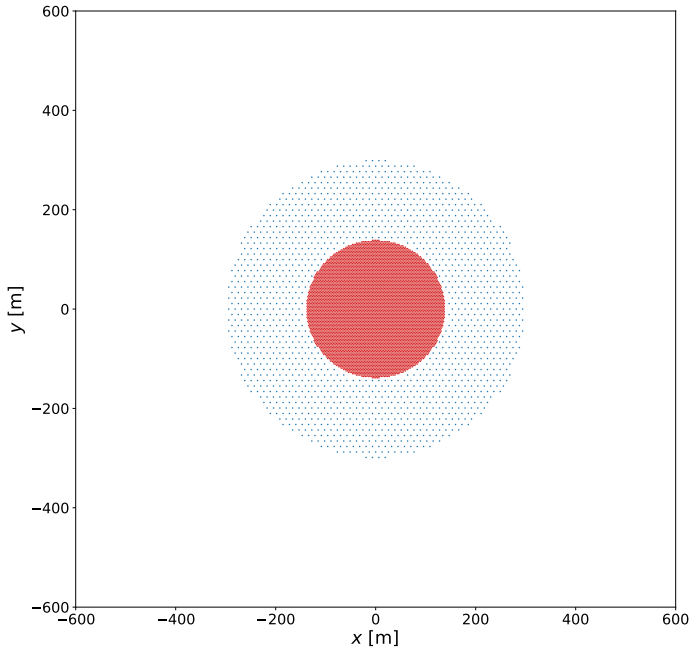

(b) C1

Figure 5.8: Sketch of the B1 and C1 array layouts. The Water Cherenkov tanks are indicated by red dots in the inner array and blue dots in the outer array.

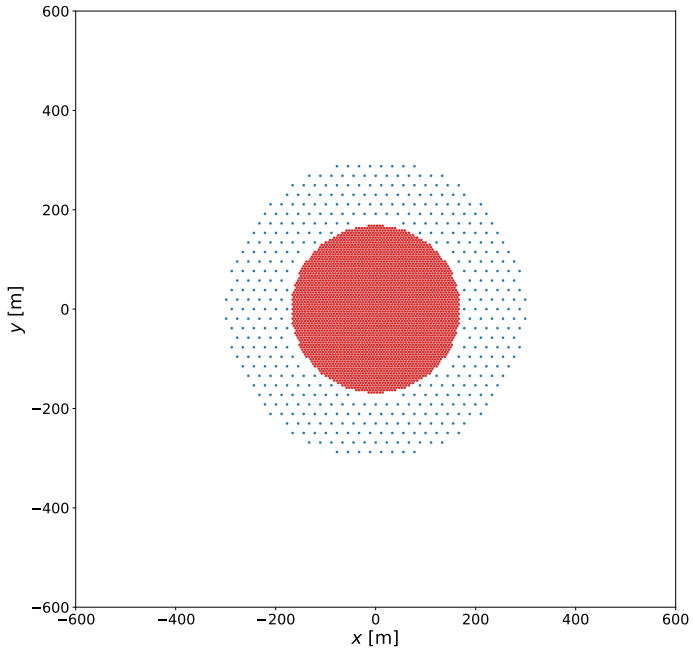

(a) D1

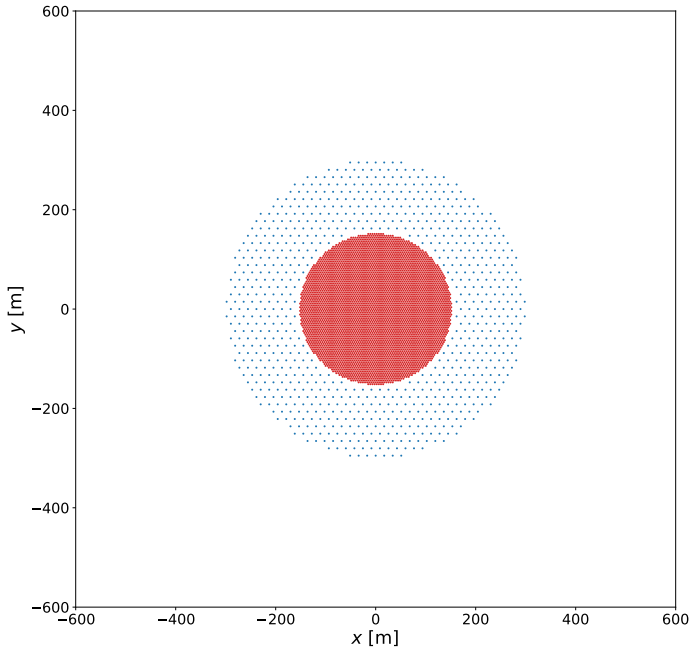

(b) E1

Figure 5.9: Sketch of the D1 and E1 array layouts. The Water Cherenkov tanks are indicated by red dots in the inner array and blue dots in the outer array.

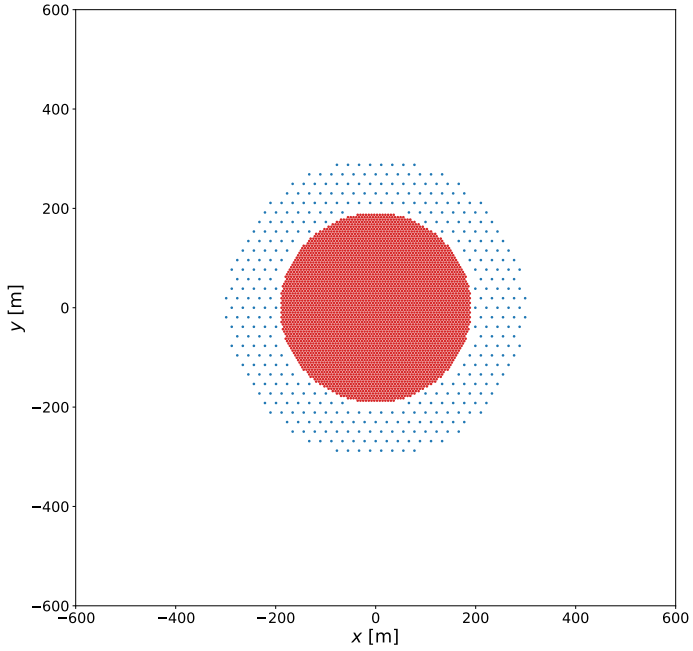

Figure 5.10: Sketch of the F1 array layout. The Water Cherenkov tanks are indicated by red dots in the first zone, blue dots in the second zone.

6 Performance Evaluation of the M5 Configurations

In this chapter, the performance of the reconstructive accuracy of the M5 configurations shall be discussed. The reconstruction of the shower core is assessed by means of the core resolution, the energy is evaluated through the configuration's energy resolution and energy bias and the angular reconstruction is gauged with angular resolution and bias plots. In the following, the workings of such core, energy and angular evaluation is explained and the performance of each of the mentioned M5 configurations is assessed and compared to the remaining setups.

6.1 Data Comparison and Applied Cuts

Before analysing the performance of the M5 configurations, the applied cuts shall be discussed first. Only EAS with zenith angles θ at and below 45° that generated at least one photoelectron in more than 25 tanks have been taken into consideration. This tank number condition had previously been chosen for the reference configuration and was applied to all configurations for the sake of comparibility. For more detailed investigations, one could optimise this condition for all configurations and investigate the reconstructive performance again. It is however important to mention that the tank condition mainly affects the resolution curves at lower energies. As high-energy EAS generate more signal within the tanks, the condition does no longer visibly impact the performance after a certain energy values. However, this energy value might vary, depending upon the tank design and array layout of each given configuration. As the SWGO is set to mostly operate in the TeV range, the conclusion that can be drawn throughout the analysis for high-energy showers are expected to not be significantly affected by this cut.

Furthermore, the core, energy and angular performance of the arrays will only be analysed for EAS whose true core position falls onto each respective array, so far. The reason for applying this cut to true core and not reconstructed core positions stems from the fact that the latter would also include showers with true core positions outside the confinements of the array. Consequently, these showers would be indistinguishable from showers with true core positions inside the array, and by extension decrease the plotted reconstruction performance. For a more realistic reconstruction procedure, one could define a parameter which quantifies the quality of each given fit and exclude showers that are reconstructed inaccurately by that parameter, instead of setting cuts based on

the true core position of each EAS. As a consequence, EAS that would fall outside the array and are thus reconstructed inaccurately could be excluded, similarly to the cut applied in this thesis. Such a parameter and cut could be implemented in the future and be seen as a further step towards an even more realistic shower reconstruction, but has not been brought about so far.

In Figure 6.1a the number of events that make it past the cut is plotted over the radial distance r from the centre of the array for all A configurations. As the area increases proportionally with r^2, the number of events has been divided by r^2, in order for the differences in area of the respective r bins to not affect the event distribution. It is visible that the tank arrangement impacts the number of events that are evaluated, as the fill factors and radii vary between inner and outer arrays of the given configurations. For instance, A5 has a tank density of only 40 % within the inner array, but also posseses the largest inner array with a radius of 234 m. This is visible in the plot, as the number of events near the centre of the array is smaller in comparison to the remaining M5 configurations, because less showers fulfill the cut due to the low fill factor. On the other hand, the peak of the A5 event distribution has a wider spread that can be explained by the increased inner array size. A noticeable exception can be found in the reference configuration for which only 10.000.000 EAS have been simulated, while 250.000.000 shower simulations were conducted for the new M5 setups. Furthermore, only showers up to smaller radii have been simulated for the reference configuration, which minifests itself in a visible radius cutoff.

Figure 6.1b shows the number of events plotted over the true energy of the EAS for each of the the A configurations. It is visible that larger setups like A7 are geared more towards high-energy showers, which cover a larger overall area, as the extremities of such high-energy showers can still potentially be detected within the boundaries of the array. Also, the A7 fill factor between 600 m and 1200 m of radius is only 0.63 %, implying that low energy showers that fall onto this portion of the setup are less likely to fulfill the previously mentioned tank condition. In order to detect low-energy EAS, one prefers setups with large inner arrays and high fill factors, as the density of secondary shower particles is lower and the EAS covers a smaller area. Therefore, a higher tank density is needed for these events to still generate enough signal within the water tanks.

6.2 Core Reconstruction

The performance assessment will be started by an evaluation of the core reconstruction, which determines the accuracy of the later plane fit and thus of the direction reconstruction, as elaborated upon in section 4.3. Therefore, improving the accuracy with which the core position is reconstructed can be seen as an important step towards an improved direction reconstruction.

In order to assess the quality of a given core reconstruction, the distances between

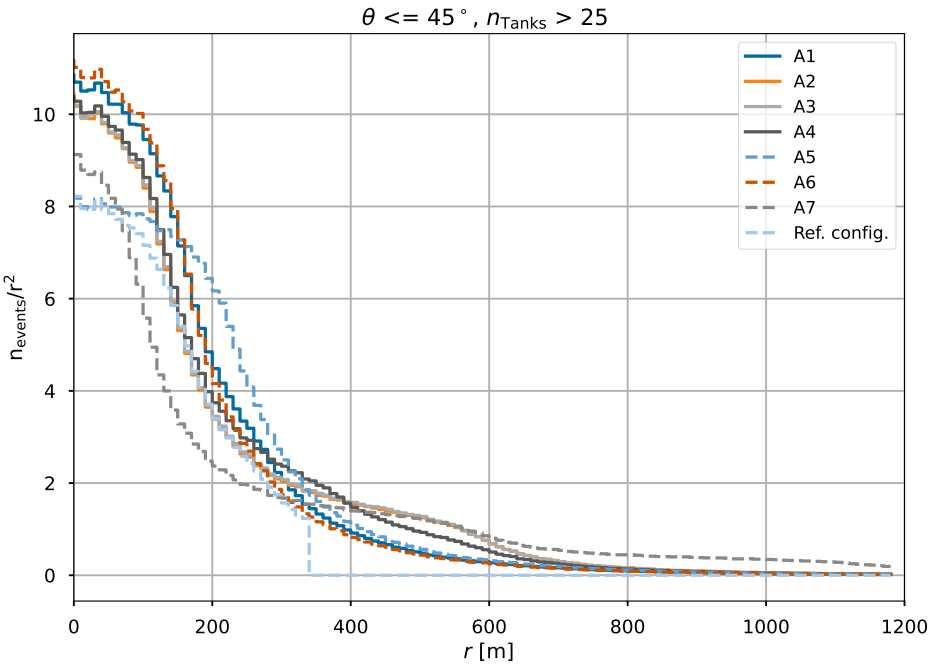

(a) Radial shower core distribution

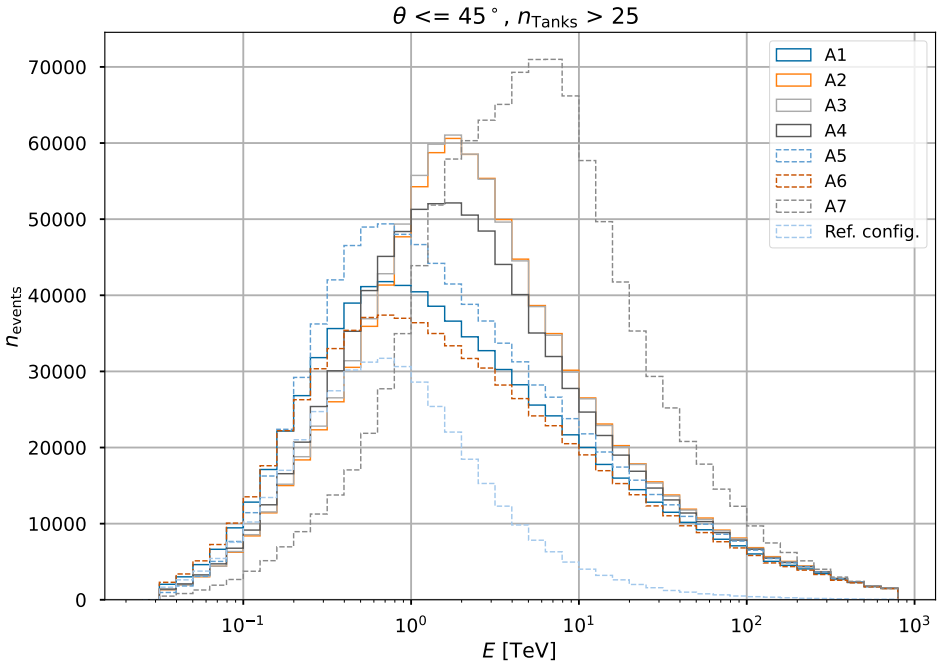

(b) Energy distribution

Figure 6.1: Radial shower core, divided by the squared radius r^2, and energy distributions of all events that trigger the zenith angle condition $\theta >= 45°$ and $n_{\text{Tanks}} > 25$ for each A configuration and the reference setup

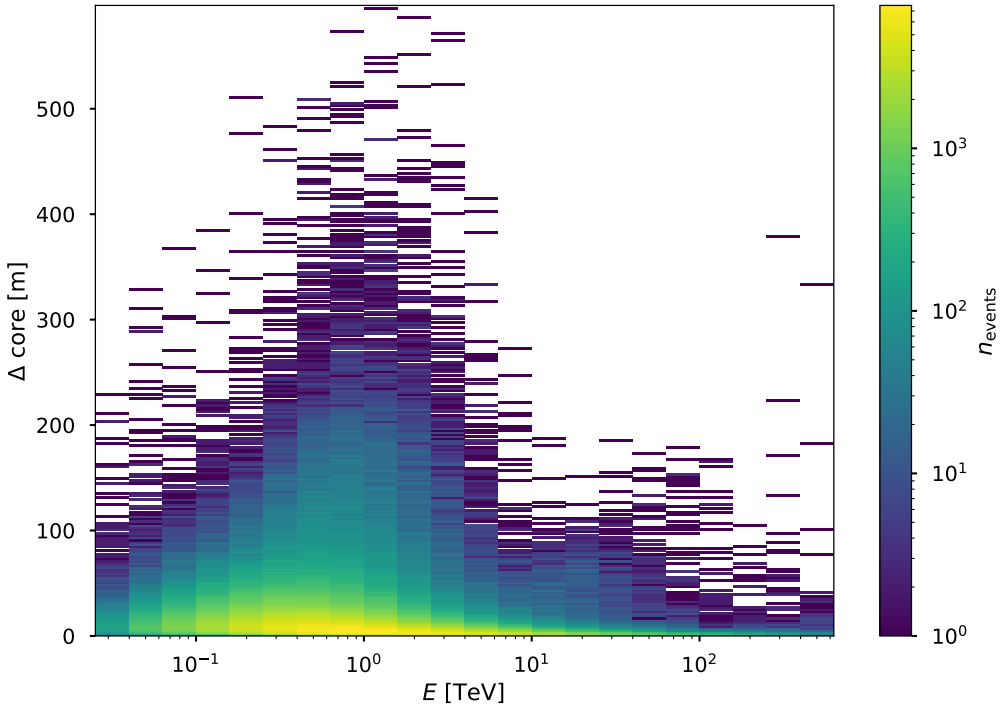

Figure 6.2: Histogram with which the core resolution of the A1 configuration can be computed. The distance between the reconstructed and true shower core is plotted over the energy, while the number of events is showcasted by the colorbar. Only showers whose core position lies within the array have been taken into consideration

reconstructed and true shower cores are plotted in a histogram over the true shower energy, as seen in Figure 6.2 for the A1 configuration. This makes it possible to assess the core performance within various energy ranges. In the next step, the core resolution can be computed, which is a measure of the precision of the core reconstruction, by calculating the 68 % containment radius of the distribution of distances between true and reconstructed shower cores for each energy bin.

Assuming a nearly Gaussian distribution, one can calculate the error of this core resolution in accordance with [SJ03] to be

$$\frac{\Delta core_{\ 68\ \%}}{\sqrt{2(n_{\text{events}}-1)}} \tag{6.1}$$

for a number of n_{events} in each energy bin, which will be indicated by the error bars.

Smaller core resolution values thereby indicate that the distance between reconstructed and true shower core positions is smaller and thus that the reconstruction has been more precise. In the following, the core resolution shall be assessed for the A and 1 configurations. By investigating the A configurations, one shall inspect the effect of the differences in array layout on the core performance, while the analysis of the 1 configurations makes it possible to see how different tank designs impact the core reconstruction for layouts similar to A1. Showers whose core falls on the inner array of a given configuration and EAS that fall on the outer array are investigated separately, before assessing the core resolution of both sets of showers in conjunction. By analysing the core performance in both portions of the array separately, one can determine how the radii and fill factors of both zones contribute to the core performance of the entire array, while the analysis of all showers, which fall onto the array, makes it possible to assess the overall core performance of each configuration.

6.2.1 A Configurations

When investigating the core resolution for inner and outer array showers, shown in Figure 6.3, one first compares the performance of the reference configuration and A1 with one another, in order to exclude major flaws in the simulations and reconstructive procedures. As explicated in chapter 5, A1 and the reference configuration are almost identical and differ only slightly in terms of the number of tank units in the inner and outer array and the utilised PMT. In A1, a 8"HQE photomultiplier is used, while the reference configuration features the inferior 8" PMT. Due to superior photomultiplier and the fact that less shower data has been simulated and thus less statistics are available for the reference configuration, one expects a slight increase in performance throughout all energy ranges for A1, but no major discrepancies. The curves for A1 and the reference configuration confirm this assumption.

When looking at showers whose core falls onto the inner array of each setup, one can observe that differences in core performance between the configurations decrease with increasing energies and that the core resolution value decreases as a whole for rising energies. The higher density of tanks in the inner portion of the setup implies that more signal can be generated by a given shower. More signal by extension implies that the reconstructive performance improves. Considering the additionally increased signal due to higher shower energies, the decrease in differences between reconstructed and true shower core positions for high-energy showers can be explained.

On the lower energy end of the curve, one can see that A5 and A7 seem to perform the best, while A6 and the reference configuration show decreased core performance. A5 has a relatively low inner array fill factor of only 40% in comparison to the 80% fill factor of the remaining layouts, apart from A6. On the other hand, the radius of the inner array of A5 measures up to 234 m, which is the highest value out of all configurations. Therefore, one could hypotesize that a decrease in inner array fill factor from 80 % to 40% could be more than compensated by an increase of the inner array diameter. This feature could

be assessed further in the future, in order to investigate if lowering the inner array tank density even further, while increasing the radius could be even more benefitial.

The reason for the link between inner array size and performance at lower energies could be explained by the fact that the proportion of showers which land on the edge of the inner array is decreased for larger inner array sizes. Thus, the fraction of events that can be reconstructed less accurately, as then outer array tanks contribute to the reconstruction, would also be decreased, resulting in improved performance. On the other hand, the lower core performance of A6 could similarly be theorised to happen due to the fact that the outer array of A6 has a relatively low fill factor of only 1 % and thus showers that land on the edge of the inner array are reconstructed less accurately, as the outer array is then contributing to the reconstruction and can gather less signal due to its low tank density, in comparison to the other layouts.

A characteristic feature in all core resolution curves is the increase in performance at the low-end of the energy distribution, which can be explained by the applied tank condition. Increasing the tank condition leads to a decreased resolution for small energies. That can be explained by the fact that more showers with low signal are cut out of the evaluation. As these showers are usually reconstructed inaccurately, this cut results in overall improved performance. The same feature will also become apparent throughout the energy evaluation in section 6.3, which can be traced back to the same explanation. At higher energies, the overall amount of signal is higher, which implies that the trigger condition does not significantly affect the performance curves past a certain point.

When looking at showers that fall onto the outer array, also shown in Figure 6.3, one quickly observes that A6 and A7 perform significantly worse than the remaining layouts. This can be explained by the fact that both configurations have relatively low outer array fill factors, which thus imply that less data can be taken. In turn, the decrease in information consequently leads to inferior reconstruction performance. However, it can be seen that A7 performs well below approximately 2 TeV. This can be explained by the fact that the outer array of A7 is split into two distinct zones with fill factors of 4 % and 0.63 %. It can be assumed that low energy events only fulfill the tank condition if they fall onto the portion of the outer array with the 4 % fill factor. Consequently, as the energy is increased and showers that fall on the 0.63 % zone of the array are also then also fulfilling the condition, the overall performance decreases.

Furthermore, the comparison between A1 and A2, A3 and A4 shall be made for outer array events, as the latter configurations range up to 600 m of radius in comparison to the 300 m of radius of A1. One would like to investigate how the decrease in size of the inner array from 160 m to 138 m and the outer array fill factor from 5 % to 2.5 %, along with the increased size of the overall array affects the reconstructive performance of the respective arrays. One can see that A2 performs worse at lower energies than A1, as low-energy showers are affected more strongly by the decrease in tank density, due to the smaller spread of such showers and decreased secondary particle densities. However, the overall increased array size enables A2 to reconstruct the core more accurately at the high-end of the energy range above 100 TeV, as the extremities of these high-energy

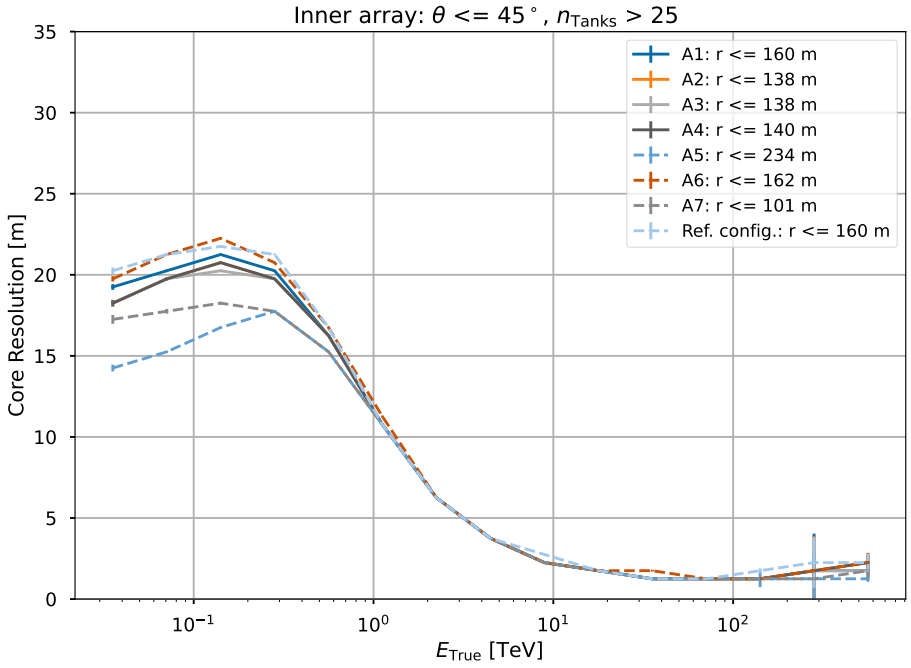

(a)

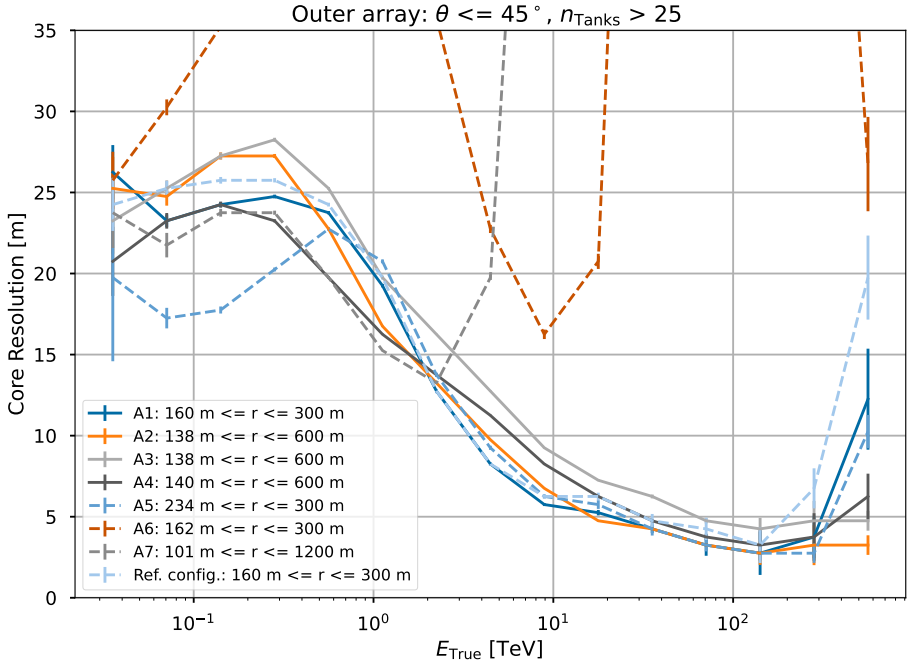

(b)

Figure 6.3: Core resolution, defined as the 68 % containment radius of the distribution of distances between real and reconstructed EAS core, plotted for the A configurations. Showers that fell on the inner array (a) and outer array (b) are shown separately.

showers can then also be detected by the array, due to the increase in area of the detection site. A3 behaves similarly to A2, as the only significant difference between those two setups can be found in the outer array tank arrangement. In case of A3, the tanks are set up in clusters of seven units each, while the A2 tanks are distributed evenly. It is noticeable that A3 performs slightly worse than A2 througout all energies above 100 GeV, as the core position might oftentimes fall right in between those clusters, which results in a decrease in performance.

A4 is also set up similarly to A2, but the outer array is divided into two seprarate zones. One of these zones has a fill factor of 4 %, while the more distant portion of the outer array possesses a tank density of 1.25 %. For lower energies, A4 performs better than A2, due to the fact that mostly showers that fall on the denser zone of the outer array trigger the necessary condition that more than 25 tanks need to be hit. In that case, the fact that this portion of the array has a fill factor of 4 % makes it perform better than A2 with its outer array tank density of 2.5 %. However, at higher energies above 3 TeV A2 performs better as A4, as the more distant portion of the outer array of A4 decreases the performance of the setup due to its smaller tank density.

The slight increase in core resolution after approximately 200 TeV can largely be explained by a lack of statistics, as confirmed by the error bars. Therefore, performance-related conclusion cannot be drawn for energies above 200 TeV throughout this thesis, which could be investigated in more detail in the future.

When assessing the core performance of the entire array, which is shown in Figure 6.4, one can see that the decreased outer array core performance of A6 and A7 severly impacts the core reconstruction of the entire array. On the other hand, the A5 configuration still performs best throughout all energy ranges due to the previously outlined reasons. Thus, one could regard an increase in inner array size as benefitial with regards to its impact on the core reconstruction, despite the decrease in fill factor from 80 % to 40 %. With regards to the A2, A3 and A4 configurations, one can still conclude that A4 performs best at lower energies below 2 TeV, while A2 is superior at the high-end of the energy range above 3 TeV. Furthermore the clustering of the outer array tanks, as seen for A3, seems to lead to inferior core performance throughout all energy ranges. The slight increase in resolution for high-energy EAS, that has been recognised throughout the outer array analysis, also persists to be visible for the same statistical reasons. It is important to mention that the cut conditions would need to be optimised for each of the configurations, in order for a completely fair comparison to be possible. Thus, no defintive conclusions can be drawn at this stage and this thesis can rather be seen as a first preliminary analysis.

6.2.2 1 Configurations

In this section, the core performance of the 1 configurations will be investigated. These configurations have different tank designs, but similar array layouts, as explained in

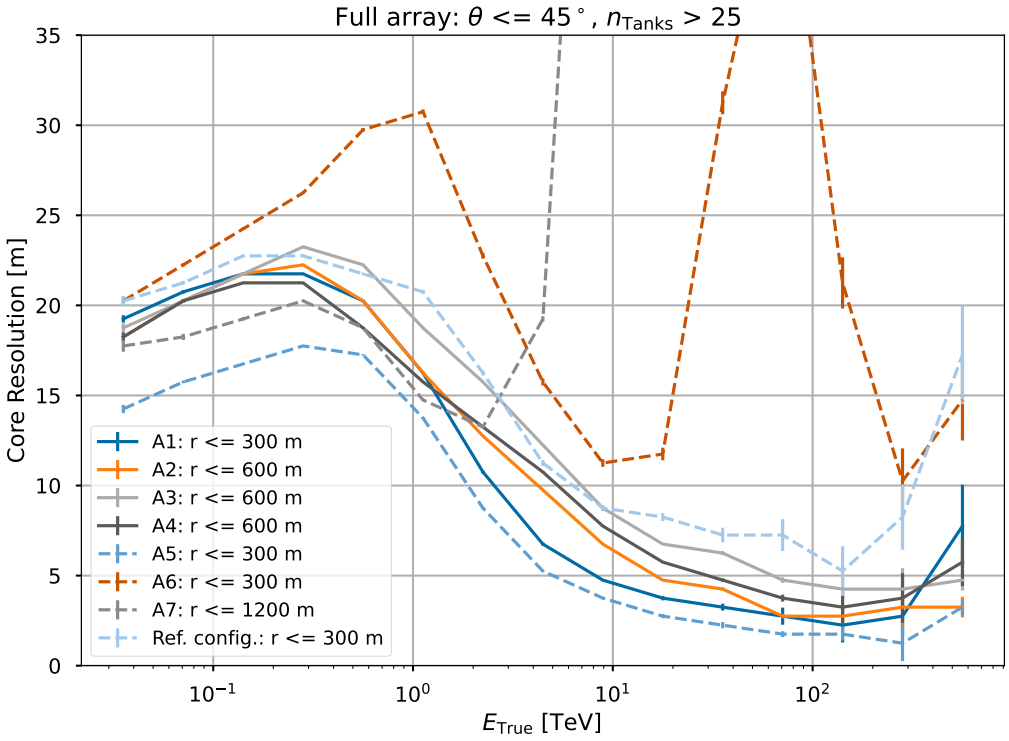

Figure 6.4: Core resolution, defined as the 68 % containment radius of the distribution of distances between real and reconstructed EAS core, plotted for the A configurations. All showers that fell onto the array have been taken into consideration.

further detail in chapter 5. Thus the effect of differing tank designs on the reconstruction performance can be evaluated. One observes that E1 performs worse than the remaining configurations at lower energies below 1 TeV for both inner and outer array showers, as visualised in Figure 6.5. This performance decrease could happen due to the tank condition $n_{\text{tanks}} > 25$ and the fact that E tanks contain three PMTs within each unit. Thus, the tank could be more sensitive to the incoming signal at low energies and the same minimum tank number cut would not exclude as many low-signal events as beforehand, thus decreasing the reconstruction performance. Similarly to the reconstruction of the A configurations, the data cut has not been optimised for the different configurations, which would be necessary for a final assessment.

The effect of the cut is mainly visible at low energies and vanishes for the high-end of the energy distribution. The same can be seen for the core performance of E1, which is comparable to the core reconstruction of the remaining setups at high energies and only worsens below approximately 1 TeV.

When looking at outer array EAS, it is visible that all configurations apart from A1 and the reference configuration reach core resolution values well above 25 m below 100 GeV, which could again be explained by the fact that the applied data cut was optimised for the A tank design. E1 still seems to exceed the core resolution values of all remaing configuration, suggesting that it has the lowest trigger treshold to γ-ray induced EAS. On the other hand, the decreased trigger treshold of the B1 configuration could then be explained by the larger 10"HQE photomultiplier that is placed within it, which in turn can detect more signal, while C1 possesses a larger number of tank units than A1 which consequently implies that a larger number of PMTs can potentially detect secondary shower particles, making the tank condition less restrictive and thus excluding less low-signal events.

The D1 and F1 configurations have the largest tank units, but in turn possess the least amount of detection tanks. Thus, one would expect the tank condition to be more restrictive than for the A1 configuration and thus D1 and F1 to perform better at low energies, as more low-signal events are excluded. This expectation is confirmed when looking into inner array showers. However, for outer array showers the core resolution suddenly increases for decreasing energies below approximately 150 GeV. This feature cannot be explained at this stage and needs to be investigated further in the future.

When assessing inner and outer array showers together, as seen in Figure 6.6, most of the previously mentioned features still appear. However, the anomalies for the core resolution of D1 and F1 at low energies do not persist, which suggests that most low-energy events that trigger the tank condition are located within the inner array. Furthermore, one can see that the reference configuration performs worse at high energies, which could be explained by the fact that an inferior 8" PMT is used, as well as decreased statistics. When assessing the high-end of the energy distribution above 30 TeV, one notices that all remaining configurations perform almost equally well and that all differences in performance can be attributed to statistical fluctuations. This suggests that differences in tank design have a smaller impact on the configuration's performance at high energies

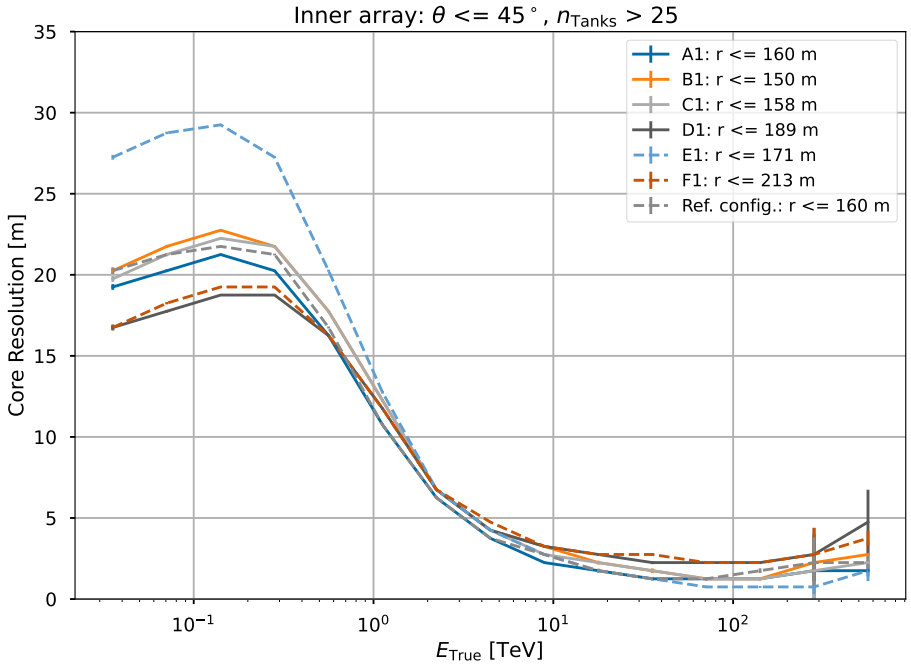

(a)

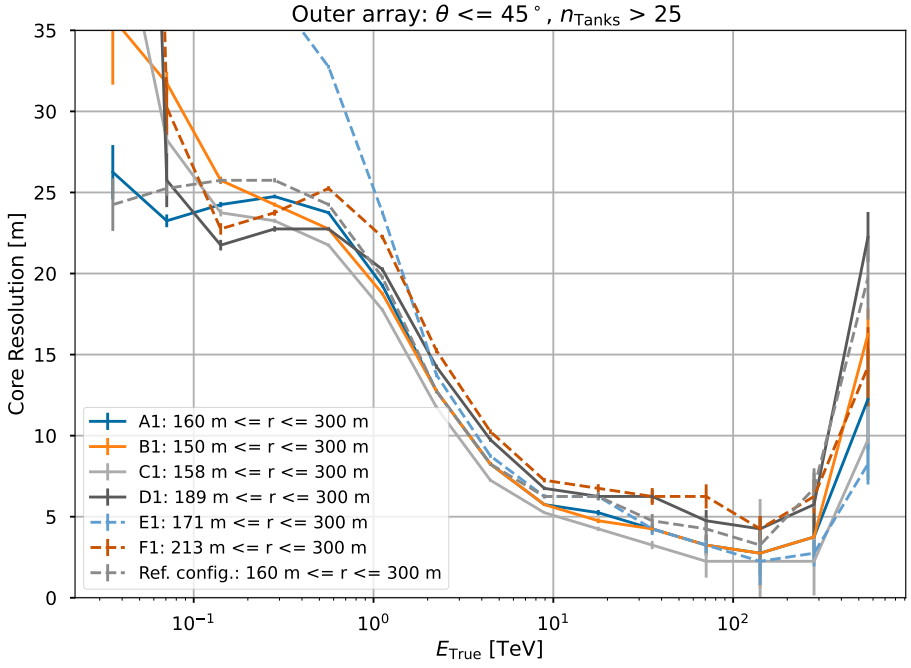

(b)

Figure 6.5: Core resolution, defined as the 68 % containment radius of the distribution of distances between real and reconstructed EAS core, plotted for the 1 configurations. Showers that fell on the inner array (a) and outer array (b) are shown separately.

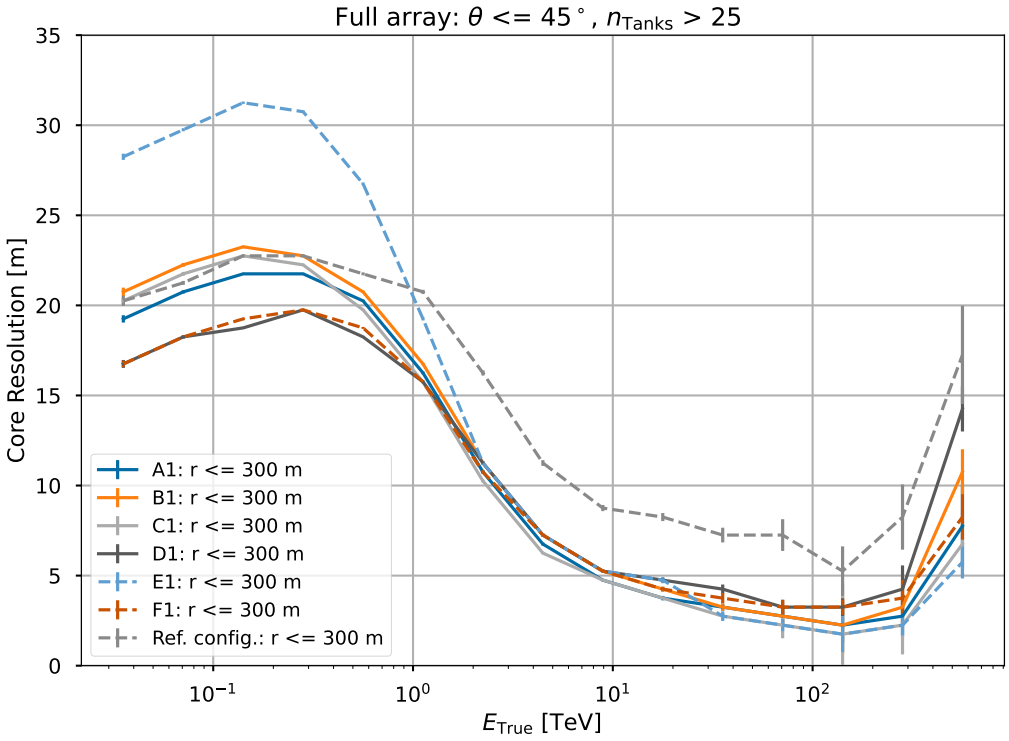

Figure 6.6: Core resolution, defined as the 68 % containment radius of the distribution of distances between real and reconstructed EAS core, plotted for the 1 configurations. All showers that fell onto the array have been taken into consideration.

than the previously analysed differences in array layout. This can be explained by the fact that differences in array layout oftentimes include differing array sizes, which in turns impacts the array's ability to detect the extremitites of high-energy EAS. On the other hand, differences in tank design lead to larger differences at lower energies, as the trigger treshold of the setup varies when different PMT and tank unit sizes are used and the number of tank units also fluctuates.

6.3 Energy Reconstruction

Next, the accuracy of the energy reconstruction shall be evaluated. In order to do so, the relation $\log_{10}(E_{\text{Reco}}/E_{\text{True}})$ between reconstructed and true energy is plotted over the true EAS energy, as shown in Figure 6.7 for A1. Higher absolute values of $\log_{10}(E_{\text{Reco}}/E_{\text{True}})$ thereby indicate a higher difference between the reconstructed and true energy values and thus a less accurate reconstruction.

The measures by which the energy estimation can be evaluated are the energy resolution and the energy bias. The energy resolution is defined as the root mean squared (RMS) of the $\log_{10}(E_{\text{Reco}}/E_{\text{True}})$ distribution within each true energy bin, while the energy bias is simply computed as the mean of the same distribution.

The mean error can then be computed to be

$$\frac{\Delta \log_{10,\ \text{mean}}(E_{\text{Reco}}/E_{\text{True}})}{\sqrt{n_{\text{events}}}} \tag{6.2}$$

for a number of n_{events} events in each energy bin and utilised for the energy bias, while the error of the energy resolution can be expressed by

$$\frac{\Delta \log_{10,\ \text{RMS}}(E_{\text{Reco}}/E_{\text{True}})}{\sqrt{2(n_{\text{events}}-1)}} \tag{6.3}$$

,

similarly to the error that has been computed for the core resolution in section 6.2.

In the following, the energy resolutions and biases are assessed for the A and 1 configurations. Similarly to the core analysis, showers whose core position falls on the inner and outer array are investigated separately, before analysing them in conjunction. Thereby, it shall be assessed whether the performance-related features of the M5 configurations that have been found throughout the analysis of the core reconstruction in section 6.2 can be related to similar features throughout the energy evaluation.

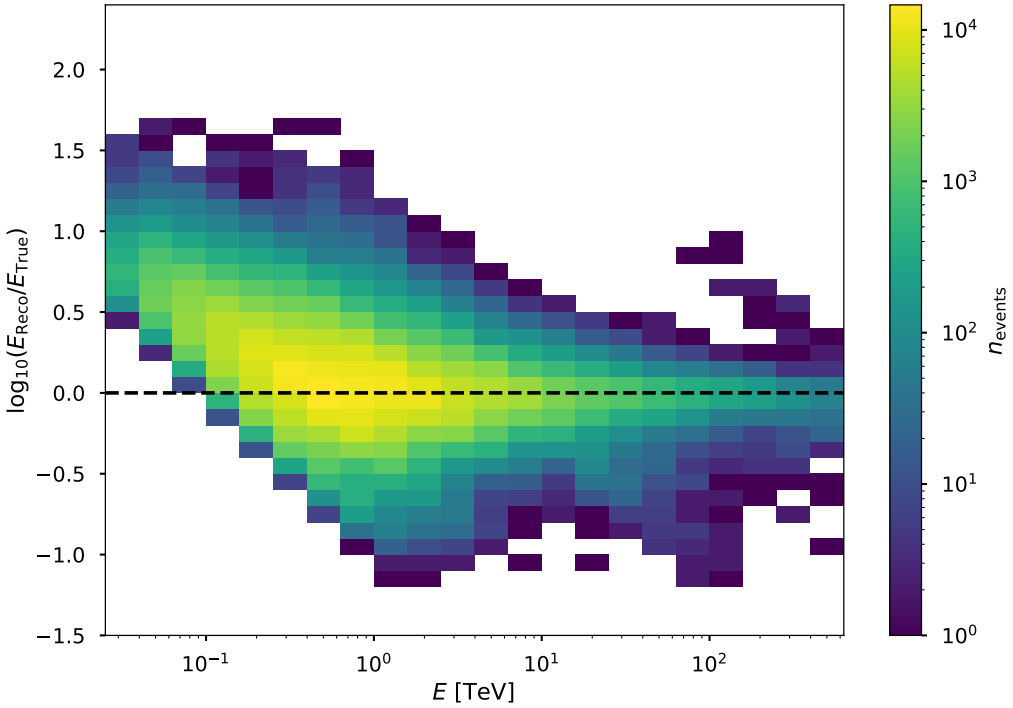

Figure 6.7: Histogram with which the energy resolution and the energy bias of the A1 configuration can be computed. The relation $\log_{10}(E_{\mathrm{Reco}}/E_{\mathrm{True}})$ is plotted over the true EAS energy, the colorbar represents the number of events. Only showers whose core position lies within the array have been taken into consideration

6.3.1 A Configurations

In Figure 6.8, the energy resolution of the A configurations can be seen for showers with inner and outer array core positions. EAS with a core that lands within the confinements of the inner array behave almost indistinguishably from one another, similarly to the core assessment. Again, differences between the layouts seem to minimise with increasing energies up until approximately 100 TeV, before increasing again due to statistical fluctuations. At lower energies below 10 TeV the A5 configuration seems to perform best, which would confirm the assumption that the decrease in inner array tank density from 80 % to 40 % can be compensated by an overall larger inner array radius and even lead to a superior setup at the low-end of the energy distribution.

Similarly to the core analysis, differences between the layouts increase when looking at EAS with outer array cores, shown in Figure 6.8, as the amount of signal is decreased. Furthermore, the drop in performance for A6 and A7 also persists throughout the energy estimation, which then also negatively affects the performance of the entire array, shown in Figure 6.9. The comparison between A2, A3 and A4 for outer array showers shows again that A4 performs best at lower energies below 400 GeV, while A2 reconsts the energy of the EAS more accurately above approximately 80 TeV. At the same time, the clustering of outer array tanks in A3 leads to decreased outer array performance at high energies above 20 TeV, in comparison to A2. At and above energies of approximately 200 TeV, one can recognise an increase in energy resolution for all configurations, similarly to the increase in core resolutions, which has been discussed in section 6.2. One can still speculate this increase to partially happen due to statistical reasons, as less showers have been simulated in that energy range. Also, high-energy showers might exceed the boundaries of the detection due to their increased area, which might imply an additional dip in performance after 200 TeV.

When investigating all showers that fall onto the array, as shown in Figure 6.9, one still finds A2 and A5 to perform best for higher energies above 80 TeV, while the latter also shows the best energy performance at lower energies below approximately 700 GeV, followed by A4. However, between approximately 1 TeV and 70 TeV, A5 performs worse than A2, A3 and A4, while still outperforming A1, A6 and A7. Thereby, the increase in resolution that is visible between approximately 10 TeV and 70 TeV would to be investigated in the future, as it connot be explained at this stage.

Assuming that the SWGO detection site is set to focus on the investigation of γ-ray induced EAS in the TeV range, one could suggest that A2 might be even more suitable than A5 with regard to its energy performance. However, one would need to investigate this feature, while conducting a performance analysis with optimised cuts for each configuration, before drawing finalised conclusions on this matter.

The energy resolution can also be expressed percentage-wise by calculating

$$\left|\left(E_{\text{Reco}} - E_{\text{True}}\right)\right| / E_{\text{True}} \tag{6.4}$$

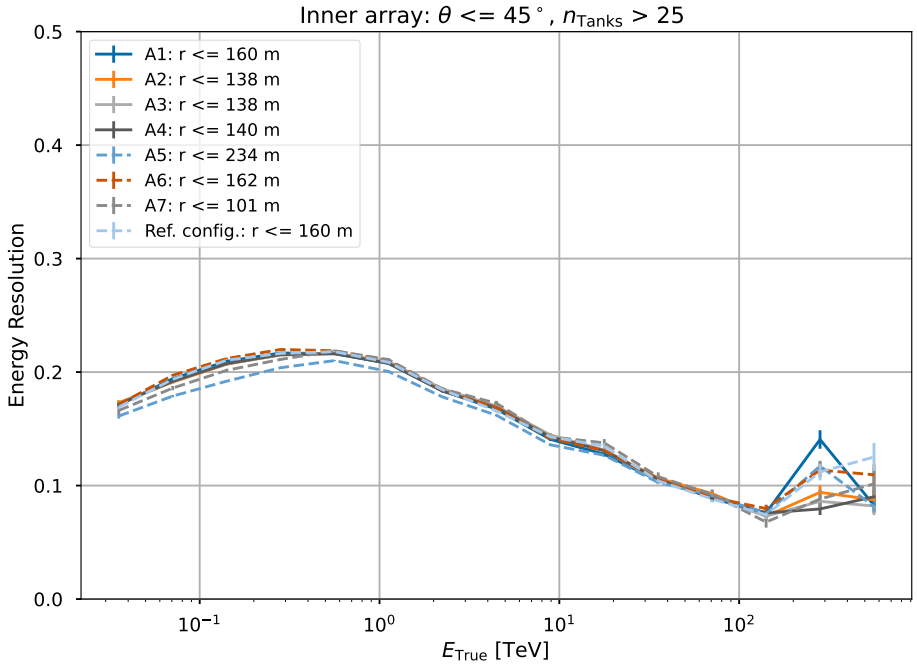

(a)

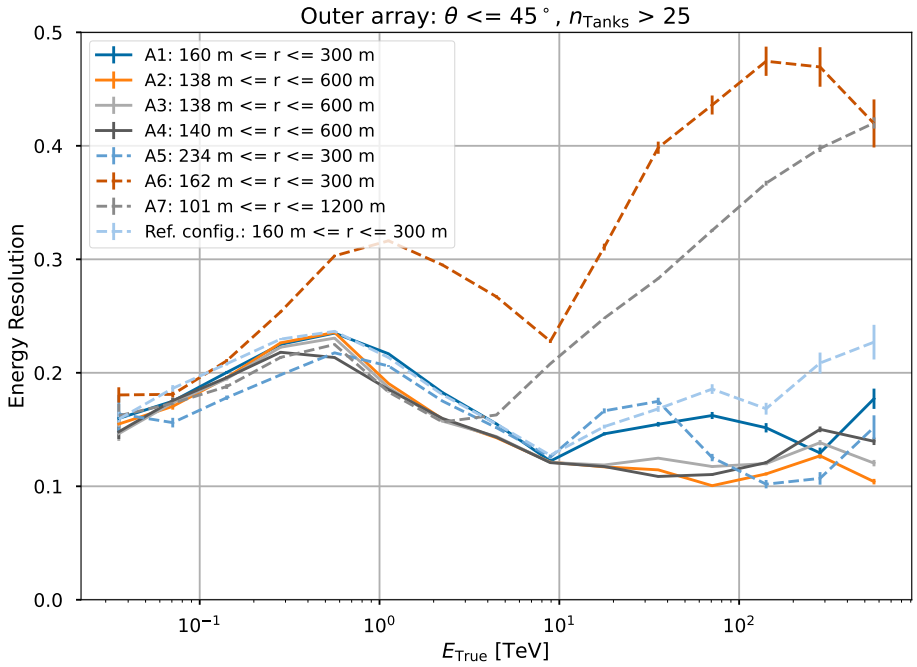

(b)

Figure 6.8: Energy resolution, defined as the RMS of the distribution of $\log_{10}(E_{\mathrm{Reco}}/E_{\mathrm{True}})$, plotted for the A configurations. Showers that fell on the inner array (a) and outer array (b) are shown separately.

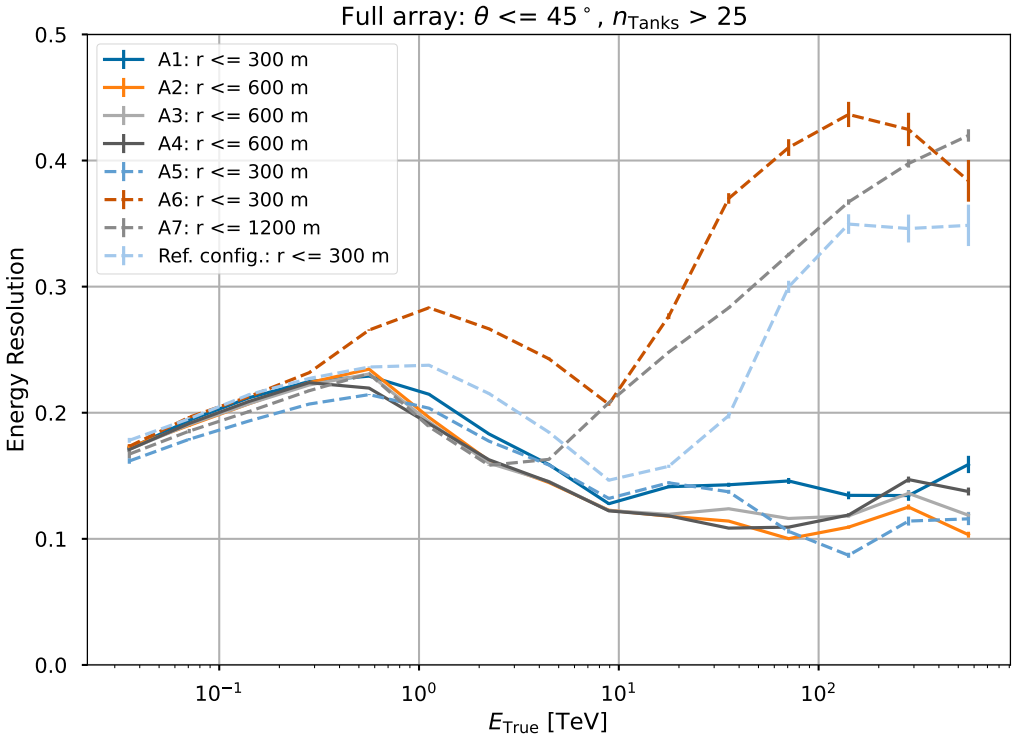

Figure 6.9: Energy resolution, defined as the RMS of the distribution of $\log_{10}(E_{\mathrm{Reco}}/E_{\mathrm{True}})$, plotted for the A configurations. All showers the fall onto the array have been taken into consideration.

Thereby, when investigating all showers that fall onto the array from Figure 6.9, it can be shown that the A2 energy resolution decreases from $\sim 66\%$ at around 1 TeV to $\sim 27\%$ at approximately 100 TeV, when investigating the energy resolution curve of all showers combined.

Besides assessing the energy resolution, one can also investigate the energy bias. As previously mentioned, it showcasts the mean of the distribution of $\log_{10}(E_{\text{Reco}}/E_{\text{True}})$, that has been shown in Figure 6.7. Thereby, energy bias values around 0 would be most optimal, as this would imply that the true and reconstructed energies are almost identical on average. As can be seen in Figure 6.10, the energy bias is very similar for all A configurations when only investigating showers whose core falls onto the inner array of the setup. At lower energies, the energy bias is increased due to limited shower signal and starts fluctuating around 0 at and above energies of about 0.7 TeV. For energies above approximately 200 TeV, a slight dip in energy bias can be seen which could be explained by limits in the setup, as the showers might exceed the size of the inner array. Thus, the part of the shower that is absorbed within the outer array generates less signal, which consequently amounts to a decreased reconstructed energy in comparison to the true EAS energy. Also, statistical fluctuations need to be taken into consideration, as less showers have been simulated for energies above 200 TeV.

The energy bias of outer array showers, visible in Figure 6.10, confirms the assessment that the general performance of the A6 and A7 configurations is negatively impacted by the low fill factor of their respective outer arrays. However, the remaining configurations are very similar to one another and do not show any significant bias between approximately 3 TeV and 300 TeV. This indicates a stable region for energy reconstructions in that given energy range [Jos19], which substantiates the previously drawn conclusions from the discussion of the energy resolutions for higher energies. Consequently, the increased low-energy performance of A5 in comparison to A2 can be put in perspective and be seen as less important, while the superior A2 energy performance for energies above 10 TeV could be regarded as more relevant. Similar conclusions can also be drawn from the energy bias of all showers whose core falls onto the array, which are visualised in Figure 6.11.

6.3.2 1 Configurations

In this section, the energy performance of the 1 configurations shall be assessed. For inner array showers the energy resolutions behave almost identically for all setups, as shown in Figure 6.12, while E1 performs slightly worse at lower energies. This feature was also visible throughout its core assessment and could again be motivated by the suggestion that the tank condition excludes less low-signal events for E1, due to its decreased trigger treshold. When assessing outer array showers, one can observe that D1 and F1 perform better at low energies which could be explained by the data cut, as elaborated on in section 6.2, while the energy resolution curve of B1 and C1 could be slightly higher than A1 as a result of the same reason. D1 and F1 feature a smaller number of tanks and

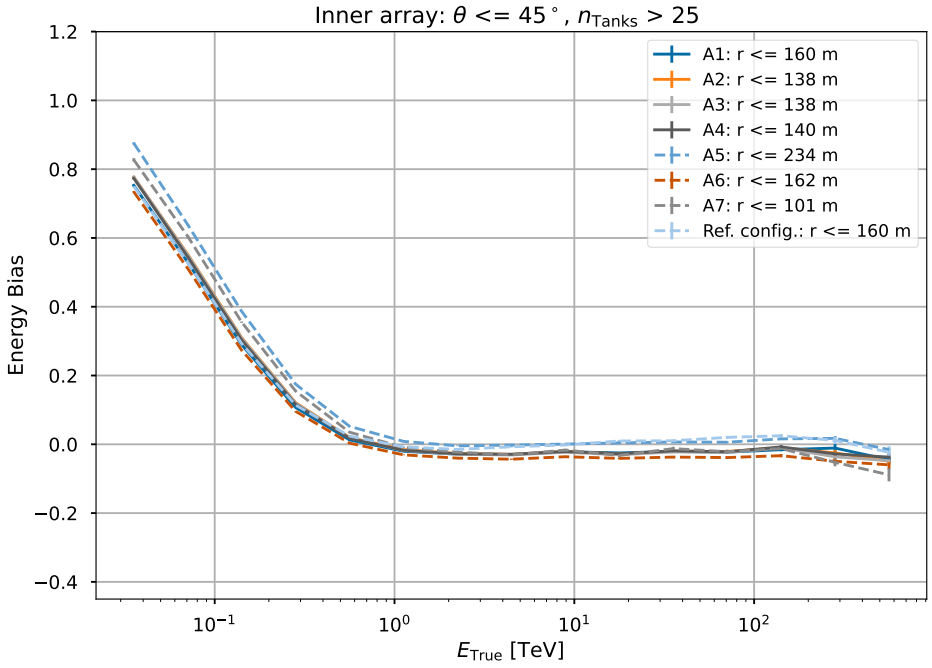

(a)

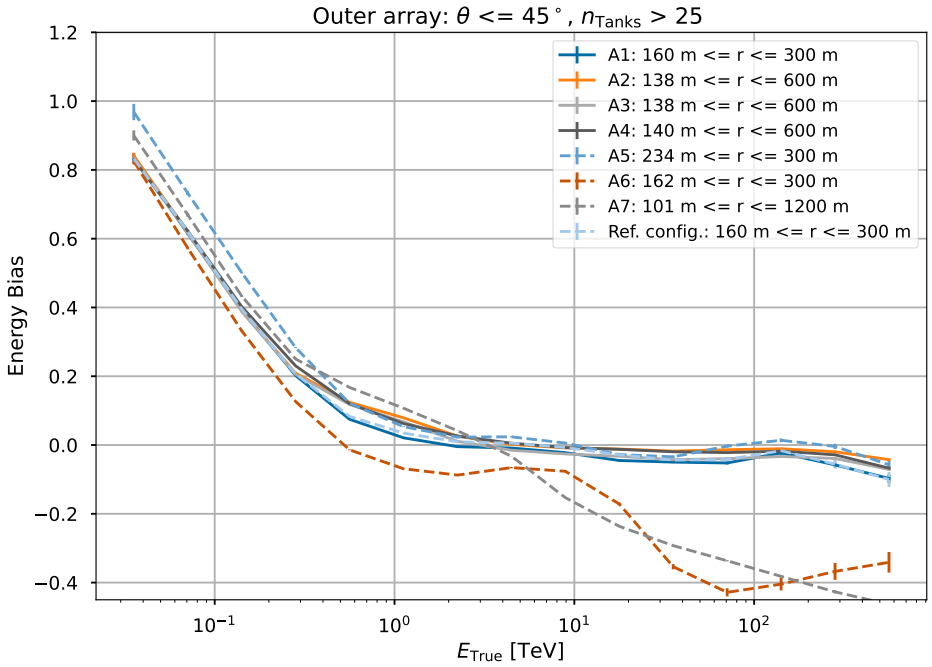

(b)

Figure 6.10: Energy bias, defined as the mean of the distribution of $\log_{10}(E_{\mathrm{Reco}}/E_{\mathrm{True}})$, plotted for the A configurations. Showers that fell on the inner array (a) and outer array (b) are shown separately.

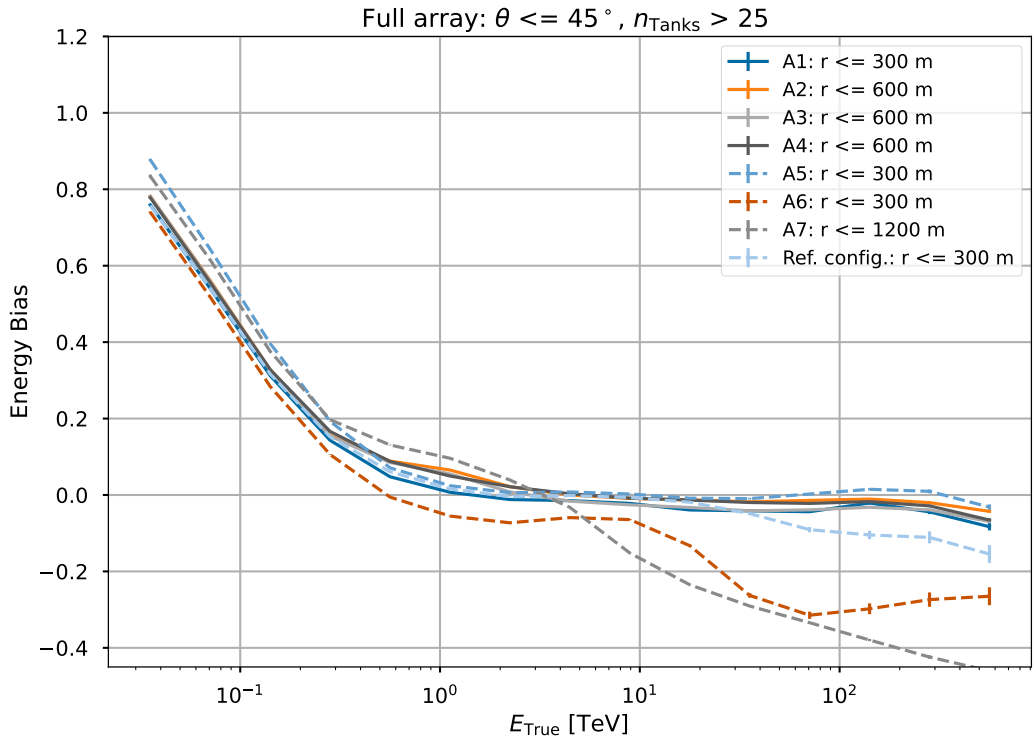

Figure 6.11: Energy bias, defined as the mean of the distribution of $\log_{10}(E_{\text{Reco}}/E_{\text{True}})$, plotted for the A configurations. All showers the fall onto the array have been taken into consideration.

consequently the tank condition would be triggered for a smaller number of low-energy showers, while C1 features the most water tanks out of all 1 configurations. On the other hand, B1 uses larger PMTs than A1, which should imply that the trigger treshold is decreased.

When investigating all showers in conjunction, visible in Figure 6.13, the same features largely persist. At the higher end of the energy distribution above 10 TeV, all 1 configurations seem to perform similarly well with the exception of the resolution increase after 20 TeV for D1 and F1. This feature cannot be explained at this stage and needs to be investigated in the future.

Next, the energy bias can be visualised for inner and outer array showers, as seen in Figure 6.14 and all those events combined, as shown by Figure 6.15. Similarly to the assessment of the A configurations, one can see that a stable energy reconstruction energy range can be set between approximately 2 TeV and 100 TeV, in which no significant bias can be observed. An exception to this assessment can be found in the biases of D1 and F1 for outer and full array showers above approximately 20 TeV. This feature seems to be linked to the increase in energy resolution above 20 TeV for both configurations and should therefore be investigated further.

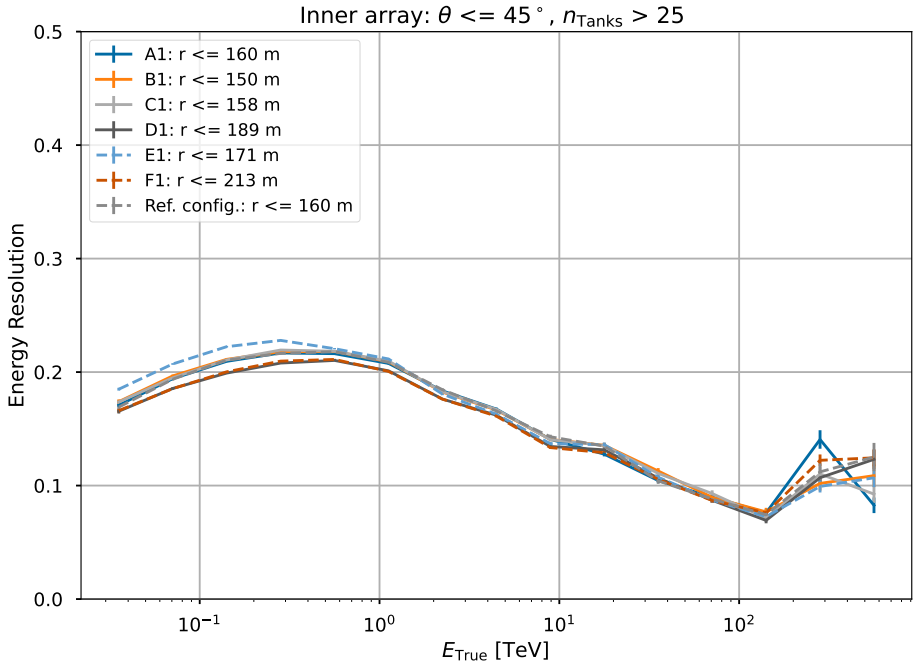

(a)

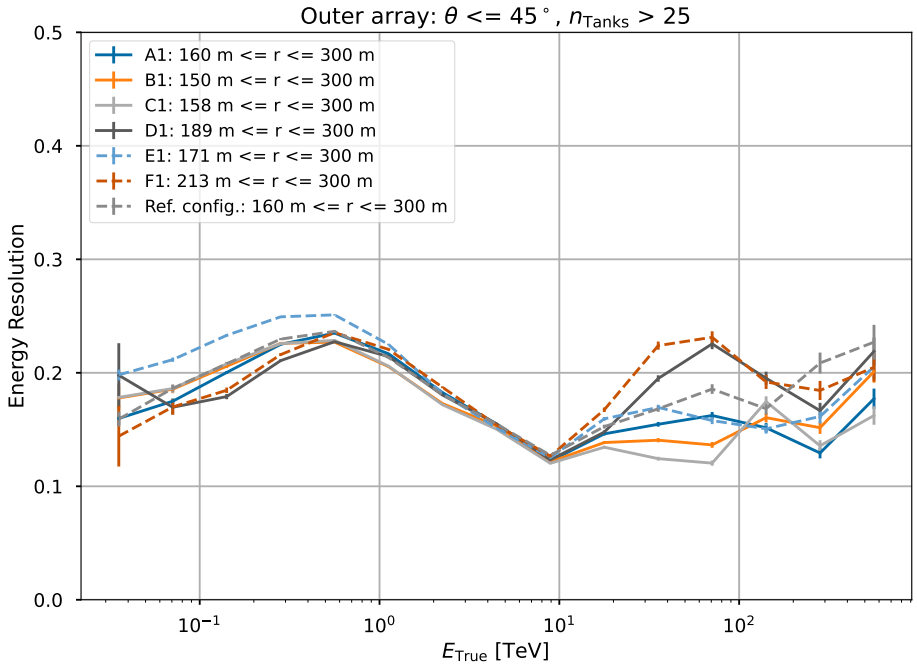

(b)

Figure 6.12: Energy resolution, defined as the RMS of the distribution of $\log_{10}(E_{\text{Reco}}/E_{\text{True}})$, plotted for the 1 configurations. Showers that fell on the inner array (a) and outer array (b) are shown separately.

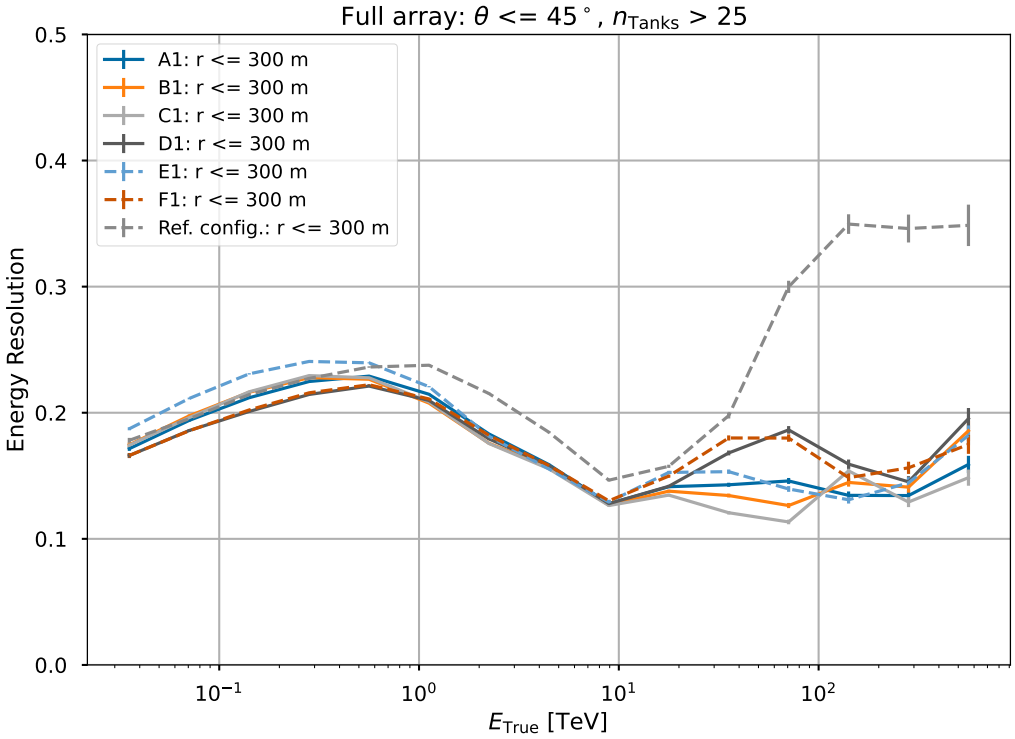

Figure 6.13: Energy resolution, defined as the RMS of the distribution of $\log_{10}(E_{\text{Reco}}/E_{\text{True}})$, plotted for the 1 configurations. All showers the fall onto the array have been taken into consideration.

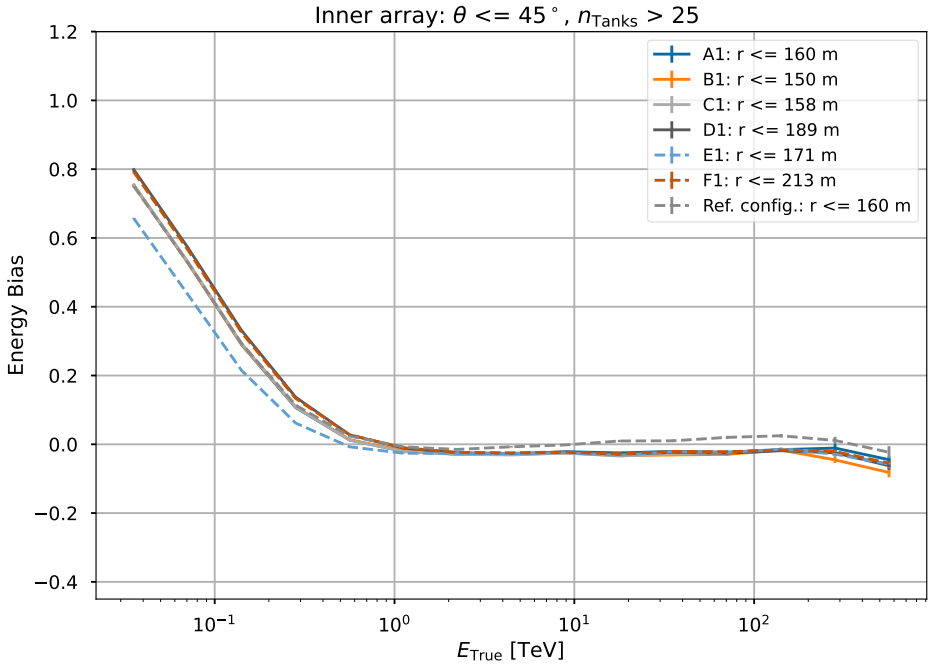

(a)

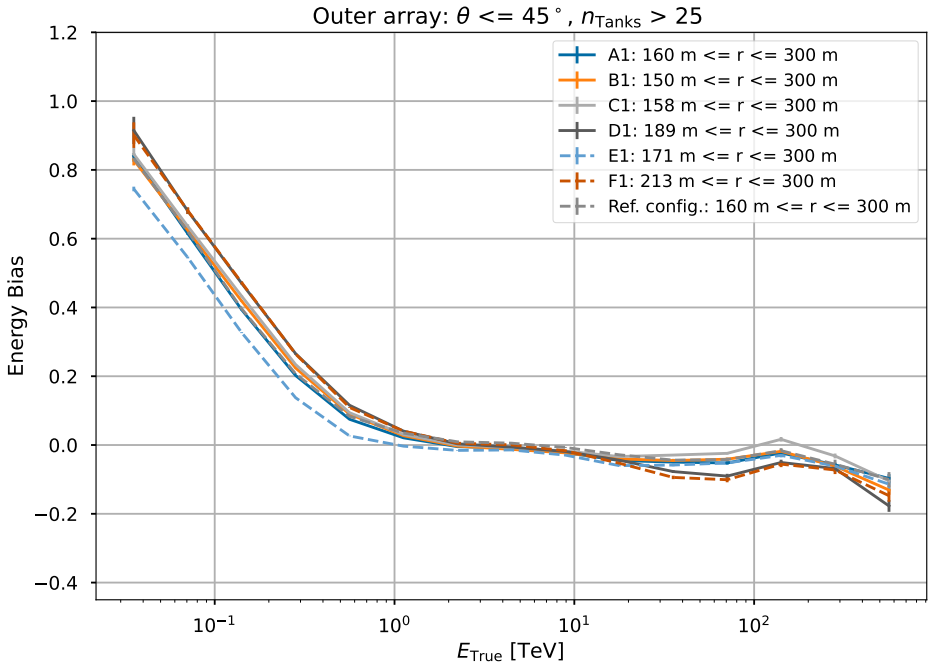

(b)

Figure 6.14: Energy bias, defined as the mean of the distribution of $\log_{10}(E_{\text{Reco}}/E_{\text{True}})$, plotted for the 1 configurations. Showers that fell on the inner array (a) and outer array (b) are shown separately.

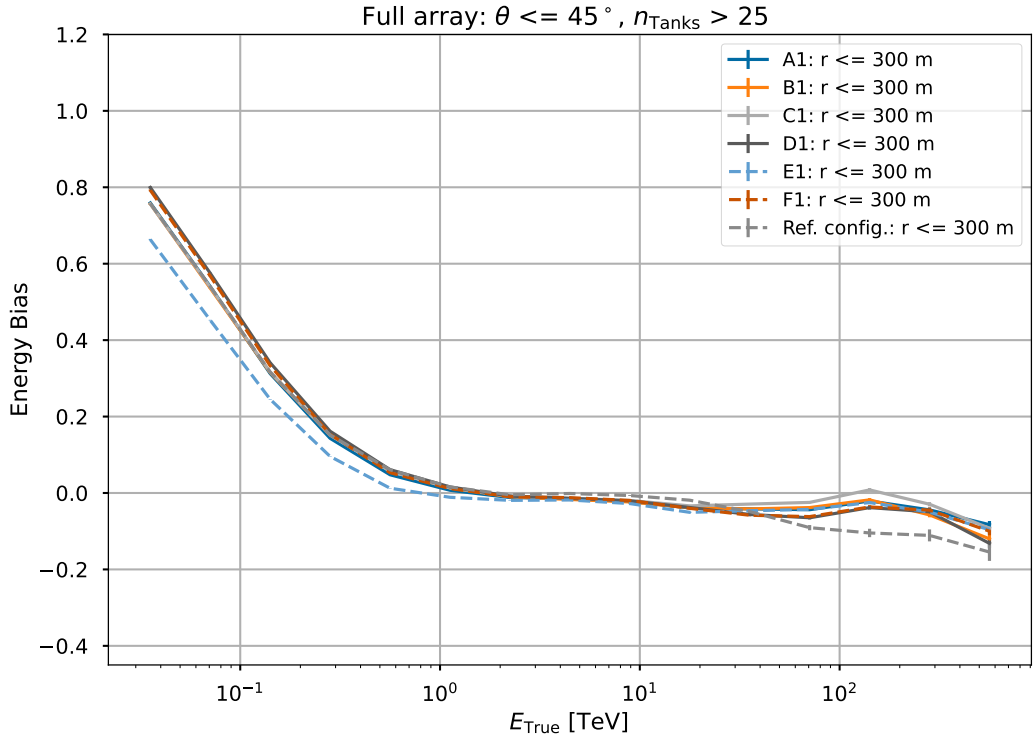

Figure 6.15: Energy bias, defined as the mean of the distribution of $\log_{10}(E_{\text{Reco}}/E_{\text{True}})$, plotted for the 1 configurations. All showers that fell onto the array have been taken into consideration.

6.4 Direction Reconstruction

Finally, the direction reconstruction of the M5 configurations is assessed. Similarly to the core and energy evaluation, one first generates a histogram in which the angular difference between true and reconstructed direction is plotted over the true shower energy, as seen in Figure 6.16 for the A1 configuration.

Subsequently the angular resolution and bias are computed, in order to analyse the precision of the direction reconstruction. Similarly to the core resolution, the angular resolution is defined as the 68 % containment radius of the distribution of angles between the simulated and reconstructed shower direction for each energy bin. The angular bias is simply calculated as the mean of the same distribution.

Similarly to the energy evaluation, one can express the errors of the angle resolution by

$$\frac{\Delta \text{ angle }_{68\%}}{\sqrt{2(n_{\text{events}} - 1)}} \tag{6.5}$$

while the error of the angular bias can be calculated with the following expression:

$$\frac{\Delta \text{ angle }_{\text{mean}}}{\sqrt{n_{\text{events}}}} \tag{6.6}$$

.

The angular resolution and bias have been plotted for the reconstructed angle values after the second plane fit, which is conducted separately after the likelihood fit. Thereby, the fitted values from the likelihood minimisation can be used as seed values throughout this second plane fit, leading to an improved direction reconstruction in comparison to the first plane fit, for which the centre of mass core position has been used as a seed. Therefore, one expects similar features from section 6.2 to be noticeable throughout the investigation of the angular performance, as the core and direction reconstructions are linked, as elaborated on in section 4.3.

6.4.1 A Configurations

When assessing the inner array showers from Figure 6.17, one can observe that the angular resolution ranges only up to approximately 1°. Similarly to the inner array resolution plots for the core and energy reconstructions, one can furthermore see that the resolution decreases for rising true energy values and that all configurations behave similarly. After about 100 TeV, an increase in angular resolution can be seen which again come from the limited area of the detection sites, as the overall area of the shower might exceed those limitations, as well as due to statistics.

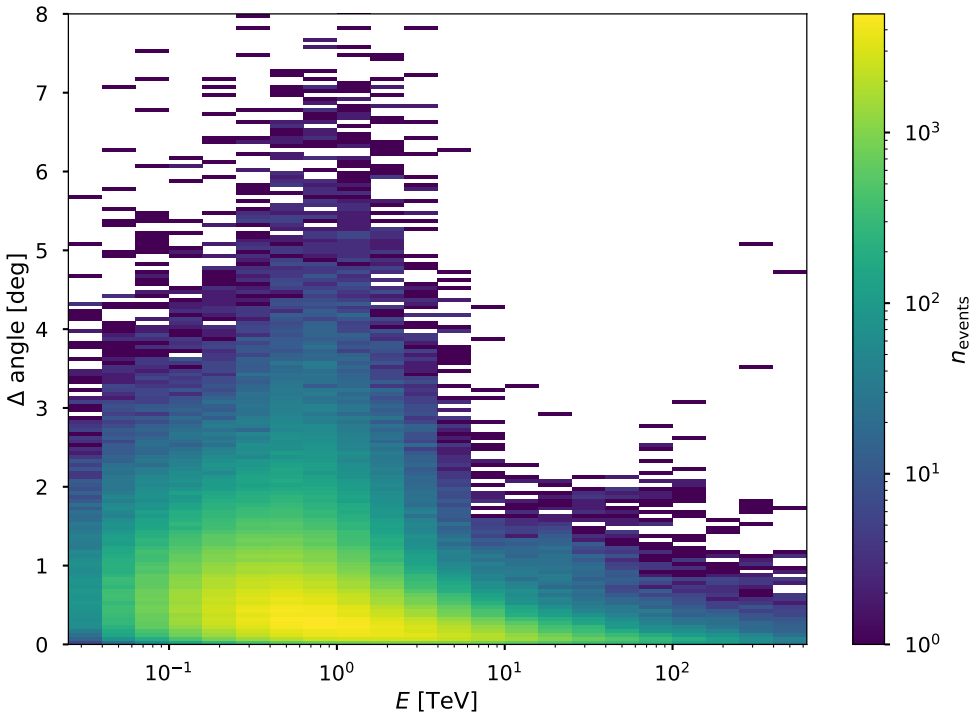

Figure 6.16: Histogram with which the angular resolution of the A1 configuration can be computed. The difference between the reconstructed and true zenith angle is plotted over $\log_{10}(E_{\mathrm{True}}/\mathrm{GeV})$, while the number of events is showcasted by the colorbar. Only showers whose core position lies within the array have been taken into consideration

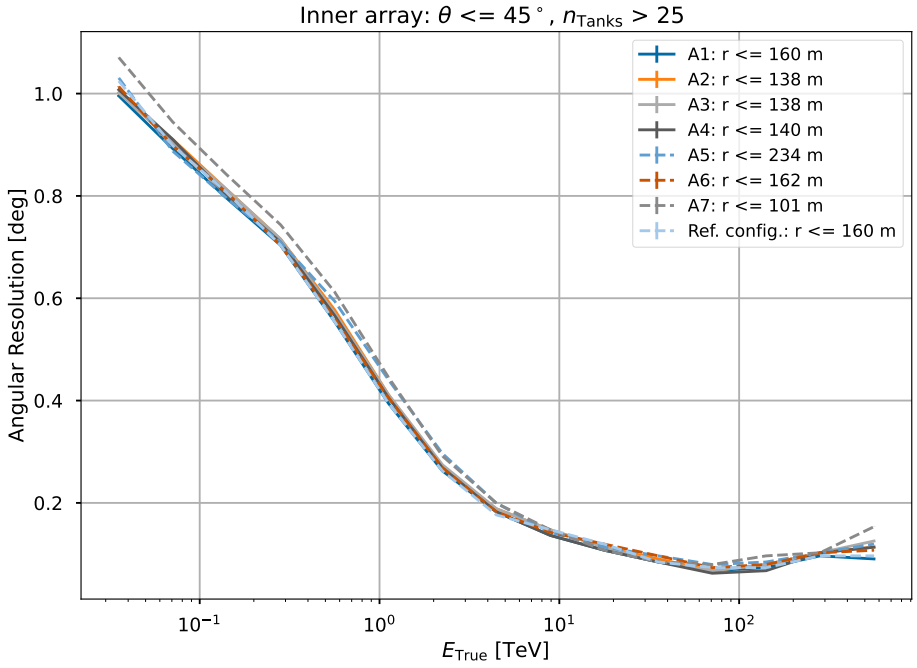

(a)

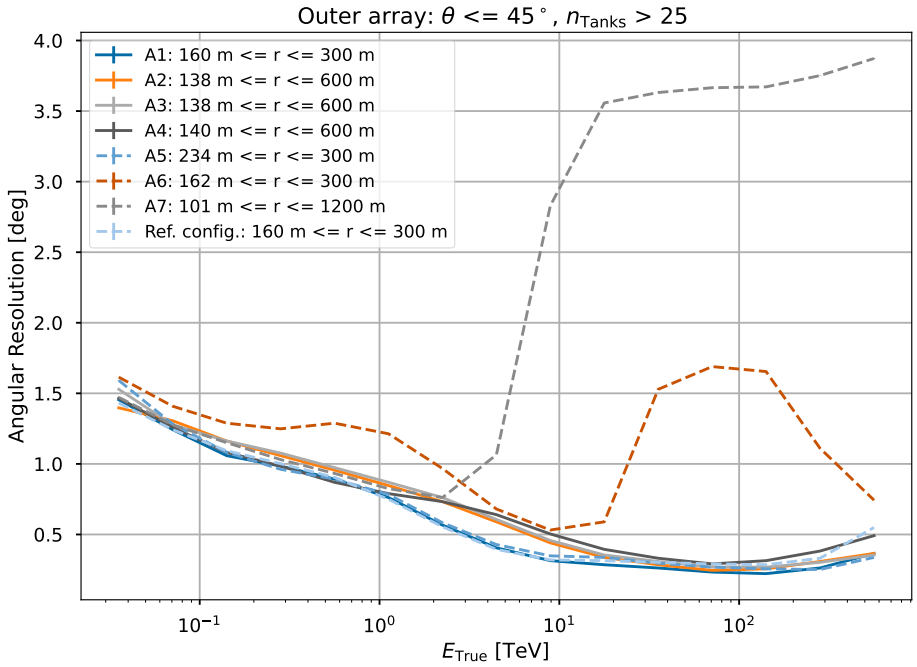

(b)

Figure 6.17: Angular resolution, defined as the 68 % containment radius of the distribution of angles between reconstructed and true EAS direction, plotted for the A configurations. Showers that fell on the inner array (a) and outer array (b) are shown separately.

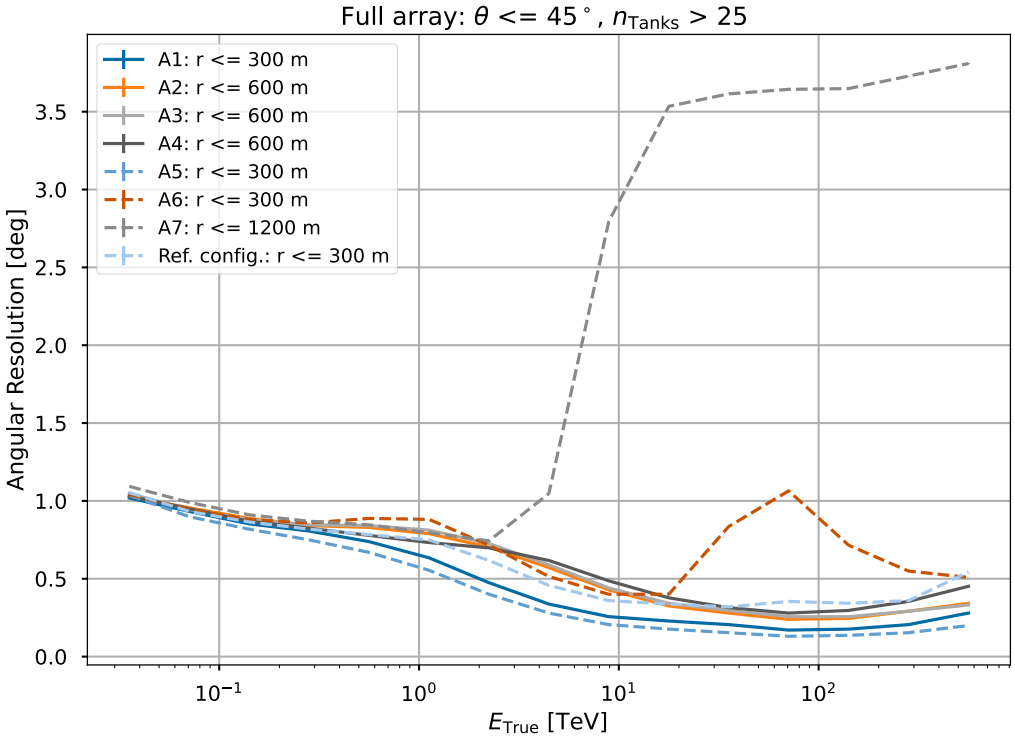

Figure 6.18: Angular resolution, defined as the 68 % containment radius of the distribution of angles between reconstructed and true EAS direction, plotted for the A configurations. All showers that fell onto the array have been taken into consideration

When looking into the angular resolution of outer array showers from Figure 6.17, the previously seen anomalies for A6 and A7 can be recognised and explained by the inferior core performance of these array. Thus, an inaccurate core position is used as seed throughout the plane fit, which leads to decreased angular performance. The best performance at high energies above approximately 20 TeV can be observed for A1, A2 and A5, which apart from A1 is in line with the features observed in the core resolution curve from section 6.2. Furthermore, A2 continues to perform better than the similar A3 configuration and has a lower angular resolution than A4 at high energies above approximately 3 TeV, while the latter is superior at the lower end of the energy distribution below 3 TeV.

The same features persist when inner and outer array showers are analysed in conjunction, as seen in Figure 6.18. This confirms the previously assumed link between core and angular reconstruction and thereby indicates that the angle fitter operates in accordance with prior expectations. This can be seen as an important step towards real-life shower reconstruction, as all relevant shower properties can now be reconstructed and utilised throughout the assessment of possible configurations.

Finally, it is possible to investigate the angular bias of the A configurations, in order to assess whether a stable energy range for angular reconstructions can be set. In Figure 6.19, the bias has been plotted for showers whose core falls onto the inner and outer array, while Figure 6.20 visualises the angular bias of all these showers together. With the noticeable exception of the A7 bias curve for outer and full array showers, which can be motivated by low fill factor and large radius of its respective outer array, the bias values find themselves at and below approximately 0.02°.

6.4.2 1 Configurations

Finally, the angular performance of the 1 configurations can be investigated. Similarly to the angular resolution curves of the A configuration, the angle performance improves for increasing energies, due to increased signal. For both inner and outer array showers, plotted in Figure 6.21, E1 performs worse than the remaing configurations at low energies below 100 GeV, that can probably be explained by the minimum tank condition, which has been explained in more detail in section 6.2. While E1 and F1 seem to perform slightly worse than the remaining 1 configurations, maximum angular resolution values do not surpass 2.5°. For outer array showers, C1 shows the lowest angular resolution for energies above 10 TeV, which could again be explained by its increased number of tank units. When assessing the angle bias of the 1 configurations, shown in Figure 6.23 and Figure 6.24, one can still observe that E1 and F1 perform worse than the remaing 1 configurations, while their direction bias values do not exceed 0.04°.

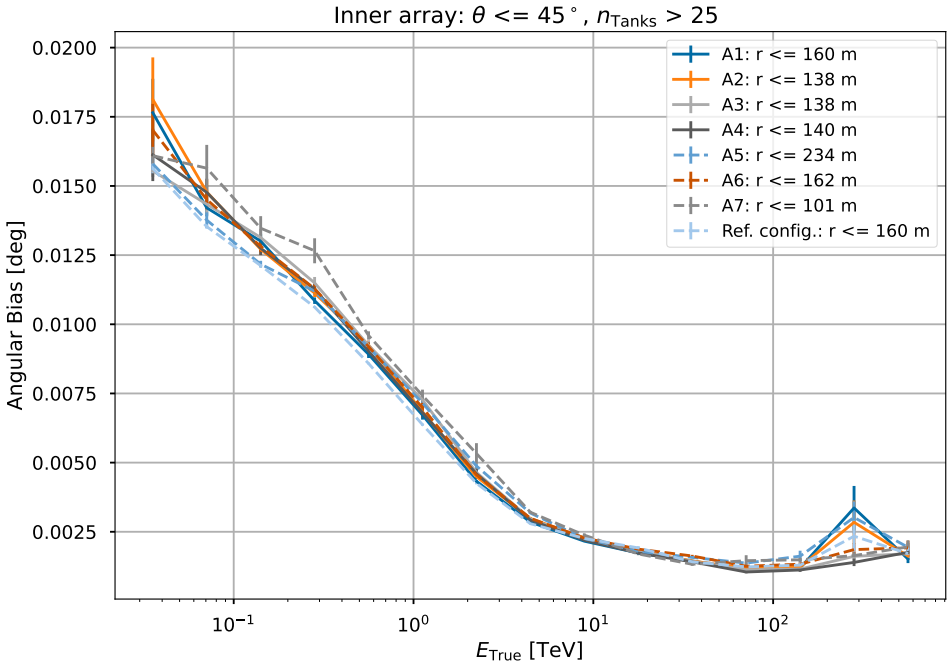

(a)

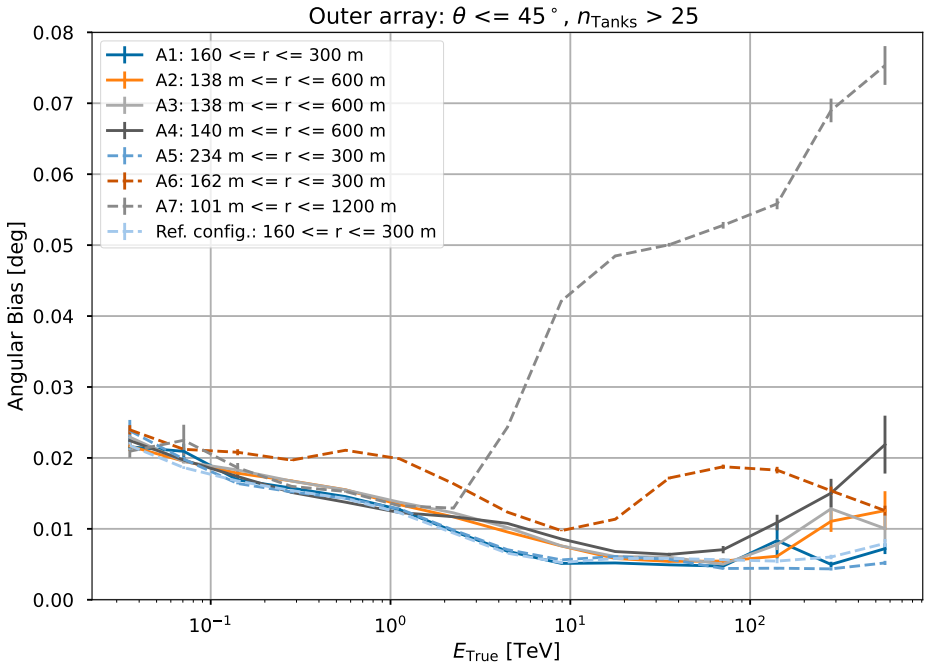

(b)

Figure 6.19: Angular bias, defined as the mean of the distribution of angles between reconstructed and true EAS direction, plotted for the A configurations. Showers that fell on the inner array (a) and outer array (b) are shown separately.

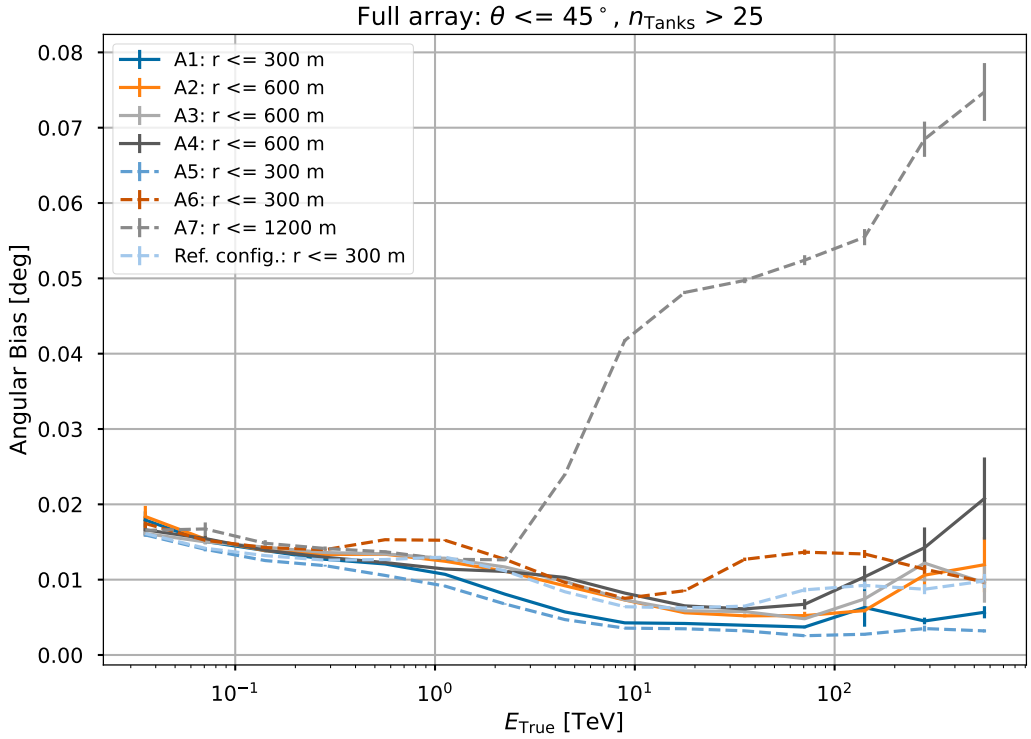

Figure 6.20: Angular bias, defined as the mean of the distribution of angles between reconstructed and true EAS direction, plotted for the A configurations. All showers that fell onto the array have been taken into consideration.

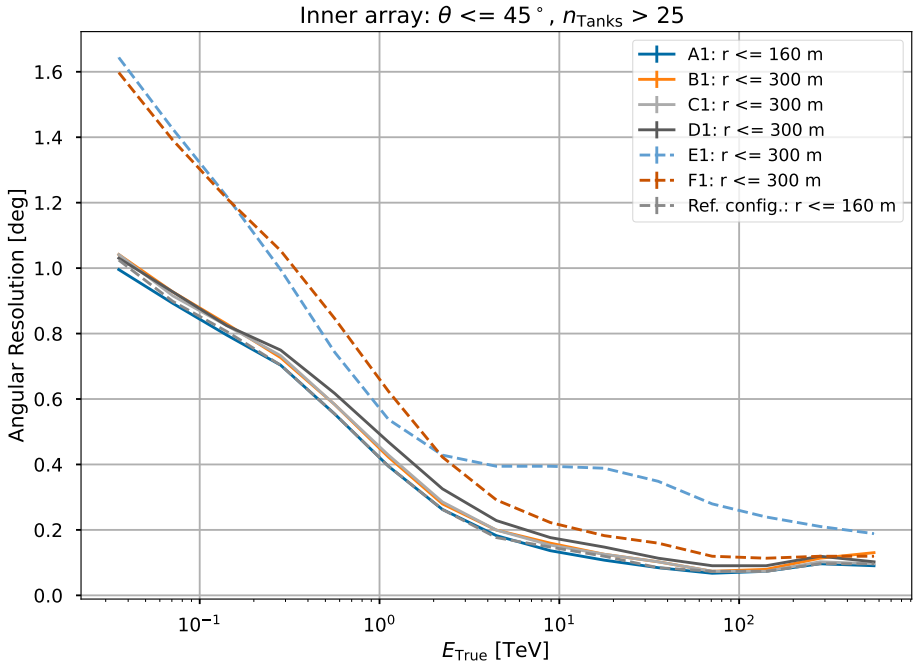

(a)

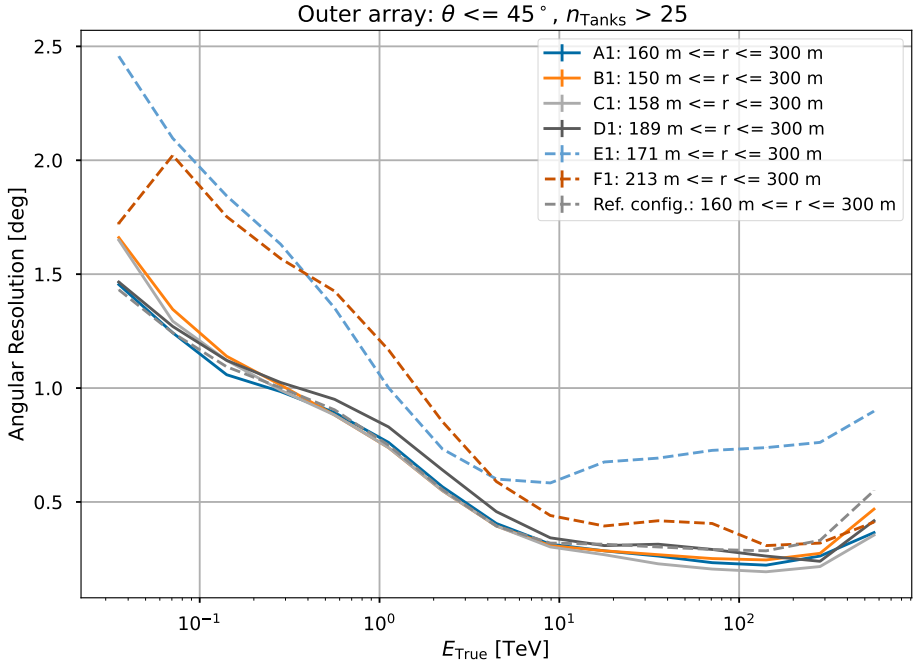

(b)

Figure 6.21: Angular resolution, defined as the 68 % containment radius of the distribution of angles between reconstructed and true EAS direction, plotted for the 1 configurations. Showers that fell on the inner array (a) and outer array (b) are shown separately.

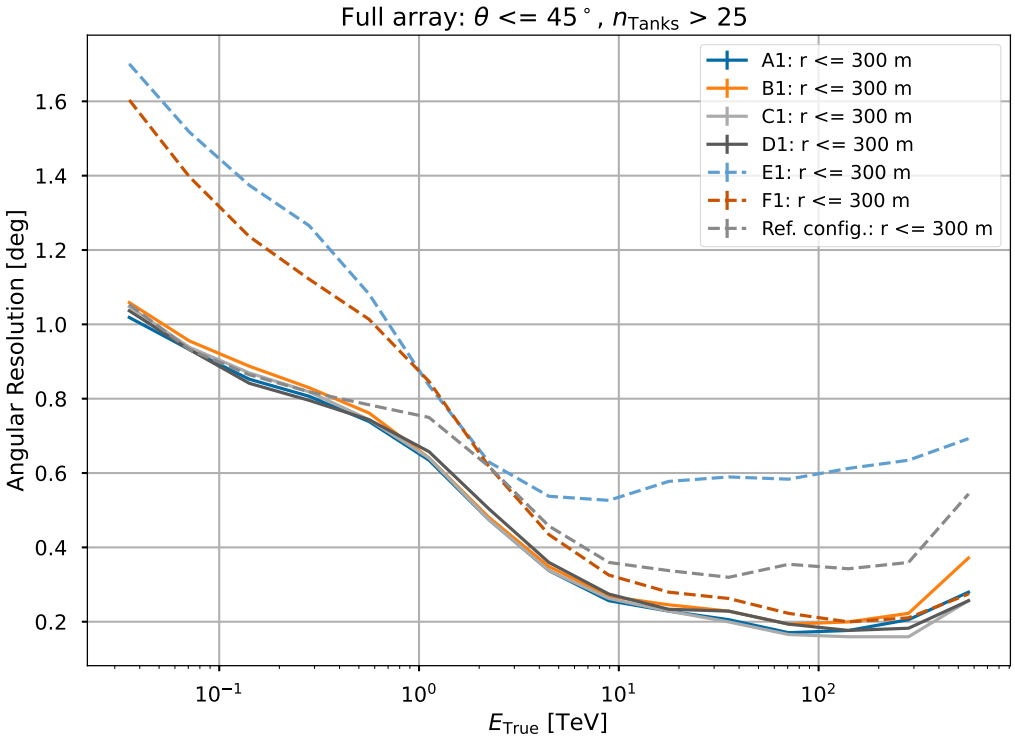

Figure 6.22: Angular resolution, defined as the 68 % containment radius of the distribution of angles between reconstructed and true EAS direction, plotted for the 1 configurations. All showers that fell onto the array have been taken into consideration

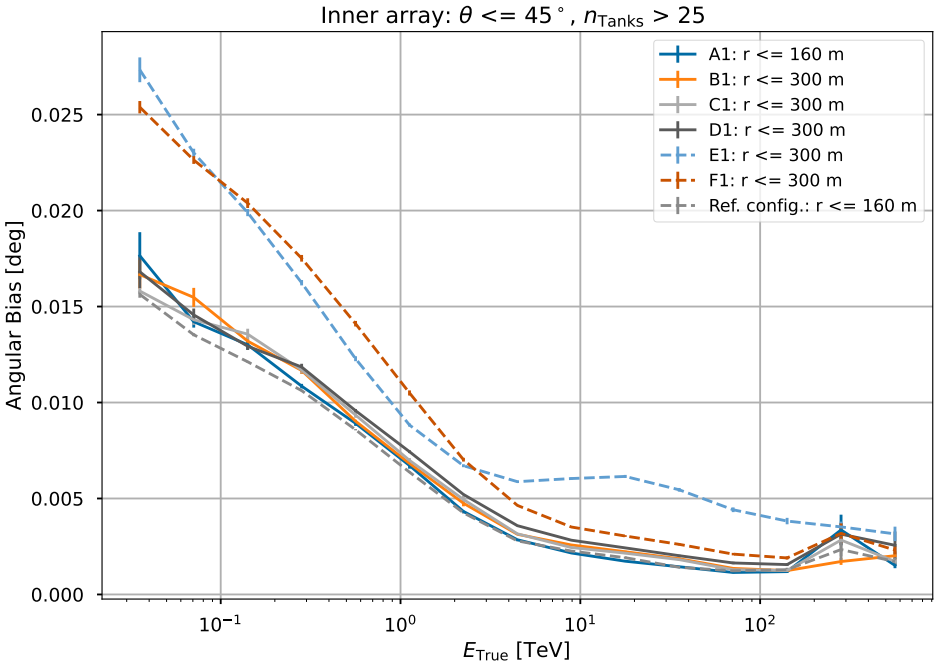

(a)

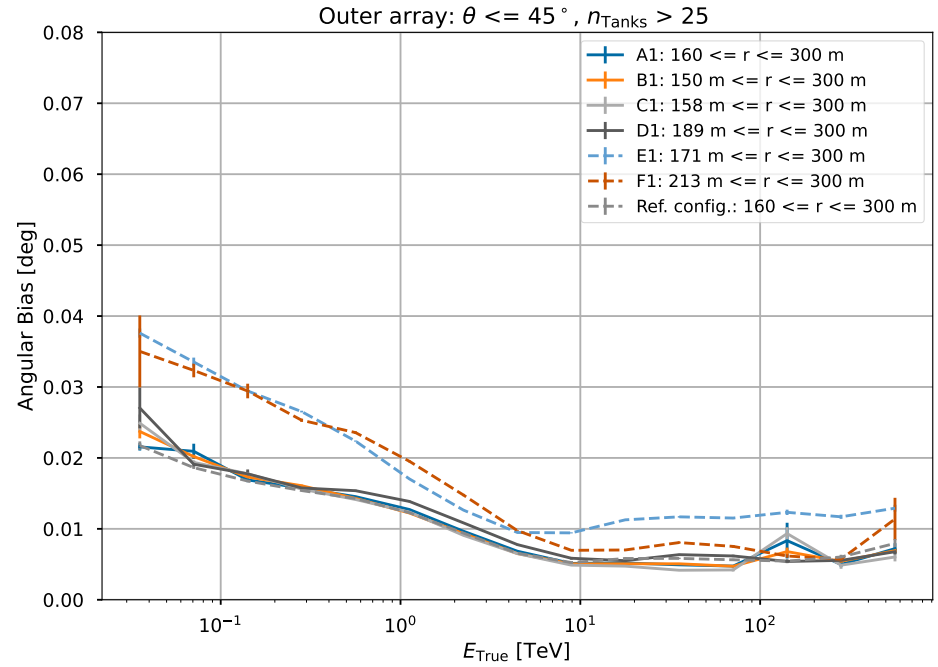

(b)

Figure 6.23: Angular bias, defined as the mean of the distribution of angles between reconstructed and true EAS direction, plotted for the 1 configurations. Showers that fell on the inner array (a) and outer array (b) are shown separately.

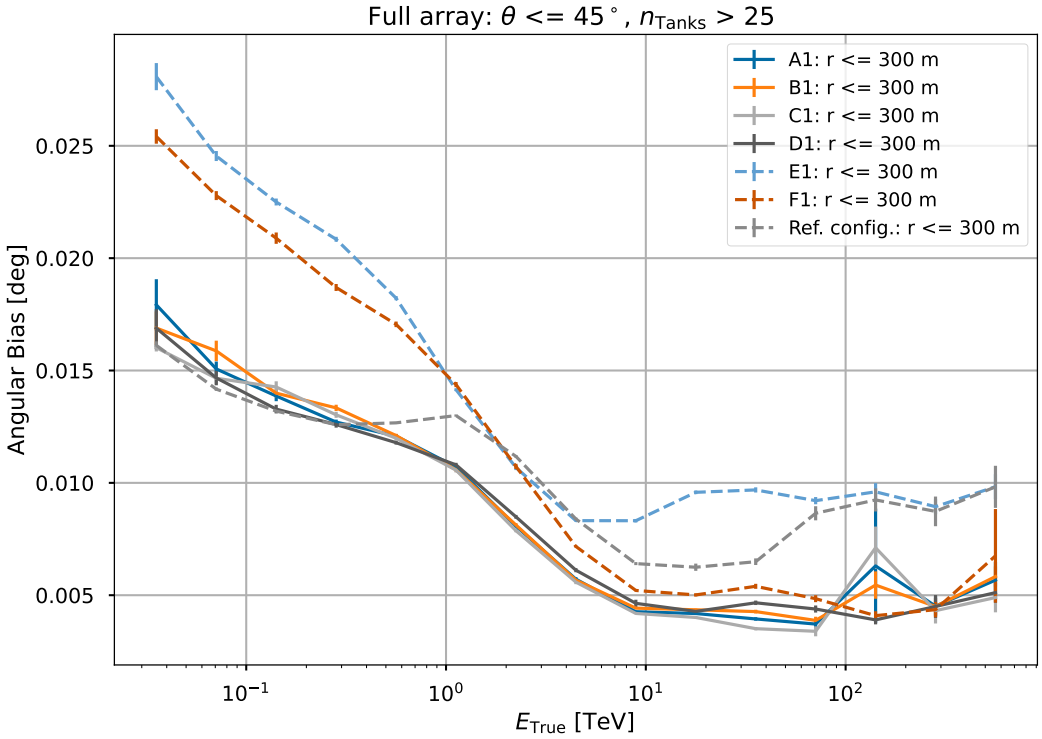

Figure 6.24: Angular bias, defined as the mean of the distribution of angles between reconstructed and true EAS direction, plotted for the 1 configurations. All showers that fell onto the array have been taken into consideration.

7 Conclusions

In this thesis, the SWGO M5 configurations were introduced and differences in array layout and tank design in between these setups were investigated. It was then possible to reconstruct a large set of simulated Monte Carlo shower data in each of those configurations. Throughout these reconstructions, only reconstructed shower properties were used, which in turn can be seen as an important step towards a more realistic reconstruction procedure that would be applicable in a real-life scenario where true shower properties are unknown.

Subsequently, the core, energy and angular reconstruction performance of each configuration has been evaluated by assessing the core, energy and angular resolution, as well as and the energy and angular bias for each setup throughout chapter 6. At this moment in time, no final conclusions with regards to the superiority of certain setups can be made, as the cut conditions have not yet been optimised for each individual configuration. However, the performance evaluation suggests that the A2, A5 and C1 configurations seem to perform best, at this stage. The reconstruction performance of A2 can be motivated by its increased array size in comparison to A1, which allows for a more precise reconstruction of high-energy events, as these events cover a larger overall area. It is however important to mention that increasing the array size up to 1200 m, as seen for A7, seems to lead to inferior performance, due to a decrease in outer array fill factor.

The good performance of A5 throughout this analysis suggests that larger inner array diameters could be benefitial inspite of a decreased inner array fill factor of only 40 %. This indicates that the benefits of increased inner array fill factors might minimise after a certain percentage, when combined with a larger inner array. In order to assess whether this is truly universally the case, this feature would need to be investigated more thouroughly by applying it to different tank designs.

The good core, energy and angular performance of the C1 setup could be an indication that increased numbers of tank units with smaller PMTs could be more benefitial in terms of the array's reconstructive capabilities than a smaller amount of tanks with larger photomultipliers, in the TeV range of the energy spectrum. Similarly to the previously mentioned features, it would again be necessary to assess this phenomenon further, in order to draw finalised conclusions on the matter. Furthermore, it would be important to optimise each data cut in accordance with each setup, in order to compare these setups in between each other even more accurately.

The next step could be to combine different tank designs and array layouts, in order to to assess their respective performance. For instance, a configuration with the C tank design, but a similar array layout to A2 or A5 could be investigated, in order to assess whether combining the features of these setups would lead to even better performance for energies above 10 TeV. By simulating shower data for even more configurations, one could further assess whether the features outlined for A2, A5 and C1 persist for different tank designs and array layouts, in order to then find the most suitable configuration for the future SWGO detection site. This master's thesis can be seen as a first performance evaluation of the presented 12 M5 configurations that could indicate which setups and features might perform best, suggesting which aspects could be investigated further, in order to later determine the best configuration for γ-ray searches in the TeV energy range.

Appendix

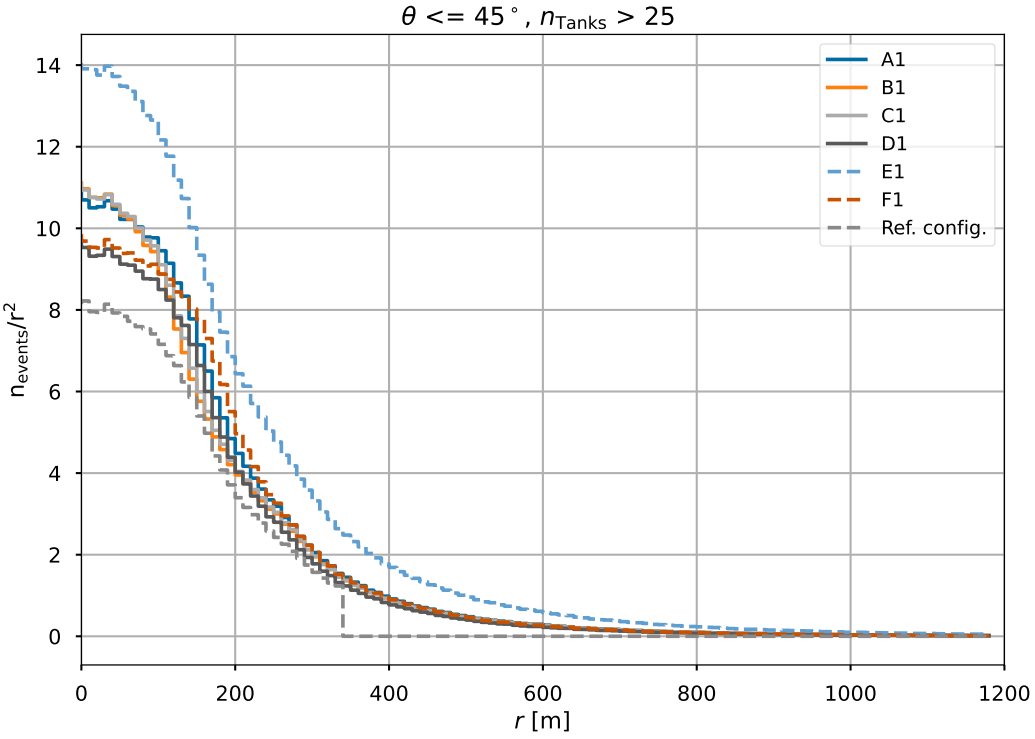

Figure .1: Radial shower core, divided by the squared radius r^2 of all events that trigger the zenith angle condition $\theta >= 45°$ and $n_{\text{Tanks}} > 25$ for each 1 configuration and the reference setup

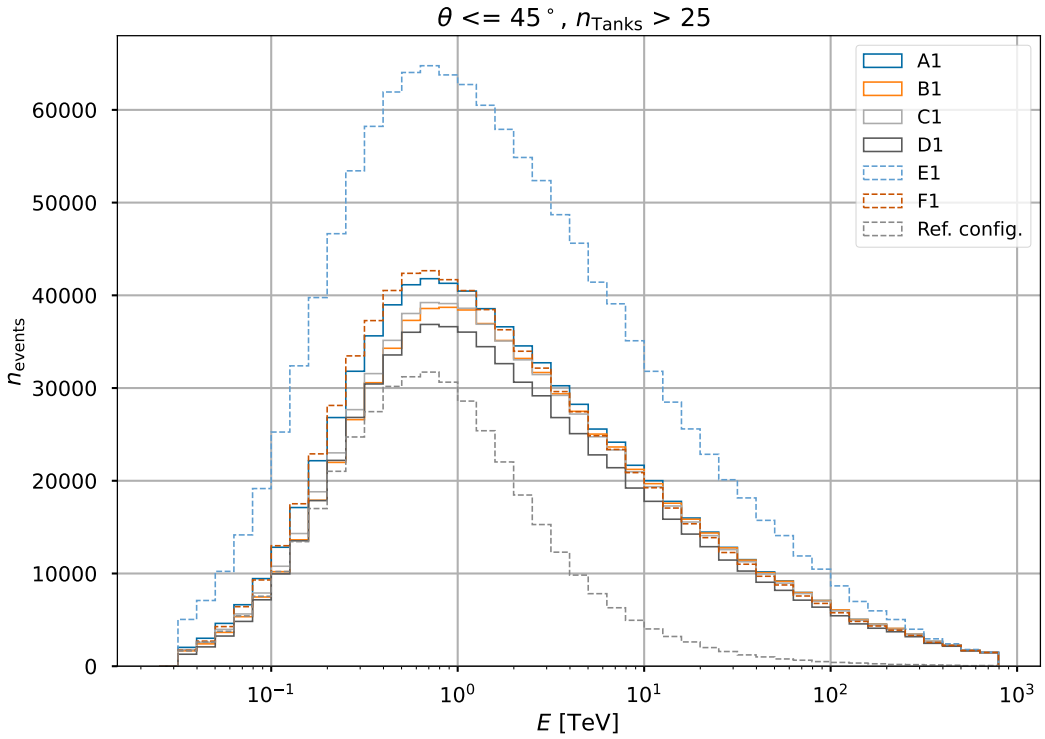

Figure .2: Energy distribution of all events that trigger the zenith angle condition $\theta >= 45°$ and $n_{\text{Tanks}} > 25$ for each 1 configuration and the reference setup

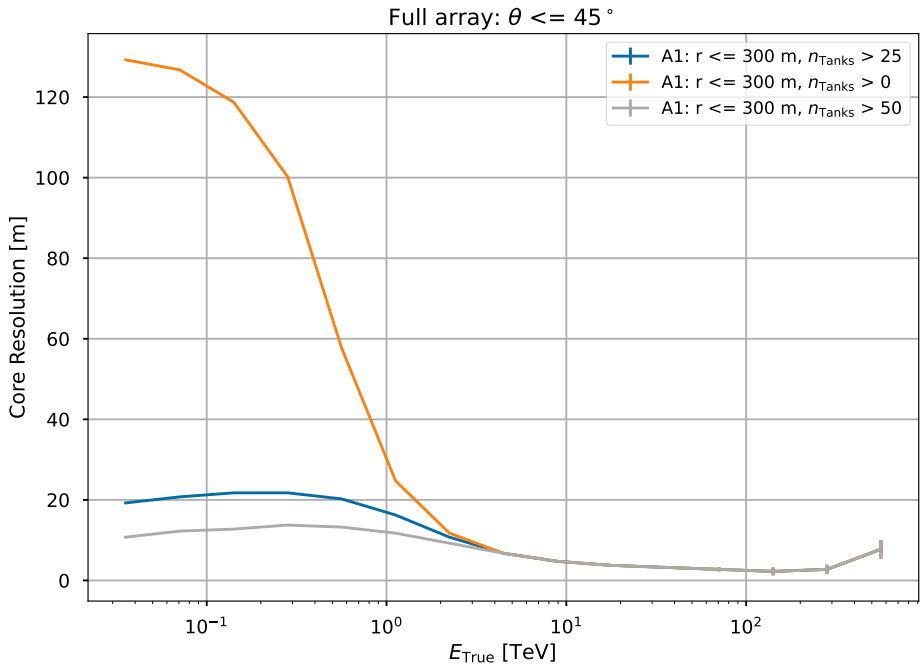

(a) Core resolution

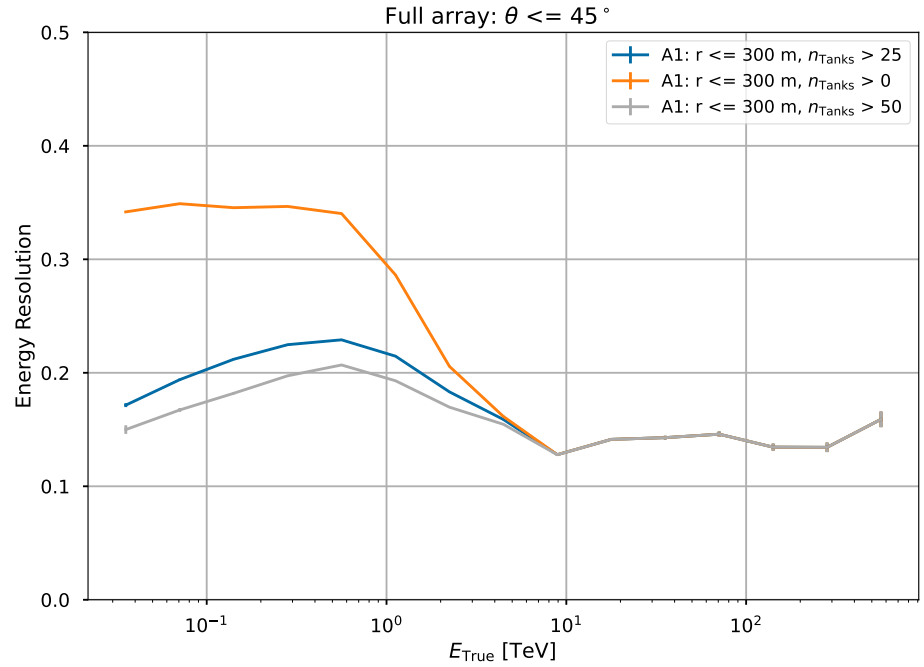

(b) Energy resolution

Figure .3: Core and energy resolution for A1 with different tank number conditions. The minimum number of tanks that needed to be hit, in order for the shower to be included in the resolution plot was set to 0, 25 and 50

References

[1] A.U. Abeysekara et al. "Searching for dark matter sub-structure with HAWC". In: *Journal of Cosmology and Astroparticle Physics* 2019.07 (July 2019), pp. 022–022. DOI: 10.1088/1475-7516/2019/07/022. URL: https://doi.org/10.1088%2F1475-7516%2F2019%2F07%2F022.

[2] P. Abreu et al. *The Southern Wide-Field Gamma-Ray Observatory (SWGO): A Next-Generation Ground-Based Survey Instrument for VHE Gamma-Ray Astronomy*. 2019. DOI: 10.48550/ARXIV.1907.07737. URL: https://arxiv.org/abs/1907.07737.

[3] S. Agostinelli et al. "Geant4—a simulation toolkit". In: *Nuclear Instruments and Methods in Physics Research Section A: Accelerators, Spectrometers, Detectors and Associated Equipment* 506.3 (2003), pp. 250–303. ISSN: 0168-9002. DOI: https://doi.org/10.1016/S0168-9002(03)01368-8. URL: https://www.sciencedirect.com/science/article/pii/S0168900203013688.

[4] A. Albert et al. "HAWC Study of the Ultra-high-energy Spectrum of MGRO J190806". In: *The Astrophysical Journal* 928.2 (Mar. 2022), p. 116. DOI: 10.3847/1538-4357/ac56e5. URL: https://doi.org/10.3847%2F1538-4357%2Fac56e5.

[5] Carl D. Anderson. "The Positive Electron". In: *Phys. Rev.* 43 (6 1933), pp. 491–494. DOI: 10.1103/PhysRev.43.491. URL: https://link.aps.org/doi/10.1103/PhysRev.43.491.

[6] Zhen Cao et al. "Ultrahigh-energy photons up to 1.4 petaelectronvolts from 12 γ-ray Galactic sources". In: *Nature* 594.7861 (2021), pp. 33–36. ISSN: 1476-4687. DOI: 10.1038/s41586-021-03498-z. URL: https://doi.org/10.1038/s41586-021-03498-z.

[7] J. Chirinos. "Introduction to Cosmic Rays". In: *AIP Conference Proceedings* 1123 (2009). DOI: 10.1063/1.3141375. URL: https://aip.scitation.org/doi/abs/10.1063/1.3141375.

[8] Ruben Conceição et al. "Detector unit and array configurations for M5". unpublished. 2022.

[9] Nicholas Copernicus et al. *Nicholas Copernicus Complete Works*. Polish scientific publ., 1978. ISBN: 978-1-349-01778-2.

[10] Tanya Edwards. "Separation of -Ray, Electron and Proton induced Air Showers applied to Diffuse Emission Studies with H.E.S.S." PhD thesis. 2017. DOI: 10.11588/heidok.00022552.

[11] D. Heck. *Extensive Air Shower Simulations with CORSIKA and the Influence of High-Energy Hadronic Interaction Models*. 2001. DOI: 10.48550/ARXIV.ASTRO-PH/0103073. URL: https://arxiv.org/abs/astro-ph/0103073.

[12] Thomas Hengstebeck. "Measurement of the energy spectrum of the BL Lac object PG1553+113 with the MAGIC telescope in 2005 and 2006". PhD thesis. Humboldt-Universität zu Berlin, Mathematisch-Naturwissenschaftliche Fakultät I, 2007. DOI: http://dx.doi.org/10.18452/15628.

[13] Kazuma Ishio. *Improvement in the gamma-ray energy reconstruction of Magic and impact on the spectral analysis of the first Gamma Ray Burst detected at TeV energies*. 2020. URL: https://edoc.ub.uni-muenchen.de/27600/.

[14] F. James and M. Roos. "Minuit - a system for function minimization and analysis of the parameter errors and correlations". In: *Computer Physics Communications* 10.6 (1975), pp. 343–367. ISSN: 0010-4655. DOI: https://doi.org/10.1016/0010-4655(75)90039-9. URL: https://www.sciencedirect.com/science/article/pii/0010465575900399.

[15] Vikas Joshi. "Reconstruction and Analysis of Highest Energy -Rays and its Application to Pulsar Wind Nebulae". PhD thesis. 2019. DOI: https://doi.org/10.11588/heidok.00026062.

[16] Vikas Joshi et al. "A template-based γ-ray reconstruction method for air shower arrays". In: *Journal of Cosmology and Astroparticle Physics* 2019.01 (2019), pp. 012–012. DOI: 10.1088/1475-7516/2019/01/012. URL: https://doi.org/10.1088\%2F1475-7516\%2F2019\%2F01\%2F012.

[17] Franziska Leitl. "Core and Energy Estimations for SWGO Using a Template-based Shower Reconstruction Method". MA thesis. Friedrich Alexander Universität Erlangen-Nürnberg, June 2021. URL: https://ecap.nat.fau.de/wp-content/uploads/2021/07/2021_MA_Leitl.pdf.

[18] M. Nagano and A. A. Watson. "Observations and implications of the ultrahigh-energy cosmic rays". English. In: *Reviews of Modern Physics* 72.3 (2000). Cited By :631, pp. 689–732. URL: www.scopus.com.

[19] Ernst Pernicka et al. "Why the Nebra Sky Disc Dates to the Early Bronze Age. An Overview of the Interdisciplinary Results". In: *Archaeologia Austriaca* 104 (Nov. 2020), pp. 89–122. DOI: 10.1553/archaeologia104s89.

[20] Hamamatsu Photonics. *Photomultiplier tubes - HAMAMATSU*. URL: https://www.hamamatsu.com/content/dam/hamamatsu-photonics/sites/documents/99_SALES_LIBRARY/etd/PMT_handbook_v3aE.pdf.

[21] Leszek Roszkowski, Enrico Maria Sessolo, and Sebastian Trojanowski. "WIMP dark matter candidates and searches—current status and future prospects". In: *Reports on Progress in Physics* 81.6 (May 2018), p. 066201. DOI: 10.1088/1361-6633/aab913. URL: https://doi.org/10.1088%2F1361-6633%2Faab913.

[22] Edna Loredana Ruiz Velasco. “Search and first detection of very-high-energy photons in gamma-ray bursts: an analysis with HAWC and H.E.S.S.” PhD thesis. 2021. DOI: 10.11588/heidok.00029603.

[23] Ahn Sangtae and Fessler Jeffrey. *Standard errors of mean, variance, and standard deviation estimators*. 2003. URL: https://www.eecs.umich.edu/techreports/systems/cspl/cspl-413.pdf.

[24] Andrew J. Smith. *HAWC: Design, Operation, Reconstruction and Analysis*. 2015. DOI: 10.48550/ARXIV.1508.05826. URL: https://arxiv.org/abs/1508.05826.

[25] M. Tanabashi et al. “Review of Particle Physics”. In: *Phys. Rev. D* 98 (3 2018), p. 030001. DOI: 10.1103/PhysRevD.98.030001. URL: https://link.aps.org/doi/10.1103/PhysRevD.98.030001.

Acknowledgements

Finally, I would like to express my gratitude towards those who supported me throughout the creation of this thesis and the entirety of my studies. Especially, I would like to thank

- Prof. Dr. Christopher van Eldik for giving me the opportunity to investigate this highly interesting topic and the supervision of my master's thesis, as well as all suggestions and ideas given throughout the biweekly meetings
- Prof. Dr Stefan Funk for the co-supervision of my thesis and all the advice given throughout the meetings
- Franziska Leitl for introducing me to this topic, answering my questions throughout the entire working process and checking this master's thesis before its submission
- Vikas Joshi for all the advice and help given throughout the past months, that resulted in an improved understanding of this topic
- the entire ECAP and SWGO Collaboration for always making me feel welcome and offering me help, whenever necessary
- my family for their unconditional support throughout the entirety of my studies and beyond

Statement of Authorship

I hereby declare that I have written this thesis without outside help and without using any sources other than those indicated. All thoughts or quotations which were inferred from these sources are clearly marked as such.

Erlangen, October 21st 2022

Matei Ruta